

Mobil

N 7 2 - 2 8 8 1 9

CASE FILE
COPY

FINAL REPORT

NEUTRON DIE-AWAY EXPERIMENT FOR REMOTE ANALYSIS

OF THE SURFACE OF THE MOON AND THE PLANETS -

PHASE III

MOBIL RESEARCH AND DEVELOPMENT CORPORATION
FIELD RESEARCH LABORATORY
DALLAS, TEXAS

FINAL REPORT

NEUTRON DIE-AWAY EXPERIMENT FOR REMOTE ANALYSIS OF
THE SURFACE OF THE MOON AND THE PLANETS - PHASE III

Period from 1 June 1970 to 30 November 1971

Prepared by: W. R. Mills and L. S. Allen
Mobil Research & Development Corporation
Field Research Laboratory
3600 Duncanville Road
Dallas, Texas 75211
214-331-6531

For: Robert P. Bryson
Apollo Lunar Exploration Office
Code MAL
National Aeronautics and Space Administration
Washington, D. C. 20546

TABLE OF CONTENTS

	<u>Page</u>
FOREWORD	iii
ABSTRACT	iv
LIST OF TABLES	vi
LIST OF FIGURES	vii
I. INTRODUCTION	1
II. DATA ANALYSIS AND PREDICTION OF VARIANCE	4
A. Least Squares Analysis	4
B. Prediction Analysis	12
C. Systematic Errors	13
III. EPITHERMAL DIE-AWAY	15
A. Functional Relationships Among Variables	15
B. Experimental Calibration Studies	29
C. Theoretical Calculations Related to Experiments	43
D. Status of Analysis of Epithermal Die-Away Data	58
IV. THERMAL DIE-AWAY	64
A. Background Discussion	64
B. Determination of Σ_a Values for Rock Models	65
C. New Thermal Neutron Die-Away Measurements on Large Models	73
D. Method of Data Analysis	76
E. New Capture Gamma-Ray Die-Away Measurements	82
V. ANALYSIS OF VENUSIAN ATMOSPHERE AND SURFACE BY LIGHTWEIGHT CPNE PROBE	87

	<u>Page</u>
VI. MISCELLANEOUS TOPICS	99
A. Neutron Output Monitor	99
B. Flight-Qualified ³ He Detector	103
VII. SUMMARY	105
LIST OF SYMBOLS	107
REFERENCES	109
APPENDICES	
TABLES	
FIGURES	

FOREWORD

This is the final report, covering the period from 1 June 1970 to 30 November 1971, on work carried out under Contract NASW-2026, "Neutron Die-Away Experiment for Remote Analysis of the Surface of the Moon and the Planets". Work under this contract constitutes the third phase of research begun under Contract NASW-1435, and which is aimed at the development of a Combined Pulsed Neutron Experiment (CPNE) for use on manned or unmanned missions to planetary surfaces.

The following individuals have participated in and contributed to the work reported: W. R. Mills, L. S. Allen, W. W. Givens, I. L. Burton, J. B. Hickman, C. W. McRight, and J. G. Baker.

Respectfully submitted,

W. R. Mills

W. R. Mills
Principal Investigator

L. S. Allen

L. S. Allen
Co-investigator

Approved by:

R. L. Caldwell

R. L. Caldwell
Principal Administrator

June 16, 1972

ABSTRACT

Continuing work on the two die-away measurements proposed to be made in the Combined Pulsed Neutron Experiment (CPNE) for analysis of lunar and planetary surfaces is described. The present report documents research done during Phase III.

A general exposition of data analysis by the least-squares method and the related problem of the prediction of variance is given. This exposition is based on a book, Prediction Analysis, by J. R. Wolberg. Prediction analysis is a technique that is useful for estimating expected variances of measured variables before the data are available. Both analysis of variance and prediction of variance are important in all of the measurements carried out in the CPNE, and are applied specifically in this report to the epithermal and thermal neutron die-away experiments.

A data analysis procedure for epithermal die-away data has been formulated. In order to facilitate the analysis, the number of independent material variables has been reduced to two: the hydrogen density and an effective oxygen density, the latter being determined uniquely from the non-hydrogenous elemental composition. Justification for this reduction in the number of variables is based on a set of 27 new theoretical calculations. Work is described related to experimental calibration of the epithermal die-away measurement. Certain difficulties were encountered and necessitated an extensive theoretical study of the new experimental results. These studies lead us to believe that ultimately

the best calibration procedure will involve a combination of theory and experiment. An interim data analysis technique based solely on theoretical calculations seems to be adequate and will be used for future CPNE field tests.

A method of analyzing thermal neutron and capture gamma-ray die-away data has been devised. In the process of investigating this method, it was found that two basic difficulties existed with previous thermal die-away measurements. The measurements on the large rock models were distorted by late returning neutrons, and the values of the macroscopic thermal neutron absorption cross section deduced from chemical analyses were in error. Both of these difficulties have been corrected by new measurements which are described. The new method of analysis permits a complete empirical calibration to be carried out, and this method will be used on the thermal die-away data obtained in future CPNE field tests.

A brief study has been made on the expected performance of the epithermal die-away measurement in analyzing the atmosphere of Venus for hydrogen. Although no numerical results have been obtained, it is proposed that the study could form the basis of more extensive investigations in the future.

A new method of remotely monitoring the neutron output of the generator used in the CPNE is proposed and investigated. This method is based on the detection of ^3He recoils in the $^3\text{He}/\text{Cd}$ detector used for the epithermal die-away measurement, and would require the addition of only a pulse discriminator and scaler to be implemented.

LIST OF TABLES

1. Values of Neutron-Nucleus Constants
2. Summary of Theoretical Epithermal Die-Away Calculations
3. Elemental Compositions of Rock Models
4. Summary of Analysis of Epithermal Die-Away Data
5. Weight Percent Water in Rock Models
6. Comparison of Analyses of Water Content
7. Macroscopic Absorption Cross Sections for Rock Models
8. Neutron Ages Determined by Least-Squares Fits to Thermal Die-Away Data

LIST OF FIGURES

1. Typical Data Analysis Situation (Two-Dimensional)
2. Experimental Epithermal Die-Away Data
3. Experimental Study of $^3\text{He}/\text{Cd}$ Detector Positions
4. Results of $^3\text{He}/\text{Cd}$ Position Study
5. Block Diagram of Electronics for Epithermal Die-Away Measurements
6. Epithermal Die-Away on Dry Sand Model; Detector on Surface; Van de Graaff; 500- μsec Period; 1 $\mu\text{sec}/\text{Channel}$
7. Epithermal Die-Away on Dry Sand Model; Detector on Surface; Sandia Generator; 500- μsec Period; 1 $\mu\text{sec}/\text{Channel}$
8. Epithermal Die-Away on Dry Sand Model; Detector Buried 30 cm; Van de Graaff; 500- μsec Period; 1 $\mu\text{sec}/\text{Channel}$
9. Epithermal Die-Away on Dry Sand Model; Detector Buried 30 cm; Van de Graaff; 1000- μsec Period; 2 $\mu\text{sec}/\text{Channel}$
10. Epithermal Die-Away on Dry Sand Model; Detector on Surface; Van de Graaff; 1000- μsec Period; 2 $\mu\text{sec}/\text{Channel}$
11. Epithermal Die-Away with Empty Tank; Detector in Surface Position; Van de Graaff; 2000- μsec Period; 4 $\mu\text{sec}/\text{Channel}$
12. Vertical Profiles of $^3\text{He}/\text{Cd}$ Response - Calculated From THEOEPI
13. Geometrical Configurations for One-Dimensional Calculations
14. $^3\text{He}/\text{Cd}$ Efficiency Curves
15. Comparison of Experimental Epithermal Die-Away and Theoretical Calculations; Dry Sand; Detector on Surface
16. Comparison of Theoretically Calculated Die-Away Curves with Programs INFSLAB and FINSLAB
17. Comparison of Experimental Epithermal Die-Away and Theoretical Calculations; Dry Sand; Buried Detector
18. Vertical Profiles of $^3\text{He}/\text{Cd}$ Detector Response for Dry Sand

19. Vertical Profiles of $^3\text{He}/\text{Cd}$ Detector Response for Sand + 0.2 Wt. % H
20. Neutron Velocity Profiles from INFLAB
21. Thermal Die-Away of Pure Water in Small Reservoir
22. Thermal Die-Away of Crushed Dunite Saturated With Pure Water in Small Reservoir
23. Thermal Die-Away of Crushed Burnet Red Granite Saturated With Pure Water in Small Reservoir
24. Thermal Die-Away of Crushed Basalt Saturated With Pure Water in Small Reservoir
25. Thermal Die-Away of Crushed Texas Rockville Granite Saturated With Pure Water in Small Reservoir
26. Probe Configuration for Thermal Die-Away Experiments
27. Thermal Neutron Die-Away Data on Knippa Basalt Model
28. Thermal Neutron Die-Away Data for All Four Large Rock Models
29. Thermal Neutron Die-Away Data for Dunite Model Fitted Over Channels 50-140
30. Thermal Neutron Die-Away Data for Burnet Red Granite Model Fitted Over Channels 50-120
31. Thermal Neutron Die-Away Data for Knippa Basalt Model Fitted Over Channels 50-108
32. Thermal Neutron Die-Away Data for Texas Rockville Granite Model Fitted Over Channels 50-90
33. Calibration Curve for Thermal Neutron Die-Away Data
34. Comparison of Thermal Die-Away on Dunite Model for Different Detector Positions
35. Gamma-Ray Die-Away Data for All Four Large Rock Models
36. Gamma-Ray Die-Away Data for Dunite Model Fitted Over Channels 44-90
37. Gamma-Ray Die-Away Data for Burnet Red Granite Model Fitted Over Channels 44-86
38. Gamma-Ray Die-Away Data for Basalt Model Fitted Over Channels 44-91

39. Gamma-Ray Die-Away Data for Texas Rockville Granite Fitted Over Channels 44-78
40. Calibration Curve for Capture Gamma-Ray Die-Away Data
41. Pulse Height Spectra in $^3\text{He}/\text{Cd}$ Detector

1. INTRODUCTION

During Phase I of work carried out under Contract NASW-1435, "Neutron Die-Away Experiment for Lunar and Planetary Surface Analysis", the feasibility of performing thermal and epithermal neutron die-away measurements on remote planetary surfaces was investigated.⁽¹⁾ It was demonstrated that such measurements are feasible under reasonable experimental conditions. During Phase II of Contract NASW-1435, the work was extended to include some problems of data analysis, possible conflicts with other parts of the Combined Pulsed Neutron Experiment (CPNE), and a demonstration of the feasibility of the CPNE concept using a single experimental probe and data acquisition system.⁽²⁾

On 19 and 20 November 1969, a meeting of personnel associated with the CPNE was held at Goddard Space Flight Center to discuss the status of the work and future plans. A list of "action items" evolved from that meeting, and this list formed the broad basis for proposed work to be done during the next phase. The complete list of items has been documented by Reed and Mandler.⁽³⁾ The most significant and critical points are related to the problem of choosing a final probe configuration for the experiment. The configuration must be selected as a result of a reasonable compromise among several parameters, including weight, volume, power, experiment running time, and quality of the results obtained. The configuration is also influenced by other factors, such as the radiation field from prospective RTG electrical power sources, the

ambient cosmic-ray-induced neutron and gamma-ray fields present at the surface of a planet, and any unusual requirements which the CPNE would impose on the host vehicle.

The question of probe weight became the prime consideration as a result of a presentation made by R. L. Caldwell and W. R. Mills of Mobil and J. H. Reed of IITRI to planetology personnel at NASA Headquarters on 22 October 1970. From this presentation and associated discussions, it became clear that the CPNE may occupy a unique position in considerations regarding surface missions to Venus. At present an experiment utilizing neutron techniques seems to be the only one which is feasible for elemental analysis. This is due to the very high surface pressure (100-200 atm) believed to exist on Venus. However, due to the small science payload weight which will likely be allotted to geochemical experiments, it is absolutely essential to reduce the weight of the CPNE to the minimum possible which still allows useful measurements to be carried out.

In its simplest and most relevant terms, the question of the probe configuration and weight is as follows: If the values of n physical variables, p_1, \dots, p_n , are either directly measured or deduced from the various parts of the CPNE, what are the expected variances, $\sigma_{p_1}^2, \dots, \sigma_{p_n}^2$, of the values for a given configuration, weight, and environmental conditions? For a given probe configuration and weight, neutron output, and data collection time, the standard deviation σ_{p_i} for the i 'th variable is one measure of the sensitivity (or threshold for measurement) of the

CPNE for that variable. A more realistic estimate of the true sensitivity is three or four times σ_{p_i} , but the standard deviation (or the variance) is a convenient measure of sensitivity and this convention was agreed upon at the GSFC meeting. The variances of the variables are also convenient indicators of the influence of the RTG radiation field and/or the ambient neutron and gamma-ray fields produced by cosmic rays. These effects can only result in increasing the $\sigma_{p_i}^2$, thereby increasing the uncertainty on a given measurement and increasing the measurement threshold for the variables.

From the above paragraph, it is evident that realistic and defensible predicted estimates of the variances of all measured variables in the CPNE are essential in order to objectively decide on the most desirable ultimate probe configuration for any given mission. For this reason, a large portion of our effort during Phase III has been addressed to the problem of determining the variances of the variables which are measured in the die-away portions of the CPNE. In order to accomplish this, the procedures for analyzing epithermal and thermal neutron die-away data must be specifically worked out and the relation between the data analysis and calibration procedures carefully studied. The bulk of the present report deals with this problem.

II. DATA ANALYSIS AND PREDICTION OF VARIANCE

A. Least Squares Analysis

The method which we will use to obtain or predict the variances of variables deduced from die-away measurements is that given by Wolberg.⁽⁴⁾ One assumes that the data will be analyzed by the least squares technique. The solution of the most general case of least squares analysis is given by Wolberg, including least squares estimates of variances and covariances of adjustable parameters. Predicted values of the parameter variances and covariances are obtained by using certain assumptions and the formal results of the least squares analysis. This procedure will be sketched briefly below in order to provide a self-contained basis for the application of the method to the die-away data. Further details can be found in the very readable book by Wolberg. Symbols used in the discussion below are given in the list at the end of this report.

Suppose that we obtain experimental values of a dependent variable Y_i and m independent variables X_{ji} ($i=1,n; j=1,m$) for n observations or data points. We assume that the true values of these variables are η_i and ξ_{ji} . If systematic errors are absent and if the experiment consisting of the n observations were repeated a large number of times, in the limit the mean value of Y_i approaches η_i and the mean value of X_{ji} approaches ξ_{ji} .

As a first step in least squares analysis, a functional relationship

between the variables is assumed:

$$\eta_i = f(\xi_{1i}, \dots, \xi_{mi}; \alpha_1, \dots, \alpha_p) \quad (1)$$

The function f is chosen on the basis of whatever a priori information is available, and contains the parameters α_k ($k=1,p$). The α_k 's may or may not be directly related to physical variables. The purpose of least squares analysis is to use the available data to find "best estimates" of the α_k . These are the least squares values a_k . If systematic errors are absent, and if the experiment is repeated many times, the average values of the a_k will approach the α_k . For a given set of experimental data, calculated or least-squares adjusted values of the dependent and independent variables are assumed to be related by the functional form in Eq. (1) with $\alpha_k = a_k$; $k=1,p$:

$$y_i = f(x_{1i}, \dots, x_{mi}; a_1, \dots, a_p) \quad (2)$$

In Eq. (2), y_i and x_{ji} are the adjusted values of the variables.

Figure 1, taken from Wolberg⁽⁴⁾, shows the relation between the observed, adjusted, and true values of the variables for the case of one independent variable. The residuals and errors are defined by

$$R_{y_i} = Y_i - y_i \quad (3)$$

$$R_{x_{ji}} = X_{ji} - x_{ji} \quad (4)$$

$$E_{y_i} = Y_i - \eta_i \quad (5)$$

$$E_{x_{ji}} = X_{ji} - \xi_{ji} \quad (6)$$

In general, E_{y_i} and $E_{x_{ji}}$ can only be estimated.

The weighted sum of squares of residuals is

$$S = \sum_{i=1}^n (w_{y_i} R_{y_i}^2 + \sum_{j=1}^m w_{x_{ji}} R_{x_{ji}}^2) \quad (7)$$

where w_{y_i} and $w_{x_{ji}}$ are suitably chosen weighting factors. The method of least squares consists of the determination of the values a_k which minimize S . In many problems the residuals $R_{x_{ji}}$ can be neglected. In the general case they must be retained in S . The form in Eq. (7) is correct provided that the errors E_{y_i} are uncorrelated and the errors $E_{x_{ji}}$ are uncorrelated.

Wolberg gives a solution of the minimization problem in an iterative form. He defines quantities A_k , where

$$A_k = a_{k0} - a_k \quad (k=1, \dots, p), \quad (8)$$

and a_{k0} is an initial guess for the value of a_k . Letting A be a $1 \times p$

row vector, the solution is given as

$$A = C^{-1} V, \quad (9)$$

where C^{-1} is the inverse of a $p \times p$ matrix and V is a $p \times 1$ column vector. The elements of C and V are given by

$$C_{kl} = \sum_{i=1}^n \frac{F_{a_k}^i F_{a_l}^i}{L_i} \quad (10)$$

$$V_k = \sum_{i=1}^n \frac{F_{a_k}^i F_0^i}{L_i}, \quad (11)$$

where the quantities $F_{a_k}^i$, F_0^i , and L_i are defined by

$$F_{a_k}^i \equiv - \frac{\partial f(x_{1i}, \dots, x_{mi}; a_1, \dots, a_p)}{\partial a_k} \Bigg|_{x_{1i}=X_{1i}, \dots, x_{mi}=X_{mi}} \quad (12)$$

$$F_0^i \equiv Y_i - f(X_{1i}, \dots, X_{mi}; a_{10}, \dots, a_{p0}) \quad (13)$$

$$L_i = \frac{1}{w_{y_i}} + \sum_{j=1}^m \frac{(F_{x_j}^i)^2}{w_{x_{ji}}} \quad (14)$$

$$F_{x_j}^i = - \left. \frac{\partial f(x_{1i}, \dots, x_{mi}; a_1, \dots, a_p)}{\partial x_{ji}} \right|_{x_{1i}=X_{1i}, \dots, x_{mi}=X_{mi}} \quad (15)$$

Initial guesses are made for a_{k0} , the A_k 's are calculated from Eq. (9), and new guesses $a_{k0} - A_k$ are thus obtained for the next iteration. The process is continued until a convergence criterion is met. With some non-linear problems, it may happen that a reasonable convergence criterion cannot be met. Wolberg discusses the steps one then takes to try to obtain convergence.

The second part of the least squares analysis is the estimate of the variances and covariances for the parameters. The variance of a_k is defined by

$$\sigma_{a_k}^2 \equiv \overline{(a_k - \alpha_k)^2}, \quad (16)$$

where the bar signifies the mean value of the squared quantity which is obtained when the experiment is repeated a large number of times.

The covariance between a_k and a_l is

$$\sigma_{kl} \equiv \rho_{kl} \sigma_{a_k} \sigma_{a_l} \equiv \overline{[(a_k - \alpha_k)(a_l - \alpha_l)]}, \quad (17)$$

where ρ_{kl} is the correlation coefficient between a_k and a_l . Under the assumptions that the errors are not large and that the quantities E_i are uncorrelated, where

$$E_i \equiv E_{y_i} + \sum_{j=1}^m F_{x_j}^i E_{x_{ji}} \quad (i=1, \dots, n)$$

Wolberg shows that

$$\sigma_{a_k}^2 \approx \frac{S}{n-p} c_{kk}^{-1} \quad (18)$$

and

$$\sigma_{kl} \approx \frac{S}{n-p} c_{kl}^{-1}, \quad k \neq l \quad (19)$$

where S is the weighted sum of the residuals for the converged values of the a_k 's. Equations (18) and (19) are approximate because the data of a single experiment can yield only estimates of the variances and covariances. Unbiased estimates of $\sigma_{a_k}^2$ and σ_{kl} are denoted by $s_{a_k}^2$ and s_{kl} , respectively, and are given by

$$s_{a_k}^2 = \frac{S}{n-p} c_{kk}^{-1} \quad (20)$$

$$s_{kl} = \frac{S}{n-p} c_{kl}^{-1} \quad (21)$$

In the applications with which we are concerned (i.e. die-away measurements), we are not interested in the values of $\sigma_{a_k}^2$ and σ_{k1} as such. Instead, we are interested in σ_y^2 when y is determined from a measurement on an unknown material, assuming that the a_k 's have been determined in a previous calibration. Thus, we have

$$y = f(x_1, \dots, x_m; a_1, \dots, a_p), \quad (22)$$

and the measured variables x_j have variances $\sigma_{x_j}^2$ (and possibly non-zero covariances $\sigma_{x_i x_j}$). The variance of y is determined as follows. From Eq. (22),

$$\Delta y = \sum_{i=1}^m \left(\frac{\partial f}{\partial x_i} \Delta x_i \right) + \sum_{k=1}^p \left(\frac{\partial f}{\partial a_k} \Delta a_k \right) \quad (23)$$

By the definition of variance,

$$\sigma_y^2 \equiv \overline{(\Delta y)^2} \quad (24)$$

Squaring Eq. (23) and averaging, we have

$$\sigma_y^2 = \sum_{i=1}^m \sum_{j=1}^m \left(\frac{\partial f}{\partial x_i} \right) \left(\frac{\partial f}{\partial x_j} \right) \overline{(\Delta x_i) (\Delta x_j)} + \sum_{k=1}^p \sum_{l=1}^p \left(\frac{\partial f}{\partial a_k} \right) \left(\frac{\partial f}{\partial a_l} \right) \overline{(\Delta a_k) (\Delta a_l)}$$

$$+ \sum_{i=1}^m \sum_{k=1}^p \left(\frac{\partial f}{\partial x_i} \right) \left(\frac{\partial f}{\partial a_k} \right) \overline{(\Delta x_i)(\Delta a_k)} \quad (25)$$

If we assume no correlation between the Δx_i and Δa_k , which is a reasonable assumption, then

$$\sigma_y^2 = \sum_{i=1}^m \sum_{j=1}^m \left(\frac{\partial f}{\partial x_i} \right) \left(\frac{\partial f}{\partial x_j} \right) \sigma_{x_i x_j} + \sum_{k=1}^p \sum_{l=1}^p \left(\frac{\partial f}{\partial a_k} \right) \left(\frac{\partial f}{\partial a_l} \right) \sigma_{kl} \quad (26)$$

$$= \sum_{i=1}^m \sum_{j=1}^m F_{x_i} F_{x_j} \sigma_{x_i x_j} + \sum_{k=1}^p \sum_{l=1}^p F_{a_k} F_{a_l} \sigma_{kl} \quad (27)$$

In Eq. (27), $\sigma_{x_i x_i} = \sigma_{x_i}^2$, $\sigma_{kk} = \sigma_{a_k}^2$, and the partial derivatives F_{x_i} and F_{a_k} are to be evaluated for the measured values of x_1, \dots, x_m on the unknown material. An estimate of σ_y^2 is given by

$$s_y^2 = \sum_{i=1}^m \sum_{j=1}^m F_{x_i} F_{x_j} s_{x_i x_j} + \sum_{k=1}^p \sum_{l=1}^p F_{a_k} F_{a_l} s_{kl}, \quad (28)$$

where $s_{x_i x_j}$ is an estimate of the covariance between the independent variable measurements, and s_{kl} is given by Eq. (21). Also, $s_{x_i x_i} = s_{x_i}^2$ and $s_{kk} = s_{a_k}^2$.

B. Prediction Analysis

We now wish to answer the following question: Assuming the data are subjected to least squares analysis, can we predict the values of $\sigma_{a_k}^2$, σ_{kl} , and σ_y^2 in Eqs. (18) (19), and (27), respectively? These predicted values are denoted by $\hat{\sigma}_{a_k}^2$, $\hat{\sigma}_{kl}$, and $\hat{\sigma}_y^2$. Similarly, the predicted values of any other quantities will be shown with a caret on top. Wolberg⁽⁴⁾ adopts the definition that the predicted value of any quantity is the mean value of the unbiased estimate of that quantity which would be obtained if the experiment were repeated many times. Thus,

$$\hat{\sigma}_{a_k}^2 = s_{a_k}^2 = \frac{\hat{S}}{n - p} (\hat{c}_{kk})^{-1} \quad (29)$$

$$\hat{\sigma}_{kl} = s_{kl} = \frac{\hat{S}}{n - p} (\hat{c}_{kl})^{-1} \quad (30)$$

$$\hat{\sigma}_y^2 = s_y^2 = \sum_{i=1}^m \sum_{j=1}^m \hat{F}_{x_i} \hat{F}_{x_j} \hat{s}_{x_i x_j} + \sum_{k=1}^p \sum_{l=1}^p \hat{F}_{a_k} \hat{F}_{a_l} \hat{s}_{kl} \quad (31)$$

The quantity S has the "chi-squared" distribution, and therefore has a mean value equal to the number of degrees of freedom. Thus, $\hat{S} = n-p$, and we have

$$\hat{\sigma}_{a_k}^2 = (\hat{c}_{kk})^{-1} \quad (32)$$

$$\hat{\sigma}_{kl} = (\hat{C}_{kl})^{-1} \quad (33)$$

$$\hat{\sigma}_y^2 = \sum_{i=1}^m \sum_{j=1}^m \hat{F}_{x_i} \hat{F}_{x_j} \hat{s}_{x_i x_j} + \sum_{k=1}^p \sum_{l=1}^p \hat{F}_{a_k} \hat{F}_{a_l} (\hat{C}_{kl})^{-1} \quad (34)$$

Equations (32) - (34) are the basic equations of prediction analysis.

In order to carry out prediction analysis calculations, one must solve two main problems:

- (i) Obtain a suitable functional form $f(x_1, \dots, x_m; \alpha_1, \dots, \alpha_p)$ from which partial derivatives can be evaluated, and
- (ii) calculate the predicted elements of the matrix C, from which the predicted inverse $(\hat{C})^{-1}$ is obtained.

The predicted elements of C are given from Eq. (10) by

$$\hat{C}_{kl} = \sum_{i=1}^n \frac{\hat{F}_{a_k}^i \hat{F}_{a_l}^i}{\hat{L}_i} \quad (35)$$

C. Systematic Errors

The treatment of least squares analysis, and the subsequent prediction analysis, was based on the assumption that only random errors are present. If the experiment is repeated a large number of times, the average values of all quantities would approach their true values:

$$\bar{Y}_i \rightarrow \eta_i$$

$$\bar{x}_{ji} \rightarrow \xi_{ji}$$

$$\bar{a}_k \rightarrow \alpha_k$$

If systematic errors are present, some or all of the above averages will not approach the true values. Wolberg⁽⁴⁾ classifies two types of systematic error:

Type 1: Errors which cause the measured values of a variable to not approach the true value.

Type 2: Errors which cause the average a_k to differ from the α_k , even though type 1 errors are absent.

Type 1 errors would normally be expected to arise from purely experimental sources. Type 2 errors would probably arise most often in the data analysis process. Examples of type 2 errors are, 1) using an inappropriate function in Eq. (1), and 2) failing to include one or more independent variables in the analysis.

We will not go further into the general problem of systematic errors here. In effect, one must identify all the possible sources of systematic errors, determine how they enter the analysis, and estimate the magnitude of the errors.

III. EPITHERMAL DIE-AWAY

A. Functional Relationships Among Variables

At the conclusion of the work done on epithermal die-away during Phase II, two principal problems remained. These were (1) the derivation of a convenient and workable relationship among experimental data obtained in an epithermal die-away measurement and the material neutron constants which govern the die-away, and (2) the development of a satisfactory calibration procedure. This section is devoted to the first problem.

We first need some measure of an observed epithermal die-away curve. Experimental data for the four large models at Mobil were given in Fig. 17 of Reference 2. For ready reference, these data are reproduced here in Fig. 2. As a measure of the die-away rate, we have chosen to use the approximate negative logarithmic slope at a delay time of 50 μ sec. If $R(t)$ is the actual detector response as a function of delay time t , then the negative logarithmic slope at 50 μ sec is

$$- \left[\frac{d}{dt} \ln R(t) \right]_{t=50}$$

For actual data, we will approximate $\ln R(t)$ by a straight line over the range 40 to 60 μ sec:

$$\ln R(t) \stackrel{\text{l.s.}}{=} -\gamma t + b, \quad 40 \leq t \leq 60 \mu\text{sec.}$$

The letters l.s. over the equals sign indicate that the parameters y and b will be determined by least squares fit; thus

$$y \approx - \left[\frac{d}{dt} \ln R(t) \right]_{t=50} \quad (36)$$

The choice of the negative logarithmic slope, as determined over the range 40 to 60 μsec , for the experimental parameter does not, of course, make use of all the epithermal die-away data obtained in a measurement. Use of the complete set of data points would lead to a very difficult non-linear least squares problem in order to deduce estimates of material neutron constants from the data. The development in this section leads to a linear least squares analysis and this must suffice for the present.

We now need to decide what the appropriate variables are which describe the physical and chemical properties of the material we are trying to analyze. To do this, consider the material parameters which enter the Boltzmann transport equation for epithermal neutrons. We previously used the Greuling-Goertzel scattering kernel approximation and the diffusion approximation to obtain an equation for the neutron flux $\phi(r, z, u, t)$, where r and z are cylindrical coordinates, u is neutron lethargy, and t is time. ⁽²⁾ The equation, good only for neutrons with energy greater than about 1 eV and for constant scattering cross section, is

$$\frac{1}{v_0} e^{\frac{u}{2}} \frac{\partial \phi}{\partial t} + \frac{\xi \Sigma}{\gamma} \phi - D \nabla^2 \phi = \frac{\xi \Sigma}{\gamma^2} \int_0^u e^{\frac{u' - u}{\gamma}} \phi \, du' + S(r, z, u, t) \quad (37)$$

In Eq. (37), v_0 is the speed of source neutrons, ∇^2 is the Laplacian operator in cylindrical coordinates, and S is the source term. The physical parameters Σ , D , ξ , and γ are given below for a single element:

$$\Sigma = \frac{0.602}{M} \rho \sigma \quad (38)$$

$$D = \frac{1}{3(1 - \frac{2}{3M}) \Sigma} \quad (39)$$

$$\xi = 1 - \frac{(M-1)^2}{2M} \ln \left(\frac{M+1}{M-1} \right) \quad (40)$$

$$\gamma = \frac{1}{\xi} \left\{ 1 - \frac{(M-1)^2}{2M} \ln \left(\frac{M+1}{M-1} \right) \left[1 + \ln \left(\frac{M+1}{M-1} \right) \right] \right\} \quad (41)$$

In these equations,

M = mass of scattering nucleus relative to the neutron mass,

ρ = bulk density (gm/cc),

σ = microscopic scattering cross section (barns).

For mixtures of elements,

$$\Sigma = \sum_i \frac{0.602}{M_i} \rho w_i \sigma_i \quad (42)$$

$$D = 1 / \left\{ 3 \sum_i \frac{0.602}{M_i} \left(1 - \frac{2}{3M_i} \right) \rho w_i \sigma_i \right\} \quad (43)$$

$$\xi = \frac{1}{\Sigma} \sum_i \frac{0.602}{M_i} \rho w_i \sigma_i \xi_i \quad (44)$$

$$\gamma = \frac{1}{\Sigma \xi} \sum_i \frac{0.602}{M_i} \rho w_i \sigma_i \xi_i \gamma_i \quad (45)$$

where w_i is the weight fraction of the i 'th type element, and the other subscripted quantities refer also to the i 'th element. For a given suite of elements present, all of the quantities in Eqs. (42) - (45) are known nuclear constants except ρ and the w_i 's. These latter quantities are the proper material variables.

Since we hope and expect that the epithermal die-away measurement will be sensitive primarily to hydrogen, it is convenient to separate its contribution in Eq. (42) - (45). If we define

$$r_i = \frac{0.602}{M_i} \sigma_i, \quad (46)$$

the epithermal neutron parameters may be written as follows:

$$\Sigma = \rho \left(12.64 w_H + 3 \sum_i' r_i w_i \right), \quad (47)$$

$$D^{-1} = \rho \left[12.64 w_H + 3 \sum_i' r_i w_i \left(1 - \frac{2}{3M_i} \right) \right], \quad (48)$$

$$\xi = \frac{12.64 w_H + \sum_i' r_i w_i \xi_i}{12.64 w_H + \sum_i' r_i w_i} \quad (49)$$

$$\gamma = \frac{12.64 w_H + \sum_i' r_i w_i \xi_i \gamma_i}{12.64 w_H + \sum_i' r_i w_i \xi_i} \quad (50)$$

The primes on the sums mean that H is omitted. The form of Eqs. (47) - (50) suggests that a simplification can be made by using the elemental densities:

$$\rho_i = \rho w_i \quad (51)$$

With this change, we have

$$\Sigma = 12.64 \rho_H + \sum_i' r_i \rho_i \quad (52)$$

$$D^{-1} = 12.64 \rho_H + 3 \sum_i' r_i \rho_i \left(1 - \frac{2}{3M_i} \right), \quad (53)$$

$$\xi = \frac{12.64 \rho_H + \sum_i' r_i \rho_i \xi_i}{12.64 \rho_H + \sum_i' r_i \rho_i} , \quad (54)$$

$$\gamma_i = \frac{12.64 \rho_H + \sum_i' r_i \rho_i \xi_i \gamma_i}{12.64 \rho_H + \sum_i' r_i \rho_i \xi_i} \quad (55)$$

and the simplest complete set of material variables consists of the elemental densities ρ_i .

As stated above, we expect the epithermal die-away measurement to be sensitive primarily to hydrogen. This suggests that we try further simplifying the problem by combining the effects of all the other elements present into a single equivalent density. If we call this variable $\rho_{\text{non-H}}$, then we have a problem in only two material variables, ρ_H and $\rho_{\text{non-H}}$. The question is whether this reduction can be done with sufficient accuracy and how is $\rho_{\text{non-H}}$ to be calculated from a given set of ρ_i . If the number of material variables can be reduced to two, it will clearly simplify the data analysis problem considerably.

To look at ways of obtaining $\rho_{\text{non-H}}$, it is convenient to rewrite Eq. (53). A good approximation for $M \gg 1$ is (5)

$$\xi \approx \frac{2}{M + \frac{2}{3}} .$$

Since the primed sum in Eq. (53) does not include hydrogen, and in practical cases would include only values of $M \geq 12$, we drop the $2/3$ in the denominator. Thus,

$$\frac{2}{3M} \approx \frac{1}{3} \xi .$$

For oxygen, $\frac{2}{3M} = 0.0417$ and $\frac{1}{3} \xi = 0.0400$. Thus we have a maximum error of about 0.2% in the factor $1 - \frac{2}{3M}$, and this is in the parameter D which probably does not play a major role in the epithermal die-away measurement. With the above approximation, we can write

$$D^{-1} \approx 12.64 \rho_H + 3 \sum_i' r_i \rho_i - \sum_i' r_i \rho_i \xi_i . \quad (56)$$

From a given set of values of ρ_i (excluding hydrogen) there are literally an infinite number of ways in which one could calculate a $\rho_{\text{non-H}}$. A method based on preserving the correct value of at least one material neutron parameter seems the best to try. It will probably be impossible to preserve the correct value for all neutron parameters. Note that in Eqs. (52), (54), (55), and (56), three different primed sums appear:

$$\sum_i' r_i \rho_i, \quad \sum_i' r_i \rho_i \xi_i, \quad \text{and} \quad \sum_i' r_i \rho_i \xi_i \gamma_i.$$

Our approach to obtaining a $\rho_{\text{non-H}}$ is to define effective elemental densities, relative to a reference element, which will make one of the above primed sums correct. Arbitrarily we choose oxygen as the reference element and define the following:

$$r_0 \rho_\Sigma \equiv \sum_i' r_i \rho_i \quad (57)$$

$$r_0 \xi_0 \rho_\xi \equiv \sum_i' r_i \rho_i \xi_i \quad (58)$$

$$r_0 \xi_0 \gamma_0 \rho_\gamma \equiv \sum_i' r_i \rho_i \xi_i \gamma_i \quad (59)$$

Thus,

$$\rho_\Sigma = \sum_i' \frac{r_i}{r_0} \rho_i \quad (60)$$

$$\rho_\xi = \sum_i' \frac{r_i \xi_i}{r_0 \xi_0} \rho_i \quad (61)$$

$$\rho_{\gamma} = \sum_i' \frac{r_i \xi_i \gamma_i}{r_0 \xi_0 \gamma_0} \rho_i \quad (62)$$

Use of one of the above three "effective oxygen densities" will make the value of Σ , $\xi\Sigma$, or $\xi\Sigma\gamma$ correct, but not more than one of the three will be correct. The problem now is to decide which, if any, of the three effective oxygen densities can be used in epithermal die-away data analysis. Table 1 gives values of the important neutron-nucleus constants. The values of σ_i are taken from the compilation by Hughes and Schwartz. (6)

We now have selected variables y , ρ_H , and $\rho_{\text{non-H}}$ (where $\rho_{\text{non-H}}$ is either ρ_{Σ} , ρ_{ξ} , or ρ_{γ}), and must find a suitable functional form relating them:

$$y = f(\rho_H, \rho_{\text{non-H}}; a_1, \dots, a_p) \quad (63)$$

We should try the three expressions for $\rho_{\text{non-H}}$ in Eq. (63) and select the one which gives best agreement with some "ground truth" information. We would still have to decide whether the best way of calculating $\rho_{\text{non-H}}$ is good enough for our purposes. Since complete experimental epithermal die-away calibration data are not available, we must use the results of theoretical calculations as our ground truth. Also, theoretical calculations provide a much wider range of the variables over which to test the choices for $\rho_{\text{non-H}}$ and the

functional form selected in Eq. (63). To this end we have calculated 27 new theoretical epithermal die-away curves. These calculations are based on the use of Eqs (6.3), (6.19), and (6.21) in Reference 2. Each combination possible among the following was calculated:

Elemental composition: basalt, granite, dunite

$\rho = 1.5, 2, 2.5 \text{ gm/cc}$

$w_H = 0, 0.0015, 0.003$

Elemental compositions used for the three rock types are those given in Table 14 of Reference 2. Table 2 of the present report gives a summary of the pertinent parameters. Values of y (in μsec^{-1}) were calculated from the formula $\frac{1}{20} \ln \frac{R(40)}{R(60)}$, where $R(40)$ and $R(60)$ are the relative theoretical epithermal responses at 40 and 60 μsec , respectively.

The simplest analytic form for Eq. (63) is a linear one:

$$y = a_1 + a_2 \rho_H + a_3 \rho_{\text{non-H}} \quad (64)$$

Sample plots of the results given in Table 2 indicate that such a linear relation is inadequate. We are thus led to try a general quadratic form:

$$y = a_1 + a_2 \rho_H + a_3 \rho_{\text{non-H}} + a_4 \rho_H^2 + a_5 \rho_H \rho_{\text{non-H}} + a_6 \rho_{\text{non-H}}^2 \quad (65)$$

Considering the variables y , ρ_H , and $\rho_{\text{non-H}}$ as mathematical entities, we could write, instead of Eqs. (63) and (65),

$$\rho_H = f(y, \rho_{\text{non-H}}; a_1, \dots, a_p) \quad (66)$$

and

$$\rho_H = a_1 + a_2 y + a_3 \rho_{\text{non-H}} + a_4 y^2 + a_5 y \rho_{\text{non-H}} + a_6 \rho_{\text{non-H}}^2 \quad (67)$$

The advantage of these forms is that ρ_H (and its variance) is the quantity we want to determine for an unknown, and ρ_H is explicitly given by Eq. (67). It is thus worthwhile to try both Eqs. (65) and (67) on the results given in Table 2.

The expressions in Eqs. (65) and (67) were used in a least squares fit to the theoretical data in Table 2. For $\rho_{\text{non-H}}$, the values ρ_Σ , ρ_ξ , and ρ_γ were used in turn. The sum of squares of residuals was taken as a measure of the goodness of fit, although this sum has no statistical significance here. For both the forms in Eqs. (65) and (67), the use of ρ_ξ led to the smallest sum of squares of residuals. In order to compare Eqs. (65) and (67), we solved Eq. (65) for ρ_H and calculated the sum of squares of residuals on ρ_H , with $\rho_{\text{non-H}}$ taken to be ρ_ξ . This latter sum was about twice as large as the corresponding sum using Eq. (67). We therefore conclude that the theoretical results are best represented by

$$\rho_H = a_1 + a_2 y + a_3 \rho_\xi + a_4 y^2 + a_5 y \rho_\xi + a_6 \rho_\xi^2 \quad (68)$$

The values of the constants $a_1 - a_6$ obtained from the least squares fit to Eq. (68) are given below:

$$a_1 = -0.0003089792906$$

$$a_2 = 0.06065874406$$

$$a_3 = -0.000148501292$$

$$a_4 = 0.1740994651$$

$$a_5 = -0.01913423303$$

$$a_6 = -0.0002122867568$$

With Eq. (68), the rms deviation is 4.14×10^{-5} . The maximum absolute error on ρ_H calculated from Eq. (68) is 7.78×10^{-5} . This error is sufficiently small that the use of Eq. (68) is suitable for data analysis. When experimental calibration data are obtained, the question of using the forms in Eq. (63) or (66) and how $\rho_{\text{non-H}}$ should be calculated must be looked at again.

Using the foregoing results we can now formulate the prediction

analysis problem for epithermal die-away in terms of specific quantities. With Eq. (68) defining the relation between the variables ρ_H , y , and ρ_ξ , the quantities defined in section II-A are as follows:

$$F_{a_1}^i = -1 \quad (69a)$$

$$F_{a_2}^i = -\gamma_i \quad (69b)$$

$$F_{a_3}^i = -(\rho_\xi)_i \quad (69c)$$

$$F_{a_4}^i = -\gamma_i^2 \quad (69d)$$

$$F_{a_5}^i = -\gamma_i (\rho_\xi)_i \quad (69e)$$

$$F_{a_6}^i = -(\rho_\xi)_i^2 \quad (69f)$$

$$F_y^i = -a_2 - 2a_4 \gamma_i - a_5 (\rho_\xi)_i \quad (69g)$$

$$F_{\rho_\xi}^i = -a_3 - a_5 \gamma_i - 2a_6 (\rho_\xi)_i \quad (69h)$$

We will assume statistical weighting; i.e. $w_{\rho_H} = \frac{1}{\sigma_{\rho_H}^2}$, $w_y = \frac{1}{\sigma_y^2}$, and $w_{\rho_\xi} = \frac{1}{\sigma_{\rho_\xi}^2}$. Thus,

$$L_i = \sigma^2_{(\rho_H)_i} + (F_y^i \sigma_{y_i})^2 + \left[F_{\rho_\xi}^i \sigma_{(\rho_\xi)_i} \right]^2 \quad (69i)$$

$$\hat{c}_{kl} = \sum_{i=1}^n \frac{\hat{F}_{a_k}^i \hat{F}_{a_l}^i}{\hat{L}_i} \quad (69j)$$

$$\hat{\sigma}_{\rho_H}^2 = (\hat{F}_y \hat{s}_y)^2 + (\hat{F}_{\rho_\xi} \hat{s}_{\rho_\xi})^2 + \sum_{k=1}^6 \sum_{l=1}^6 \hat{F}_{a_k} \hat{F}_{a_l} (\hat{c}_{kl})^{-1} + \epsilon^2 \quad (69k)$$

In evaluating Eq. (69k), it should be emphasized that the quantities $(\hat{c}_{kl})^{-1}$ are calculated from the calibration data, the quantities \hat{F}_y , \hat{F}_{ρ_ξ} , \hat{F}_{a_k} , \hat{s}_y , and \hat{s}_{ρ_ξ} refer to a measurement on an unknown, and we have assumed no correlation between the measurements of y and ρ_ξ on the unknown (i.e. $s_{y\rho_\xi} = 0$). Also in Eq. (69k), ϵ is an estimate of all systematic errors which may be present.

It would be desirable to make a study based on Eqs. (69a-k) and obtain predicted answers to the questions posed in the Introduction. An appropriate computer program, called PREDEPI, was written and successfully tested. For reasons which are based on the work described in the next three sections, no extensive calculations have been carried out with PREDEPI. However, one significant result emerged from some

preliminary calculations with the program. If either one or two different values of ρ_{ξ} are used in the calibration procedure, i.e. only one or two different non-hydrogenous compositions, the matrix \hat{C}_{kl} is ill-behaved and unphysical values of $\hat{\sigma}_{\rho_H}^2$ are obtained. This indicates that the least squares data analysis would break down in such a case. Therefore, at least three different non-hydrogenous experimental compositions must be used for calibration. Information of this type which is available in advance can obviously save a considerable amount of time and expense when such information is used intelligently to plan an experiment. In fact, prediction analysis was developed for just this type of experiment planning.

B. Experimental Studies

1. Tests on Location of $^3\text{He}/\text{Cd}$ Detector in CPNE Probe

One of the action items which resulted from the CPNE experimenters' meeting at Goddard Space Flight Center on 19, 20 November 1969 concerned flexibility in locating the $^3\text{He}/\text{Cd}$ detector. It was recommended that some tests be carried out to answer this question.

We have performed a series of epithermal die-away measurements on our basalt and crushed granite models. The experimental set-up is shown in Fig. 3. A Sandia neutron generator and tungsten attenuator were configured as shown. Although the location of a NaI detector is indicated in the figure, no actual detector was in place during these tests. Four $^3\text{He}/\text{Cd}$ detector positions were used as shown. Positions 1 and 2 were on the model surface, and positions 3 and 4 were coaxial

with the generator.

The data obtained on the crushed granite model are shown in Fig. 4. The effects we are looking for are easier to see for this model because it exhibits the slowest epithermal die-away rate of all our models. Data for positions 1, 2, and 3 are shown. The data for position 4 were very similar in behavior to those for position 3. The data for the three runs have been normalized at channel 60, or a delay of about 45 μ sec, and the behavior of all three runs after channel 60 is the same within statistics.

From the results shown in Fig. 4, we conclude that there is essentially no difference in the results which would be obtained in the various positions, provided that the die-away data at delay times greater than about 40 μ sec are used in the data analysis. The effect of fast and high energy epithermal neutrons for the different positions is different and is clearly shown in the behavior of the peak in the time distribution (i.e., greatest for position 1, least for position 3 or 4). The neutron outputs per burst for the normalized data shown in Fig. 4 were in the ratio 1:1:3 for positions 1, 2, and 3, respectively.

The question of the location of the $^3\text{He}/\text{Cd}$ detector was thoroughly discussed at an experimenters' meeting at Sandia Laboratories in Albuquerque on 21-24 June 1971. For reasons of economy of space it seemed desirable to place the detector somewhere within the symmetrical volume defined by the neutron generator, fast neutron attenuator, and NaI detector. After further study of possible probe configurations and

available ^3He detectors, it was recommended by C. A. McKeever of Sandia Laboratories and J. A. Waggoner, now of Schlumberger Well Services, that a detector of 3 in. active length and $1\frac{1}{2}$ in. active diameter be placed coaxially with the neutron generator tube, on the side opposite the neutron attenuator, and with its geometrical center approximately 20.7 cm from the target. This location would presumably produce an epithermal die-away response intermediate between that in positions 2 and 3 in Fig. 4. The electronics for driving and controlling the neutron tube would be located in the region immediately above the $^3\text{He}/\text{Cd}$ detector.

2. Experimental Calibration

As discussed in the Final Report on Phase II of our work,⁽²⁾ there remains the problem of satisfactory calibration of the epithermal die-away measurement as it is utilized in the CPNE. After considering several alternatives, we decided against having multiple water analyses carried out on samples of our rock models. There seemed to be little possibility that we would be able to adequately assess the errors involved.

For calibration of the epithermal die-away measurement, it was decided to make a series of laboratory models which consist of stoichiometrically known elemental compositions. Hydrogen content and the contents of all other elements would be determined from measured amounts of the constituents in the mixture. Hydrogen content can be easily varied by changing the amount of hydrogen-bearing material. In order to carry out this calibration program, several constraints must be met:

- 1) The models must be just large enough to be effectively semi-infinite in order to keep the costs of material down and to minimize the extensive amount of labor required to prepare the mixtures.
- 2) The materials themselves should be available at a reasonable cost.
- 3) The hydrogen content should span a range from essentially zero to the order of about 1%, and about ten values of ρ_H should be used.
- 4) The hydrogen content must be almost all stoichiometric; absorption and adsorption of water vapor from the air should be small.
- 5) The mixture of hydrogenous and non-hydrogenous materials must be homogeneous.
- 6) As mentioned in section III-A, at least three different values of effective oxygen densities must be used for proper least squares analysis when Eq. (68) is used.

Some experiments related to constraint 1 were carried out in which the Sandia generator and $^3\text{He}/\text{Cd}$ detector in position 2 (see Fig. 3) were used to obtain epithermal die-away data on the basalt and crushed granite models. Runs were taken with the generator and detector at various distances from the edge of each model. The distance at which the data become equivalent to those obtained in the center of the model was used as a guide in determining how large the hydrogenous model

mixtures must be. From an analysis of these data, it was concluded that the radius and depth of the hydrogenous models should be about 50 cm or more.

With constraints 2)-6) as a guide, we investigated several materials as to their suitability for hydrogenous and non-hydrogenous components in the proposed mixtures. Handbooks of material properties and catalogs of prices were scanned; a material was a candidate if it was available at a reasonable price and in a strictly stoichiometric form, if its physical nature was such as to allow easy mixing with other materials, and if it did not absorb or adsorb water to any appreciable extent. After a considerable amount of literature searching, obtaining samples of possible material for testing, and carrying out some tests relative to the constraints, the following materials were selected:

1. Pure silica ("frac" sand), 20-40 mesh.
2. Graphite, granular, 20-48 mesh.
3. Sucrose ("sanding sugar"), $C_{12}H_{22}O_{11}$, 26-40 mesh.

Sanding sugar is coarser than ordinary cane sugar which is "extra fine" (it will pass through a 40-mesh sieve). Samples of each of the above materials were placed in shallow open containers and left for several weeks in the accelerator room where the die-away experiments would be carried out. The sample weights were determined before and after exposure to the ambient air, the relative humidity of which is controlled to be about 50%. The silica and graphite gained less than $4 \times 10^{-4}\%$ by weight; the sanding sugar gained approximately 0.06% by weight. Both

of these are acceptably low and can be readily determined for each model which is made.

An experimental tank to contain the mixtures was ordered which was approximately 114 cm in diameter and 60 cm in height. The tank was mounted within a metal framework which was supported by a pair of jacks on casters. A track for the casters to run on was laid on the floor of the accelerator room so that the tank could be moved away from the accelerator target for filling and then moved back so that the target could be located 6.3 cm (~ 2.5 in.) above the surface of the filled tank and at any position along a diameter.

In order to experimentally verify that (1) the Van de Graaff generator and Sandia neutron generator produce equivalent epithermal die-away data, and (2) the small tank model would act essentially like the large tank models, insofar as epithermal die-away is concerned, the small tank was filled with some spare Burnet Red crushed granite, the same kind of rock that is in our large outdoor crushed granite model. Several epithermal die-away runs were taken on both the small and large models. The source-detector positions referred to below are the ones shown in Fig. 3. Runs were obtained with both the Van de Graaff and the Sandia neutron generator on the small model; only the Sandia generator could be used on the large model. Statistics were moderately good, being 50-100 counts per 1- μ sec channel at a delay of 50 μ sec.

The following is a summary of the results obtained in the runs

described above:

- 1) For detector position 4 on the small tank of granite, there is no evidence statistically of any difference between the Van de Graaff and Sandia generators.
- 2) After a delay of about 30 μ sec, there is no evidence statistically of any difference in detector positions 2 and 4 with the Sandia generator. During the first 30 μ sec the presence of the insulating oil in the generator is evident at position 2.
- 3) Runs taken with the Sandia generator and detector in positions 2 and 4 on the large crushed granite model show almost the same behavior as the corresponding runs on the small model, although there is a slight hint of a statistical trend for the epithermal die-away rate to be faster on the latter. This could indicate that the experimental tests for minimum model size described at the beginning of section III-B-2 were not completely adequate in that the effects of vertical neutron leakage were not completely accounted for.

Following the tests described above, the small tank was filled completely with the dry "frac" sand and a series of epithermal die-away runs was taken. A model consisting of only dry sand was chosen as the first one for experimentation because it was the easiest to prepare and because some problems which might exist with the selected

calibration procedure would materialize most prominently with a model containing no hydrogen. The experiments and results discussed below were obtained "stochastically", in the sense that the nature and objective of each run were dictated by the results of preceding runs.

A block diagram of the electronics and a schematic drawing of the experimental geometry are shown in Fig. 5. The cadmium-covered ^3He detector was placed on the surface of the material. The tritium target was located a distance above the surface which approximately corresponds to the position of the target in a Sandia generator when the latter is resting on the surface. The target-to-center-of-detector distance was arbitrarily chosen to be 15 cm. The configuration shown is easily reproducible on small and large models and with either the Van de Graaff or Sandia generator. The neutron detector electronics arrangement is straightforward and has been described previously⁽²⁾. The master timing clock for the system was a crystal-controlled Tektronix Model 180A Time Mark Generator. The clock pulses, which defined zero time for each cycle, were fed to a Rutherford Model A11 delay generator whose output was used to initiate time analysis in the TMC time analyzer. The purpose of delaying the start of time analysis is to permit measurement of the background immediately preceding each fast neutron burst. Clock pulses from the Time Mark Generator were also fed to an externally triggered variable frequency oscillator which, in this arrangement, served only as a pulse shaper to provide a pulse (the "initial pulse") to switch the $^2\text{H}^+$ beam onto the ^3H target and to trigger a second delay

generator. The delayed pulse from this generator was used to switch the beam off the target.

The results of the first run on the dry sand model are shown in Fig. 6. The Van de Graaff was pulsed at a rate of 2000 Hz with a burst width of 5 μ sec. A delay of 460 μ sec was used on the Model A11; since the period between bursts was 500 μ sec, this allowed 40 μ sec of background to be analyzed. The time channel width was 1 μ sec. The data were accumulated for 4×10^7 bursts over a 5.5 hour run. The average neutron output per burst was approximately 4520. The channels spanning the burst are plotted at the bottom as overflow; for these the counts/channel scale should be multiplied by 10^4 . An average background of 395 counts/channel, calculated over the first 44 channels, has been subtracted from the count in each channel.

The fact that the data were accumulated to such good statistics allows some features of the die-away curve, which normally are hidden in the statistical scatter, to be seen. The apparent behavior of the data in Fig. 6 is as follows. Early transients have disappeared by channel 80, which is about 30 μ sec after the end of the burst. From channels 80 to about 180 the die-away rate appears to be almost purely exponential, with a very slight hint of convexity toward the time axis. After channel 180 the rate of decay gradually decreases. This type of behavior is not expected on theoretical grounds. Calculated epithermal die-away curves given previously (c.f. Fig. 25 in Reference 2) exhibit a convex shape toward the time axis in the asymptotic late-time range.

In order to verify the expected theoretical behavior for dry sand specifically, a calculation of the response of an epithermal detector on a semi-infinite medium of dry sand was carried out. This calculation utilized the theory developed previously⁽²⁾ and is the same type as described in section III-A of the present report. This program, called THEOEPI, was run with the following dry sand parameters:

$$\xi = 0.1087$$

$$\gamma = 0.07661$$

$$\Sigma = 0.1544$$

$$D = 2.243$$

$$d = 4.601$$

Values of r and z were 15 and 3.4 cm, respectively. The solid curve shown in Fig. 6 is the theoretically calculated response and has been normalized to the data in the region immediately following the burst. The slopes of the experimental and theoretical die-away curves are not too different out to about channel 140; however from there on the disagreement becomes catastrophic. The conclusion is that the data are probably being perturbed by some effect which is time dependent and which is distorting the shape. Distortion of this type usually comes from one or both of two possible sources: (1) tailing on the fast neutron burst, or (2) room return neutrons.

On the next run made on the dry sand model, the Van de Graaff

generator was replaced with the Sandia generator. The same geometrical arrangement was used as is shown in Fig. 5, and the same electronic system was used with the exception that the EP 110A and EP 210A were replaced by a Rutherford B7B pulse generator which was externally triggered by the Time Mark Generator. The results of this run are shown in Fig 7. The same experimental conditions were used as in the run shown in Fig. 6, except that the total number of bursts was 5×10^7 and the neutron output per burst was about 285. When the data of Figs. 6 and 7 are overlaid for comparison, it is obvious that they look quite different. The data taken with the Sandia generator show a much greater rate of epithermal neutron die-away than the corresponding run with the Van de Graaff. Also the data show a consistent trend of concavity toward the time axis. These differences should be considered in conjunction with a similar pair of runs, described previously, which were taken when the small tank was filled with Burnet Red crushed granite. In the crushed granite runs, there was no discernable difference between the two neutron sources. We attribute the large differences seen in Figs. 6 and 7 to the fact that the "frac" sand has essentially zero hydrogen content. The hydrogen present in the insulating oil in the Sandia generator plays a key role in determining the behavior of epithermal neutrons in the dry sand model. Although the crushed granite would seem to be relatively dry, we estimate that the total content of hydrogen in the small crushed granite model is the order of 10 times greater than that in the oil filling the Sandia generator. Thus, in

the small crushed granite model the hydrogen contribution from the insulating oil is of secondary importance, whereas in the dry sand model it is the dominant factor. This clearly indicates the importance of eliminating hydrogenous materials from the generator if die-away measurements on truly dry materials are to be made properly.

In order to further elucidate the results obtained in the run shown in Fig. 6, a run was taken with the Van de Graaff target centered over the sand tank and the $^3\text{He}/\text{Cd}$ detector buried in the sand. The detector axis was vertical and displaced 2.5 cm parallel to the cylindrical axis of symmetry of the model; the center of the detector was located 30 cm below the surface of the sand. The motivation behind a run of this type was to increase the ratio of the contribution to the counting rate from the model itself to that due to room-return neutrons.

The results of the above run are shown in Fig. 8. Experimental conditions for this run were the same as for the data in Fig. 6, with the exception that a total of 3.6×10^7 neutron bursts were used at an average output per burst of approximately 3200. By comparison with Fig. 6, it is seen that the die-away rate is considerably faster with the detector buried than on the surface, there is a definite trend to convexity toward the time axis in the asymptotic region, and there is still evidence of a time-dependent background present.

It was thought to be very doubtful that a large difference, such as that observed in Figs. 6 and 8, would exist in epithermal die-away rates between the surface and buried detector positions in a truly dry

medium. In an attempt to support this opinion, we made a theoretical calculation with program THEOEPI which was similar to the calculation described in connection with Fig. 6. The material parameters were the same as given before. Values of r and z were 2.5 and 35 cm, respectively. A value of $z=35$ cm corresponds to a physical depth of 30 cm because the former must include the extrapolation distance, d . The solid curve in Fig. 8 shows the theoretical result. Two points are significant. The disagreement between theory and experiment is much greater in Fig. 8 than in Fig. 6, and the two theoretical curves in Figs. 6 and 8 practically overlay. Thus, if the theoretical calculations are trustworthy, at least in a relative sense, the experimental die-away rates should be little different for a detector located on the surface of the dry sand model and buried 30 cm into it. On the basis of the data and theoretical calculations in Figs. 6 and 8, we concluded that, (1) the surface detector run was badly distorted due to some effect or effects, (2) the buried detector run more nearly represents the true epithermal die-away in the dry sand model, although it too is being distorted somewhat, and (3) the THEOEPI program fails badly to account for the observed data.

In order to investigate the problem of apparent asymptotic distortion of the epithermal die-away data, some diagnostic runs were taken. Figure 9 shows the first of these, wherein the experimental conditions are the same as for Fig. 8 with the exceptions that the period was doubled to 1000 μ sec, channel length was doubled to 2 μ sec, and a delay of 920 μ sec

was used. In this way, more of the time cycle could be observed. The data in Fig. 9 have not been corrected for background. There is clear evidence that, due to some effect, the behavior of the die-away at long delay times is reflecting the presence of a slowly decaying component.

A run similar to that of Fig. 9 was carried out with the detector in the surface position. These data are shown in Fig. 10. The combination of lower epithermal neutron flux at the model surface and reduced shielding of the detector by the model from room neutrons results in a lower ratio of signal to time-dependent background.

As a final test for extraneous influences the sand was emptied from the tank, the detector placed in the "surface" position, and a run taken with a period of 2000 μsec , channel width of 4 μsec , and a delay of 1840 μsec . The data are shown in Fig. 11. Two background components are evident. A time-independent background, with an average intensity of 311 counts/4 μsec channel, is present and is probably due to neutron production throughout the source cycle by the $^2\text{H}^+$ beam when it is deflected off of the ^3H target. A time-dependent background is also present and probably results from neutrons produced at the target which travel to the walls of the accelerator room, make a few collisions, and return to the detector. The die-away of these neutrons in time will be strongly influenced by flight-time effects. For example, a 1-ev neutron requires about 250 μsec to travel from the nearest point on the walls to the detector location. A flight time of 250 μsec is 62.5 channels at 4 $\mu\text{sec}/$

channel. A pulse from such a neutron would occur at about channel 103 in Fig. 11, and we see that this is essentially in the middle of the time-dependent decay. Thus the assumed source of the time-dependent background seems reasonable and is not inconsistent with the data.

At this point two serious problems had presented themselves, viz., distortion of the data by a time-dependent background, which was presumed to be due to room return neutrons, and an apparent large discrepancy between experimental results and theoretical predictions. Since the proposed calibration scheme is based ultimately on theoretical arguments, it seemed necessary to solve the second problem before actively tackling the first. Also, the calibration experiments would be an irreversible process — once the materials were mixed and used, they could not be unmixed in order to repeat the experiments if something were found to be wrong with the basic approach. The next phase of this work involved an extensive theoretical study whose objective was to solve the second problem mentioned above.

C. Theoretical Calculations Related to Experiments

There are several possible sources of discrepancy between the THEOEPI-calculated die-away curves and the experimental data. It is possible that the basic theoretical model is not adequate. It is also possible that the finiteness of the dry sand model is playing a major role in determining the time behavior of the neutrons. This possibility is supported to some slight degree by the comparison runs on the large crushed granite model and on the small tank filled with crushed granite, as mentioned in

section III-B-2.

As a first attempt to study the problem theoretically, some further calculations with program THEOEPI were carried out. Two different semi-infinite media were considered; these were dry sand and sand +0.2% hydrogen by weight. The material neutron parameters for dry sand were given previously. Those for sand +0.2 wt.% H are as follows:

$$\xi = 0.2916$$

$$\gamma = 0.7258$$

$$\Sigma = 0.1940$$

$$D = 2.060$$

$$d = 3.662$$

The $^3\text{He}/\text{Cd}$ detector response was calculated as a function of time for $r = 2.5$ cm and $z = 3.4, 5, 10, 20, 30, 40, 60, 80,$ and 100 cm. The series of values of z was used in order to be able to plot vertical spatial profiles to see if the tank size might be influencing the measurements. Vertical profiles for a delay time of $50 \mu\text{sec}$ are shown in Fig. 12. The depth in a semi-infinite medium corresponding to the effective depth (including extrapolation distance) of the experimental tank is shown at $z = 64.7$ cm. It should be noted that the detector location used for the data given in Figs. 8 and 9 was 30 cm below the physical surface, or at a z -value of 34.7 cm in Fig. 12.

From the results shown in Fig. 12 it seems quite possible that the effects of finite model size could be quite large in the case of dry sand. The maximum of the vertical distribution in the semi-infinite case occurs at a z-value corresponding roughly to the bottom of the small tank. A boundary condition on the finite model is that the flux shall be zero at the extrapolated bottom of the tank. Thus, the shape of the vertical profile will be quite different for a semi-infinite medium consisting of dry sand and the small experimental tank filled with dry sand. This does not necessarily mean that there will be large differences in the epithermal die-away curves for these two cases, but such differences are strongly implied by the foregoing argument. Although no experimental results have been obtained for a small model consisting of sand +0.2 wt.% H, the vertical profile for this case shown in Fig. 12 would lead one to suspect that measurements made at depths shallower than about 30 cm might differ very little from those made on a semi-infinite medium of the same composition.

Based on the results of the THEOEPI calculations shown in Fig. 12 and the preceding discussion, it seemed necessary to theoretically investigate more thoroughly the effects of model finiteness. It was deemed too difficult to try to develop a complete three-dimensional calculation at this time. As a reasonable compromise, which would nevertheless be informative, it was decided to develop two one-dimensional theories for the geometrical situations shown in Fig. 13. In one case a semi-infinite slab was taken to be in the region $d \leq z < \infty$, and the

extrapolated plane where the flux is zero is at $z=0$. A plane source of fast neutrons is assumed to be at $z=d$. In the second case a finite slab occupies the region $d \leq z \leq a - d$. The extrapolated boundaries are at $z=0$ and $z=a$. A plane source of fast neutrons is assumed to be at $z=d$ in this case also. In applying the results of the theoretical calculations, care must be taken to add the extrapolation lengths to the physical dimensions and to locate detector positions properly with respect to the boundaries in Fig. 13.

Details of the solutions of these two problems are given in Appendices 1 and 2. The work involved in obtaining the solutions was greatly facilitated by the mathematical similarities between the one- and three-dimensional problems. Appendices 1 and 2 are little more than additions to Appendix 3 in Reference 2, wherein details of the three-dimensional solution were given. The neutron fluxes for the one-dimensional semi-infinite and finite slabs are given below:

Semi-infinite slab

$$\phi(z, v, t) = \frac{2}{\pi} \frac{e^{-\frac{\xi \Sigma v t}{\gamma}}}{(vDt)^{\frac{1}{2}}} \int_0^{\infty} \sin\left(\frac{z}{\sqrt{vDt}} x\right) \sin\left(\frac{d}{\sqrt{vDt}} x\right) e^{-x^2} g(x) dx \quad (70)$$

where

$$g(x) = \frac{\left[\left(\frac{\xi \Sigma v t}{\gamma} + x^2 \right) \left(\frac{v}{v_0} \right)^{\frac{\gamma}{\xi \Sigma v t} x^2} \right] \left(\frac{2/\gamma}{1 + \frac{\gamma}{\xi \Sigma v t} x^2} \right)}{\Gamma \left(\frac{2/\gamma}{1 + \frac{\gamma}{\xi \Sigma v t} x^2} \right)} \quad (71)$$

Finite slab

$$\phi(z, v, t) = \frac{2}{a} e^{-\frac{\xi \Sigma v t}{\gamma}} \sum_{n=1}^{\infty} \sin\left(\frac{n\pi d}{a}\right) \sin\left(\frac{n\pi z}{a}\right) e^{-v D t \left(\frac{n\pi}{a}\right)^2} h_n(v, t) \quad (72)$$

where

$$h_n(v, t) = \frac{\left\{ \left[\frac{\xi \Sigma v t}{\gamma} + v D t \left(\frac{n\pi}{a}\right)^2 \right] \left(\frac{v}{v_0}\right)^{\frac{D \gamma}{\xi \Sigma} \left(\frac{n\pi}{a}\right)^2} \right\} \left[\frac{2/\gamma}{1 + \frac{D \gamma}{\xi \Sigma} \left(\frac{n\pi}{a}\right)^2} \right]}{\Gamma \left[\frac{2/\gamma}{1 + \frac{D \gamma}{\xi \Sigma} \left(\frac{n\pi}{a}\right)^2} \right]} \quad (73)$$

The quantities appearing in the above expressions have the same meaning as in Reference 2; their definitions are included in the List of Symbols.

Although the flux given by Eq. (70) or (72) is of interest itself, it is not the theoretical quantity which is to be compared with the results of die-away experiments. Instead we must calculate the theoretical detector response $R(z, t)$, where

$$R(z, t) = \int \phi(z, v, t) \epsilon(v) dv \quad (74)$$

and $\epsilon(v)$ is the speed-dependent $^3\text{He}/\text{Cd}$ detector efficiency. It was

found previously⁽²⁾ that a useful and probably adequate analytic approximation to $\epsilon(v)$ is

$$\epsilon(v) = \begin{cases} \frac{1.43}{v} \left(1 - \frac{0.715}{v}\right), & v \geq 1 \text{ cm}/\mu\text{sec} \\ 0, & v < 1 \text{ cm}/\mu\text{sec} \end{cases} \quad (75)$$

Figure 14, which is reproduced from Reference 2, shows the correct and approximate curves for $\epsilon(v)$.

Two computer programs, called INFSLAB and FINSLAB, were written to evaluate the expressions given for the fluxes and to calculate the detector response by Eqs. (74) and (75). The following characteristics of the programs are pertinent:

- (1) In INFSLAB, the upper limit on x in the integral in Eq. (70) was fixed at $x=5$ and the integral was evaluated with a 1024 - point Simpson's rule.
- (2) In FINSLAB, the series was terminated when n reached a value such that

$$\left| e^{-vDt} \left(\frac{n\pi}{a}\right)^2 h_n / \sum_{m=1}^n \sin\left(\frac{m\pi d}{a}\right) \sin\left(\frac{m\pi z}{a}\right) e^{-vDt} \left(\frac{m\pi}{a}\right)^2 h_m \right| < 10^{-8}$$

- (3) In both INFSLAB and FINSLAB, the integral for $R(z,t)$

was evaluated by a trapezoidal approximation.

- (4) Values of the Gamma function were obtained by routines developed by G. C. Wallick of this laboratory. These routines are based on rational polynomial approximations and return values of $\Gamma(x)$ which are correct to 13 significant figures.

A series of calculations was made with the two new programs and a modified version of the older THEOEPI program converted to a one-dimensional problem. The objectives of the various calculations varied, since the answers to several questions were being sought. The calculations and results are described below.

The first series of calculations was with FINSLAB for dry sand and sand +0.2 wt.% H. The neutron parameters for these two materials were calculated from Eqs. (42) - (45) and the constants given in Table 1. The bulk density of the sand was taken as 1.573 gm/cc (measured) and d was assumed to be $\frac{0.7104}{\Sigma}$. The material neutron parameters are given below:

<u>Parameter</u>	<u>Dry Sand</u>	<u>Sand +0.2 wt.% H</u>
ξ	0.1087	0.2916
$\Sigma(\text{cm}^{-1})$	0.1544	0.1940
γ	0.07661	0.7258
$D(\text{cm})$	2.243	2.060
$d(\text{cm})$	4.601	3.662
$v_0(\text{cm}/\mu\text{sec})$	5200	5200

Values of $a=60$ cm and $z=5$ and 30 cm were used. The following sets of values of t and v were used:

$$t = 5, 10, 20, 40, 60, 80, 100, 120 \text{ } \mu\text{sec}$$

$$v = 1, 1.5, 2, 3, 4, 6, 8, 10, 15, 20, 30, 40, 60, 80, 100, 150, 200 \text{ cm}/\mu\text{sec}$$

For each combination possible among the variables, the calculations were carried out in two ways: (1) by using the convergence criterion given in (2) above, and (2) using 50 terms in the series for $\phi(z,v,t)$. The purpose was to verify that the proposed convergence criterion was satisfactory. It was found in every case that the two ways of calculating the flux agreed to at least 9 significant figures (the number printed out). The results also showed that the series expression for $\phi(z,v,t)$ in Eq. (72) is very rapidly convergent. In most cases only a few terms were required to meet the convergence criterion, and in the worst cases some 20 terms were needed. Rate of convergence of the series was considerably greater for dry sand than for sand +0.2 wt.% H.

One result obtained from the above calculations was that the set of v -values had to be spaced finer in order to adequately outline a neutron velocity profile. In order to accomplish this, all further calculations with INFSLAB or FINSLAB were done with the following set of values of v :

<u>Range of v</u>	<u>Increment (Δv) Between Values of v</u>
$1 \leq v \leq 2$	0.1
$2 < v \leq 5.2$	0.2
$5.2 < v \leq 6$	0.4
$6 < v \leq 10$	0.5
$10 < v \leq 20$	1
$20 < v \leq 50$	2

The range of v 's stops at 50 cm/ μ sec. This upper limit is used, not because the detector efficiency is negligible at this speed, but because the neutron fluxes are negligible for $v > 50$ cm/ μ sec, even for the smallest value of t used (5 μ sec).

The next series of calculations was carried out for dry sand with both INFSLAB and FINSLAB. In each case the detector was assumed to be on the surface at $z=d=4.6$ cm. For FINSLAB the slab thickness was 60 cm, which gave a value of $a=60+2d=69.2$ cm. Epithermal die-away curves calculated from the two programs are shown in Fig. 15 along with a repeat of the corresponding experimental run. The FINSLAB curve has been normalized to the data at the beginning of the die-away and the INFSLAB curve has been normalized to the FINSLAB curve in the asymptotic decay region. From the results in Fig. 15, it is seen that the INFSLAB calculation and the data disagree badly over the entire time range, whereas the FINSLAB calculation and the data show rather good agreement over about 80 μ sec of the decay followed by an increasing divergent trend. The agreement over

the early part of the decay is somewhat artificial, since it has already been pointed out that the experimental die-away is being held up by a time-dependent background. However, the significant point of Fig. 15 is that the true decay can only be faster than is observed and thus the degree of agreement with the FINSLAB calculation and disagreement with the INFSLAB calculation must be greater than appears in the figure. This result reinforces the conclusion that the dry sand model is not effectively semi-infinite.

Next, calculations were made with INFSLAB and FINSLAB for a model of sand +0.2 wt.% H. As in Fig. 15, the detector was assumed to be on the surface at $z=d$, the extrapolation distance, and the slab thickness was 60 cm for FINSLAB. Epithermal die-away curves for these two cases are shown in Fig. 16, together with the corresponding cases for dry sand shown in Fig. 15. The curves in Fig. 16 are normalized absolutely to each other, so that no vertical shifting was done in plotting. Several things are noteworthy. There is a persistent difference in both shape and intensity between the dry sand cases. The two cases of sand +0.2 wt.% H are very nearly the same, however, in both shape and intensity. This strongly suggests that a model of the size used in the experiments which consisted of sand +0.2 wt.% H would probably be a quite satisfactory model of the corresponding semi-infinite medium.

The next calculations that were carried out were for the purpose of comparison with the data in Fig. 8. The primary objective was to look into the possibility of a combination of experimental and theoretical calibration. If the theory, especially FINSLAB, could come reasonably

close to predicting the observed data, it would be a reasonable approach to calibrate a few theoretical parameters on the basis of some selected experiments. Calculations were carried out with both INFSLAB and FINSLAB for dry sand, a detector located at $z=35$ cm, and the standard set of values for t and v . For FINSLAB, the slab thickness was taken as 60 cm ($a = 69.2$ cm). Figure 17 shows the calculated epithermal die-away curves and a repeat of the data given in Fig. 8. The disagreement between the data and the INFSLAB results is again quite large. The disagreement between the data and the FINSLAB results is not too bad when a rough estimate is made of the correction which should be removed due to the time-dependent background. This has not been done in the figure because there is no defensibly objective way to carry it out. Even after a reasonable correction for the background, the negative logarithmic slope of the experimental data will be greater than that of the FINSLAB curve in the 40-60 μ sec delay region. This is not unexpected because the theory is only one-dimensional, whereas the experiment is three-dimensional and there is neutron leakage both radially and vertically. FINSLAB accounts for only the latter. The addition of radial leakage can only increase the epithermal neutron die-away rate, and it seems a reasonable supposition that a complete three-dimensional theoretical calculation might agree quite well with the observed die-away given in Fig. 17, provided that the time-dependent background is eliminated.

The next series of calculations which was carried out was related to the question of depth of investigation. This problem has a direct

bearing on the sizes of models which would be necessary in order to look effectively semi-infinite for epithermal die-away measurements. The problem has an indirect bearing on the depths of investigation achieved in the thermal die-away and capture gamma-ray measurements, in the sense that the thermal neutron flux is driven by the epithermal flux. It should be stated at the outset, in regard to spatial questions, that the results of INFSLAB or FINSLAB should be considered as approximate guidelines rather than accurate predictions. This is because the assumption of constant neutron scattering cross sections, and the fact that cross section values in the epithermal range are used, is an excellent one insofar as time dependence of the neutron flux is concerned, but a relatively poor one for spatial dependence.

Calculations were carried out with INFSLAB for dry sand and sand +0.2 wt.% H, $t=60 \mu\text{sec}$, the standard set of values of v , and thirteen values of z from 5 through 200 cm. Calculations were carried out with FINSLAB for dry sand and sand +0.2 wt.% H, $t=60 \mu\text{sec}$, the standard set of values of v , and the following combinations of values of a and z :

$$a = 70 \text{ cm}; z = 5, 10, 20, 30, 40, 60 \text{ cm}$$

$$a = 130 \text{ cm}; z = 5, 10, 20, 30, 40, 60, 80, 100, 120 \text{ cm}$$

$$a = 210 \text{ cm}; z = 5, 10, 20, 30, 40, 60, 80, 100, 120, 140, 160, 180, 200 \text{ cm}$$

The z - values used in INFSLAB are those above for $a = 210 \text{ cm}$. A value of $t = 60 \mu\text{sec}$ was chosen as a representative delay time. The results of the calculations are shown in Figs. 18 and 19. In each case the

detector response, which is simply a certain velocity-weighted average of the flux, is plotted as a function of detector position, z . Note that the detector response has been multiplied by 10^4 for dry sand and 10^5 for sand +0.2 wt.% H.

Several features of the results plotted in Figs. 18 and 19 are noteworthy. For dry sand and $a=70$ cm, the counting rates are very much less than those for a semi-infinite medium; in fact, the spatial distribution is almost a fundamental mode, the antithesis of semi-infiniteness. In order to have a proper model for epithermal die-away calibration with the detector on the surface ($z \approx 5$ cm), for dry sand the thickness should be greater than 70 cm but need not be greater than 130 cm, whereas for sand +0.2 wt.% H a thickness of 70 cm is adequate. If epithermal calibration is desired for a buried detector position, primarily for corroborative and diagnostic purposes, larger models would be required, the sizes depending on the particular detector location.

The results shown in Figs. 18 and 19 are of interest in the implications they contain for thermal die-away measurements by a gamma-ray detector and thermal neutron capture gamma-ray spectral measurements. Since the thermal neutron flux is derived from additional slowing down of the epithermal flux, and the detector responses in the figures were calculated at a delay of 60 μ sec (at this delay most of the response is due to neutrons with energy ~ 1 ev), the spatial distribution of thermal neutrons and thermal neutron capture gamma rays must look something like

the curves given in Figs. 18 and 19. The most surprising implication is the degree to which a dry sand model of thickness about 70 cm fails to represent a semi-infinite medium. Considering the fact that the response of a NaI detector placed on the surface will be a volume weighted average over the neutron flux, the curves would indicate as much as an order of magnitude difference in counting rate between a truly semi-infinite dry medium and one whose thickness is of the order of 70 cm.

Availability of all the INFSLAB and FINSLAB calculations which have been discussed thus far provided us with the opportunity to check the accuracy of the approximate expression obtained for the flux during the work of Phase II⁽²⁾. The one-dimensional approximate solution is easily obtained by going through the three-dimensional solution and making the appropriate changes. The result for the flux is

$$\phi(z, v, t) = \frac{1}{\Gamma\left(\frac{2}{\gamma}\right) (4\pi\beta)^{\frac{1}{2}}} \left(\frac{\xi\Sigma vt}{\gamma}\right)^{\frac{2}{\gamma}} e^{-\left(\frac{\xi\Sigma vt}{\gamma}\right)} \left[e^{-\frac{(z-d)^2}{4\beta}} - e^{-\frac{(z+d)^2}{4\beta}} \right] \quad (76)$$

where

$$\beta = vDt + \frac{2D}{5\Sigma} \left[\ln\left(\frac{5\Sigma v_0 t}{\gamma}\right) - \psi\left(\frac{2}{\gamma}\right) - 1 \right], \quad (77)$$

$\psi(x)$ is the Digamma function, and all other symbols have the same meaning as given in the List of Symbols. The above flux is formally the same as that for the three-dimensional problem evaluated at $r=0$, with the sole exception that the exponent on $4\pi\beta$ is $3/2$ in the three-dimensional case instead of the $\frac{1}{2}$ appearing in Eq. (76).

The flux given by Eq. (76) was evaluated for dry sand and sand +0.2 wt.% H, for $z=d$, for $t=5, 60$, and $120 \mu\text{sec}$ for dry sand and $5, 40$, and $80 \mu\text{sec}$ for sand +0.2 wt.% H, and for the standard set of v values. Comparison with the exact fluxes in the corresponding INFSLAB calculations showed the following: (1) for dry sand the approximate flux is correct to within about 1%; (2) for sand +0.2 wt.% H, the approximate flux is too small by 17% for $t=5 \mu\text{sec}$, 12% for $t=40 \mu\text{sec}$, and 8% for $t=80 \mu\text{sec}$. Thus the slope of the approximately calculated die-away curve should be almost exactly correct for dry sand, and have a negative logarithmic slope in the 40-80 μsec range which is too small. By the law of propagation of errors, the fractional error in γ , the slope defined by Eq. (36), is

$$\left| \frac{\Delta\gamma}{\gamma} \right| \approx \frac{1}{\ln\left(\frac{R_{40}}{R_{80}}\right)} \left| \frac{\Delta R_{80}}{R_{80}} \right|, \quad (78)$$

assuming the curves to be normalized to be equal at $t=40 \mu\text{sec}$ and there are no errors in calculating R from ϕ by Eq. (74). A calculation for sand +0.2 wt.% H based on Eq. (78) gives $|\Delta y/y| \approx 1.6\%$. Slopes calculated from the theoretical detector responses for dry sand and sand +0.2 wt.% H show discrepancies between THEOEPI and INFSLAB of 6.95 and 1.12%, respectively. The reason that the dry sand slope is off by about 7% when it should be essentially correct, whereas the slope for sand +0.2 wt.% H is only off by about 1.1% when it should be off by 1.6%, almost surely lies in the fact that the detector response R is calculated in INFSLAB by a trapezoidal approximation. This is inferior to the 1024-point Simpson's rule used in THEOEPI. The discrepancy in the calculations is greater for dry sand than sand +0.2 wt.% H because of the shape of $\phi(z, v, t)$ as a function of v . Figure 20 shows plots of ϕ versus v from INFSLAB for the values of the variables mentioned above. The fluxes change much slower with v for sand +0.2 wt.% H than for dry sand. Thus a trapezoid approximation for the area under the product of $\phi(z, v, t)$ and $\epsilon(v)$ will be more accurate for the former case.

D. Status of Analysis of Epithermal Die-Away Data

Based on the results of the experimental and theoretical studies described in the two preceding sections, the status of the calibration and analysis of the epithermal die-away measurement in the CPNE may be summarized in the following points:

1. A completely empirical calibration as originally conceived is not possible with models which are 4 feet in diameter by 2 feet deep. Corrections for finiteness would have to be made in many of the cases, and this would have to be based on theory. There still remains the problem of eliminating the time-dependent background if the models are used indoors.

2. Construction of six (the minimum needed) or more models sufficiently large to be effectively semi-infinite is prohibitive, both from the cost and time standpoint.

3. The best possibility for calibration in the future is probably a combination of experimental and theoretical approaches. The idea would be to use a few models outdoors where there would be no epithermal neutron return problem. The basic model might consist of a large tank of dry sand, roughly 400 cm in diameter by 200 cm deep. In the upper part of this tank, a smaller cylindrical volume would be maintained separate from the larger volume. The dimensions of this part might be about 140 cm diameter by 70 cm depth. When the small volume is filled with dry sand, a uniform dry sand model would be obtained which is effectively semi-infinite. Mixtures of sand and hydrogenous material could be put in the small volume, the resulting models being also effectively semi-infinite. Cost of materials and time and labor of mixing would be minimized by this cylinder-within-a-cylinder arrangement. In these experiments it would be essential to use a generator with almost no hydrogenous material in it. This could

be achieved by use of the new Sandia generator if it is available, or by repackaging an old one in a thin metal gas-tight housing and using an insulating gas, such as SF₆.

4. In order to utilize a greater portion of the epithermal die-away data for analysis, the possibility of getting a more convenient form of the theoretical solution should be considered.

The question remains of what to use for an interim calibration so that the data obtained with the new test probe can be analyzed. The only possibility seems to be to use the theoretical approach given in section III-A. This method is based on the use of Eqs. (68) and (61) with the values of a_1 through a_6 given by the results of the least squares fit of Eq. (68) to the 27 theoretical cases. One way to get some idea of the adequacy of this approach is to analyze the data, shown in Fig. 2, taken on the four large rock models to see if the results seem to be at least reasonable. As a first step in carrying out this idea, the data were fit in the least squares sense over the time range 40 to 60 μ sec to the following formula:

$$\ln R(t) = -yt + b \quad (79)$$

The values of y are the least squares estimates for the negative logarithmic slope of the die-away curve. Values of ρ_{ξ} for each model were calculated from the values of the nuclear constants given in Table 1, the elemental analyses given in Table 6 of Reference 2, and

the bulk densities of the models. Table 6 of Reference 2 is reproduced in this report as Table 3. Finally values of ρ_H were calculated from Eq. (68). These data are summarized in Table 4. The values of bulk density, ρ , are those obtained by accurate measurements as part of the thermal die-away studies to be discussed in section IV. The uncertainties on y are the standard deviation resulting from the fit of Eq. (79) to the data in each case.

In order to reduce the results to a form which would allow comparison with some independent measurement, the values of ρ_H were converted to weight percent hydrogen and then to weight percent water. These were compared with the "best" chemical determinations of water content obtained previously. These best determinations were given in Table 12 of Reference 2 and are reproduced here as Table 5. Table 6 gives a final summary of the results. One bit of editing has been done on the "best" chemical value of w_{H_2O} , viz., that for Texas Rockville granite. The best value for total water content given in Table 5 was judged to be the sum of the bound water determined by combustion at the USGS and absorbed plus adsorbed water determined by weight loss from heating at our laboratory. But the solid block of Texas Rockville must have effectively almost zero absorbed and adsorbed water in the dense state when the epithermal die-away measurement was made. Most of the absorbed and adsorbed water reported must have accumulated on the sample after the rock was crushed for analysis. Therefore, the "best" chemical value of w_{H_2O} for Texas Rockville is taken to be the

bound water only.

The agreement between the "best" chemical values of w_{H_2O} and those deduced from the die-away is quite good and may be fortuitous to some extent. There is no way for us to obtain values of uncertainties on w_{H_2O} from the "best" chemical, primarily because we have no idea of the errors involved in the bound water analysis. The errors quoted on the values of w_{H_2O} from the die-away measurement are rough estimates only and have been obtained from Eqs. (28) and (68):

$$s_{\rho_H}^2 \approx (F_Y s_Y)^2 + (F_{\rho_\xi} s_{\rho_\xi})^2 + \epsilon^2 \quad (80)$$

In writing Eq. (80), we have assumed that calibration errors are lumped into the systematic error ϵ . From Eq. (68) we have

$$F_Y = -a_2 - 2a_4 Y - a_5 \rho_\xi$$

$$F_{\rho_\xi} = -a_3 - a_5 Y - 2a_6 \rho_\xi$$

For ϵ we assume a value of 4.14×10^{-5} , the rms deviation quoted previously between correct values of ρ_H and those obtained from Eq. (68). Values of a_2 - a_6 were given in section III-A, and we arbitrarily assumed s_{ρ_ξ} to be 5% of ρ_ξ . The value of $s_{w_{H_2O}}$ was obtained from

$$s_{w_{H_2O}} = s_{\rho_H} \left(\frac{\rho_H}{w_{H_2O}} \right)$$

As a point of interest it should be remarked that the reason we had so much difficulty previously in deciding how to proceed with the calibration process may be seen by comparing the values of y and w_{H_2O} (%, "best" chemical) in Table 6. It had been assumed that y and w_{H_2O} would be functionally related in a reasonably simple way. However it can be seen by comparing these values that this is not true. It was only after the theoretical arguments leading to Eq. (65) and its equivalent, Eq. (67), that a suitable relation between y and the material variables was found which ultimately permits a determination of w_{H_2O} from the die-away data.

IV. THERMAL DIE-AWAY

A. Background Discussion

Difficulties which have been encountered in analyzing thermal die-away data have been discussed previously.^(1,2) These difficulties were of two types: (1) smoothing the data, and (2) extracting estimates of physically significant parameters from the data. A partial solution to the first type of problem was described in Reference 2 and was implemented in a computer program called GUDFIT. Basically this program fits the logarithm of the observed counting rate to a polynomial in time in each of two or three time domains into which the thermal die-away data are partitioned. This procedure yields a good smooth approximation to the data in about 80% of the cases we tried. In the remaining 20% there was observed to be some type of undesirable feature in the smooth approximation. More to the point is the fact that the second type of problem still remained. This problem can be summarized as follows: according to available chemical analyses, there are essentially two models with values of macroscopic absorption cross section about 0.0065 cm^{-1} , and two with values about 0.012 cm^{-1} ; however, the observed thermal neutron and capture gamma-ray die-away rates indicated no such grouping.

The foregoing difficulties led us to speculate that either the thermal die-away rates were much more sensitive to the thermal neutron diffusion coefficient, D , than we had previously assumed, or that the chemically deduced values of Σ_a were in error, or that both of these

might be true. We also discussed the possibility of deducing the bulk density from the thermal die-away measurement if D were a sensitive parameter.

Three items of future work were contemplated relative to the thermal die-away measurements in order to surmount these difficulties:

1. Obtain a new and independent set of both He^3 and NaI die-away data using the Sandia neutron generator and the IITRI probe configuration. These would be run longer than usual in order to improve the counting statistics.
2. Have additional chemical or elemental analyses carried out on samples of the models by one or more laboratories that could make some estimate of the accuracy of their results.
3. Attempt to empirically find a suitable functional form that would allow us to estimate values of physically significant parameters from the data.

During the work of Phase III, all three of these have been essentially accomplished.

B. Determination of Σ_a Values For Rock Models

As mentioned above, the calibration procedure for thermal die-away was complicated by the ambiguous results described in the Phase II report; namely, that four distinctly different lifetimes were observed for both neutron and gamma-ray measurements on the four rock models, whereas only two distinctly different values of macroscopic absorption cross section were computed from the compositions provided

by the wet chemical analyses. Thus if one assumes that the lifetime measurements are correct, then it follows that either unexpectedly large diffusional effects exist and contribute to the observed lifetimes, or the chemical analyses are incorrect. Several theoretical studies were carried out in an attempt to see if any reasonable theoretical model for the thermal die-away process could be found which would lead to strong diffusional effects. No such model could be found. Since no theoretical justification for the needed diffusional corrections could be demonstrated, it was supposed that either the chemical analyses erred in the amounts of major elements present in the rocks, or some strongly absorbing trace element(s) had been overlooked. A very good candidate in the latter category is the element gadolinium. It has a thermal neutron absorption cross section of 46,000 barns; hence only a few parts per million of this element are needed to cause significant changes in the value of Σ_a for the rocks. The credibility of this explanation is reinforced by the fact that the average concentration of gadolinium in igneous rocks is reported to be approximately 7 parts per million⁽⁷⁾.

In view of the uncertainty as to the precise composition of our rock materials, it was concluded that the macroscopic absorption cross sections of our rock materials should be measured by an alternate pulsed neutron technique. Details of this method are given by Meadows and Whalen⁽⁸⁾; only the principal features of the method will be discussed here. Basically, the procedure is to carry out thermal neutron die-away

measurements in a small container so that the fundamental spatial mode is dominant in the observed die-away rate. The method is absolutely calibrated by a measurement in pure water. The value of Σ_a for an unknown is then determined from a measurement in a mixture of the unknown material and water. The observed lifetime, τ , is related to the thermal neutron diffusion and absorption parameters, D and Σ_a , of the mixture by the equation

$$\frac{1}{\tau} = v(\Sigma_a + D B^2) \quad (81)$$

where v is the most probable speed of thermal neutrons (2200 m/sec at the customary reference of 20°C), and B^2 is an effective geometric buckling for the fundamental mode of the decaying thermal neutron population. The fundamental mode buckling is determined by the boundary conditions applied to the solution of the neutron diffusion equation. To what extent this parameter is "effective" will be discussed subsequently; for the present B^2 is simply regarded as a known quantity from an initial experiment using only pure water. Since the diffusion parameters of water are accurately known, it is possible to extract Σ_a of the rock from a lifetime measurement using Eq. (81), provided D of the mixture is known. D can be computed with good accuracy from the chemical analyses for the major elements of the rocks and the known value of D for pure water. Trace elements are wholly unimportant because the water dominates the magnitude of D for the mixture.

A suitable reservoir is needed to contain the rock-water mixtures. Its size is important because large diffusional corrections are required if it is too small, and harmonic modes are persistent if it is too large. We used a 20x20x30-cm parallelepiped tank made of 2.5 mm thick Lucite sheets. It was covered completely with cadmium to screen out thermal neutrons returning to the reservoir from the room. The target of the Van de Graaff accelerator was positioned at the center of one 20x20-cm face of the reservoir. Shielded access into the top of the reservoir was provided for a 6x6-mm cylindrical, enriched ^6LiI detector and a 10-in. Lucite light pipe which optically coupled the detector to a photomultiplier tube. In all of the experiments reported here the detector was located at the center of the reservoir. Numerous measurements were made, however, with the detector located at the top of the rock-water mixtures in order to check the effect of locating the detector within the mixtures. The effect was always small, and agreed well with the magnitude predicted by diffusion theory. Centralization of the detector was preferred because much higher counting rates could be obtained, and the first harmonic modes are completely suppressed. Fast neutron bursts of 100 μsec were used in every case in conjunction with a period between bursts of 3000 μsec . In all of the experiments discussed in this section, the channel length of the TMC time analyzer was set at 16 μsec .

The geometric buckling for the fundamental mode of the decaying thermal neutron population in a parallelepiped reservoir is given by

$$B^2 = \left(\frac{\pi}{a+2d}\right)^2 + \left(\frac{\pi}{b+2d}\right)^2 + \left(\frac{\pi}{c+2d}\right)^2, \quad (82)$$

where a, b and c are the true physical dimensions of the reservoir, and d is the extrapolation distance which must be added to the physical dimensions to account for the fact that no thermal neutrons can return to the reservoir through the cadmium shielding. For the parallelepiped geometry d is related to the diffusion coefficient by the simple expression, $d=2.13D$. When Eq. (82) is used to relate the diffusion parameters with measured lifetimes for cases where the fundamental mode decay is slightly contaminated with higher modes, the buckling is referred to as "effective". A measure of the contamination is provided by the extent to which the values of a, b and c must differ from their true values in order for Eq. (81) to be satisfied. In the experiments reported here this difference is very small. Note, however, that B^2 varies from mixture to mixture through its dependence on the extrapolation distance d.

Figure 21 shows the first die-away data taken for pure water. Exponential decay with a single time constant appears to begin around channel 50. To be a little conservative, channels 55 and 85 were selected as the beginning and ending channels, respectively, for all lifetime computations. These computations were made using Behrens' method for treating single-exponential decay⁽⁹⁾. The lifetime of thermal neutrons in pure water was measured twice, the values obtained being $146.31 \pm .56$

μsec , and $145.79 \pm .51 \mu\text{sec}$. The average values of vD and $v\Sigma_a$ given by Martinho and Paiva⁽¹⁰⁾ for four recent pulsed-neutron measurements in pure water (referred to 20°C) are $0.036137 \pm 0.000244 \text{ cm}^2/\mu\text{sec}$ and $0.004818 \pm 0.000025 \mu\text{sec}^{-1}$, respectively. Using these values the effective buckling can be computed from Eq. (81) to be $0.056147 \pm 0.000938 \text{ cm}^2$. Since the height and width of the reservoir are identical, and equal to $2/3$ of its length, we can let $a=b=2c/3=1$ and solve for l using Eq. (82). The result is $l=20.07 \text{ cm}$ which agrees well with the true width and height of the tank. This value of l was used in all subsequent computations of B^2 for rock-water mixtures; corrections for variations in d through the diffusion coefficients were always made.

Die-away measurements for the four different rock-water mixtures are shown in Figs. 22 through 25. Note that in every case the die-away is more rapid initially than for pure water, but decay with a single exponential time constant is established prior to channel 55. All of the crushed rocks used in these experiments, except the Texas Rockville granite, were used exactly as they were received from the supplier. No further crushing or sieving was needed. This was not true, of course, for the monolithic block of Texas Rockville granite. In our first attempt to measure its cross section, samples were chipped from the block, as randomly as possible, then crushed and sieved to obtain almost uniform chips of approximately $1/8''$ diameter. Temporarily set aside was approximately $2/3$ of the original sample which had been reduced to a very fine particulate material by the crushing operation.

When die-away measurements were made on the water-saturated chips, and the data reduced to a value of Σ_a for the solid rock, it was discovered that the value of the cross section was too small to agree with die-away measurements made on the large block. This inconsistency was rectified, however, by including the fine particulate material in the lifetime measurement. To do this, it was necessary to saturate thin, alternating layers of rock chips and fine dust with distilled water. The fine material migrated significantly into the rock chips, but no gross separations occurred as frequently happens when one attempts to mix aggregates of two different sizes. Lifetime measurements were also made on two different mixtures of the fine material and water. These measurements confirmed that the fine part of the crushed rock did indeed have a larger cross section than the coarse component, the cross sections being 0.02267 cm^{-1} and 0.01823 cm^{-1} , respectively.

One obvious explanation for this result is to suppose that a principal neutron absorber is concentrated near the grain boundaries of the primary minerals of the granite, perhaps in a mineral of small relative abundance. The crushing operation could have preferentially removed the secondary mineral leaving a "depleted" coarse component in the sieve.

The absorption cross sections measured for the four igneous rocks are given in Table 7. Included also are the absorption cross sections calculated on the basis of the wet chemical analyses. Note that in every case the measured absorption cross section exceeds the cross section

computed using the chemical analyses. It would thus appear that at least one unknown thermal neutron absorber is present in all of the rocks, with the possible exception of the North Carolina Olivine (dunite). As mentioned previously, gadolinium is a prime suspect in the category of unrecognized offenders. The results of sufficiently sensitive specific chemical analyses for this element in our rock samples are not available. Two final points with regard to Table 7 should be made. First, a small correction was applied to the measured cross sections to account for the presence of the detector and light pipe in the reservoir. The magnitude of this correction, in terms of the final cross section value, never exceeded 1%. Finally, the densities shown in Table 7 apply to the rocks as they are used in our large models. The density of the Texas Rockville granite therefore refers to solid rock, whereas the others are densities of crushed material.

Solid-rock densities were needed for all of the rocks in order to calculate the absorption cross sections from the measured lifetimes. These were measured simply by adding 100 ml of crushed rock to a 200 ml flask containing 100 ml of pure ethyl alcohol and obtaining the weight of the added rock. Insolubility was assumed, but checked for each rock-alcohol mixture by measuring the density of the alcohol after each mixture was weighed. No measurable changes were observed. The results of these measurements are summarized in the following tabulation:

<u>Rock Description</u>	<u>Density - gms/cc</u>
Balsam, N.C. Olivine	3.24
Burnet Red Granite	2.64
Knippa Basalt	3.12
Texas Rockville Granite	2.63

All of the figures cited for the densities in this tabulation are believed to be significant.

C. New Thermal Neutron Die-Away Measurements on Large Models

The configuration of the thermal neutron and gamma-ray probes used on the large rock models is shown in Fig. 26. These probes were always deployed on the surface of the models in such a way that the midpoint of the source-detector spacing coincided with the center of the model. In all of the experiments the repetition rate for the 6- μ sec burst of fast neutrons from the Sandia generator was 200 pulses per second. A 25-cm source-detector spacing was adopted for both the thermal neutron and the gamma-ray detectors.

The first of the new die-away measurements on the large models was made with the neutron probe. An example of the data is shown in Fig. 27 as closed circles. In this example data were accumulated for 2 hours on the crushed basalt model. Counting statistics are good, enough better than those obtained previously that the "tailing up" of the decay curve at large values of time is clearly evident. Such results are frequently caused by thermal neutrons returning to an experiment

after scattering by a wall or ceiling. We had not anticipated problems of this nature because the models are located out-of-doors under a shelter of very light overhead structure. Nonetheless, thermal neutrons were being returned to the experiment by the 2'x6" ceiling joists and sheet iron roof, because a 1/32" sheet of cadmium completely covering the probe and the surface of the model eliminated the problem, as shown by the data in open circles in Fig. 27. It was subsequently verified that a single 6'x6' sheet of cadmium covering the experiment provided sufficient protection from the returning thermal neutrons.

A complete set of die-away measurements using the cadmium-shielded neutron probe is shown in Fig. 28. The data are normalized so as to display the differences in die-away rates observed for large values of time. Data accumulation times ranged from 1 to 3 hours, depending on the lifetime of the model. Adequate counting statistics were desired over at least 20 channels of the die-away spectrum where the decay is almost exponential. An attempt could then be made to fit this part of the data with the solution of the age-diffusion equation for the semi-infinite medium given in Reference 1:

$$n(r, z, t) = \frac{S e^{-\left[v \Sigma_a t + \frac{r^2}{4(\theta + vDt)} \right]}}{\left[4 \pi(\theta + vDt) \right]^{3/2}} \left\{ e^{-\frac{(z-d)^2}{4(\theta + vDt)}} - e^{-\frac{(z+d)^2}{4(\theta + vDt)}} \right\} \quad (83)$$

This equation was used in conjunction with the Gaussians generalized

least-squares fitting routine⁽¹¹⁾ to fit the data of interest shown in Fig. 28. In order to select, in some consistent way, the time at which the die-away period of interest begins, the data of Fig. 28 were first fitted by the empirical equation

$$\ln \phi(t) = \theta_1 - \theta_2 t + \theta_3 / t^2 \quad (84)$$

The fitting began with channel 50 and stopped when less than 100 net counts were available. Very good fits were obtained, but the magnitude of θ_3 was uncertain typically by about 20%. It follows from Eq. (84) that

$$(\partial/\partial t) \ln \phi = -\theta_2 - 2\theta_3/t^3 \quad (85)$$

Suppose we want the contribution of the second term in Eq. (85) to be a certain fraction of the first. Then

$$2\theta_3/t^3 \theta_2 = \beta, \quad (86)$$

where β is the fraction. If channel 61 is judged to be the beginning of the asymptotic decay period for the Texas Rockville Granite, then β can be calculated for this selection; the result is $\beta=.0768$. Using this value of β , the beginning channel for asymptotic decay was calculated for the other materials with the following results.

<u>Rock Description</u>	<u>Channel Number</u>
Burnet Red Granite	77
Balsam, N.C. Olivine	74
Knippa Basalt	64

Although arbitrary, this procedure was believed to be better than an eyeball estimate for all four models.

In the fit of Eq. (83) to the data shown in Fig. 28, the known values of D and Σ_a were used, but the neutron age was treated as a variable parameter. Table 8 gives the results of this study. Not unreasonable values were obtained for the ages, but the values were somewhat uncertain due to the statistical quality (and quantity) of the data. Attempts were made to fit larger portions of the data with Eq. (83), but poor results were obtained. This finding is not surprising because the simple theory cannot be expected to cope with the complicated slowing down and thermalization processes which take place during the early portion of the die-away period.

D. Method of Data Analysis

However gratifying this limited success of age-diffusion theory might be from a theoretical point of view, the asymptotic fitting procedure is basically unsatisfactory because a large amount of statistically reliable data is not used. An empirical remedy for this difficulty is Eq. (84). By comparison with Eq. (83) it can be seen

that θ_1 should be proportional to the neutron source strength S , whereas θ_2 should be governed, at least for large t , by the magnitude of $v\Sigma_a$. All non-exponential behavior is clearly lumped into θ_3 . Hence, θ_3 can be viewed as a stripping parameter which allows more of the data to be used than would be possible with only a two-term expression.

The die-away data shown in Fig. 28 were fitted with Eq. (84) over several ranges to check the sensitivity of θ_2 to the fit range. Best results were obtained when the time analysis commenced with channel 53. The same value of θ_2 was obtained as when either channel 52 or 54 was selected. These results are shown in the following tabulation of θ_2/v as a function of the beginning channel for the data fitting:

<u>Rock</u>	<u>Ch 52</u>	<u>Ch 53</u>	<u>Ch 54</u>
Dunite	0.00989	0.00988 \pm 0.00010	0.00986
Burnet Red Granite	0.01486	0.01479 \pm 0.00023	0.01474
Basalt	0.02006	0.02003 \pm 0.00019	0.02000
Texas Rockville Granite	0.02603	0.02570 \pm 0.00066	0.02619

For beginning channels prior to channel 52 the value of θ_2/v was significantly influenced by the choice of the starting channel. The terminating channel of the die-away analysis period should be determined by statistical considerations. Data need not be rejected unless the scatter increases the uncertainty associated with the value determined for θ_2 .

Examples of the data fits using Eq. (84) are shown in Figs. 29 through

32. Equation (84) gives slightly better fits to the entire set of data than

$$\ln \phi(t) = \alpha_1 - \alpha_2 t + \alpha_3/t, \quad (87)$$

the second best of the simple forms. It was hoped that θ_3 might be useful in determining the diffusion coefficient of the rocks, but this was not the case. For the data fits starting with channel 53 the statistical uncertainties associated with θ_3 ranged from 20 to 50 percent. For a remote measurement, which could be allocated no more than one-half hour of data accumulation time, meaningful values of θ_3 simply could not be obtained.

It can be seen from Eqs. (83) and (84) that θ_2/v should approach Σ_a in magnitude as Σ_a becomes very large. This trend is clearly evident in the following comparison of Σ_a and θ_2/v :

<u>Rock</u>	<u>$\Sigma_a - \text{cm}^{-1}$</u>	<u>$\theta_2/v - \text{cm}^{-1}$</u>
Dunite	0.00659±0.00030	0.00988±0.00010
Burnet Red Granite	0.01149±0.00035	0.01479±0.00023
Basalt	0.01698±0.00030	0.02003±0.00019
Texas Rockville Granite	0.02113±0.00049	0.02570±0.00066

A reasonable expression for correlating Σ_a and θ_2/v would thus appear to be

$$\Sigma_a/x = 1 - a_1/x - a_2/x^2 - a_3/x^3 \quad (88)$$

where

$$x = \theta_2/v \quad (89)$$

A calibration curve based on Eq. (88) is shown in Fig. 33. The coefficients of Eq. (88) were determined by a least-squares fit to have the following values:

$$a_1 = 0.02555$$

$$a_2 = -0.001318$$

$$a_3 = 0.00002902$$

An alternative form of Eq. (88) is clearly

$$y = x - a_1 - a_2/x - a_3/x^2 \quad (90)$$

where, for simplicity of notation, we have let

$$y = \Sigma_a \quad (91)$$

According to Wolberg⁽⁴⁾, the variance of y is computed as follows.

From the calibration data compute

$$F_{a_1}^i = -\partial y / \partial a_1 = 1 \quad (92)$$

$$F_{a_2}^i = -\partial y / \partial a_2 = 1/x_i \quad (93)$$

$$F_{a_3}^i = -\partial y / \partial a_3 = 1/x_i^2 \quad (94)$$

Form

$$L_i = \sigma_{y_i}^2 + (F_{x_i}^i \sigma_{x_i})^2, \quad (95)$$

where

$$F_{x_i}^i = -\partial y / \partial x_i = -1 - a_1/x_i^2 - 2a_2/x_i^3. \quad (96)$$

Calculate the matrix elements

$$C_{kl} = \sum_{i=1}^4 F_{a_k}^i F_{a_l}^i / L_i \quad (97)$$

From a measured value of x on the unknown surface the variance of y is then given by

$$\sigma_y^2 = (F_x \sigma_x)^2 + \sum_{k=1}^4 \sum_{l=1}^4 F_{a_k} F_{a_l} c_{kl}^{-1}, \quad (98)$$

where σ_x^2 is the variance of the measured value of x .

The entire computational problem of fitting the calibration data using Eq. (88), and calculating Σ_a from a measured value of θ_2/v is carried out by a computer program named SIGMA. The value of θ_2/v and its fractional standard deviation are obtained from GAUSHAUS when the die-away data are fitted using Eq. (84). When the calibration data were processed by program SIGMA as unknowns, the predicted cross sections compared favorably with the measured values as they should:

<u>Rock</u>	<u>Measured Σ_a</u>	<u>Predicted Σ_a</u>
Dunite	0.00659±0.00030	0.00658±0.00035
Burnet Red Granite	0.01149±0.00035	0.01167±0.00043
Basalt	0.01698±0.00030	0.01642±0.00033
Texas Rockville Granite	0.02113±0.00049	0.02160±0.00083

The predicted fractional standard deviations of Σ_a vary from case to case but average 3.7%. While greater precision is certainly desirable, such results are believed to be adequate and consistent with the combined experiment. Note that the calibration range is $0.010 \leq \theta_2/v \leq 0.026$ in units of cm^{-1} . Since absorption can be expected to dominate the

measured lifetime for values of θ_2/v exceeding 0.026, extrapolation on the high side is probably safe enough. Diffusional effects are clearly important for $\theta_2/v < 0.01$, hence extrapolation on the low side is probably very risky.

It should be noted finally with regard to thermal neutron experiments that die-away measurements were made with the helium-3 detector buried 60 cm below the surface of the rock models. The detector was located on the axis of the cylindrical model directly below the Sandia generator which was resting on the model surface. These measurements were made to check the age-diffusion theory prediction that the lifetime should increase only slightly with depth, and to make sure that the return neutron problem had been solved by the cadmium shielding. Figure 34 illustrates a typical result of these experiments. The data are not normalized; except for small variations in the output of the neutron generator the two-hour measurements are directly comparable. Very similar asymptotic die-away rates are plainly evident; lifetime values calculated for the two cases differ by only 6 percent. In order to make this measurement on the block of Texas Rockville Granite, it was necessary to drill a 1- $\frac{1}{2}$ " diameter horizontal access hole 60 cm below the surface of the slab. Similar results to those shown in Fig. 34 were obtained.

E. New Capture Gamma-Ray Die-Away Measurements

Capture gamma-ray die-away measurements on the large rock models essentially duplicated the experiments performed with the thermal neutron

detector. No changes in timing or accelerator operation were made. The gamma-ray detector system was always biased to reject photons having energies less than 250 kev. Although it was not necessary to shield the gamma-ray detector from return neutrons, suitable shielding for the model surface would have been desirable. Unfortunately, completely satisfactory shielding was either too expensive, or judged to be sufficiently thick that its use would interfere with the experiments. As a result none was used. It would appear from the data that the effect of return neutrons is small if not negligible, quite in contrast to the situation encountered when thermal neutrons were detected. This is due to the fact that the gamma-ray detector responds to thermal neutron captures occurring at considerable depth within the model.

Figure 35 is the gamma-ray counterpart of Fig. 28. Four distinctly different die-away rates are plainly evident, in agreement with the results obtained using the helium-3 detector. Fits of the individual die-away curves using Eq. (84) are shown in Figs. 36 through 39. As before, Eq. (84) gave the best fits to the entire set of data. The data fitting always began with channel 44. Earlier beginning channels could not be used because the rapid die-away component present in channels before 43 would clearly contribute to the analysis. Values of θ_2/v obtained when the time analysis commenced with channels 43, 44, and 45 are shown in the following tabulation:

<u>Rock</u>	<u>Ch 43</u>	<u>Ch 44</u>	<u>Ch 45</u>
Dunite	0.00976	0.00975±0.00020	0.00970
Burnet Red Granite	0.01348	0.01355±0.00056	0.01318
Basalt	0.02008	0.02007±0.00021	0.01985
Texas Rockville Granite	0.02518	0.02351±0.00102	0.02280

The time-base stability of the fitting procedure beginning with channel 44 is clearly quite good. Note, however, that the statistical errors are somewhat larger here than for the neutron detector.

The gamma ray calibration curve based on Eq. (88) is shown in Fig. 40. Least-squares values for the coefficients are

$$a_1 = 0.02452$$

$$a_2 = -0.001699$$

$$a_3 = 0.00004246$$

Using the computer program referred to earlier for calculating the magnitude and variance of Σ_a given θ_2/V and its fractional standard deviation, the following results were obtained for the gamma-ray calibration data

<u>Rock</u>	<u>Measured Σ_a</u>	<u>Predicted Σ_a</u>
Dunite	0.00659 \pm 0.00030	0.00660 \pm 0.00056
Burnet Red Granite	0.01149 \pm 0.00035	0.01138 \pm 0.00085
Basalt	0.01698 \pm 0.00030	0.01752 \pm 0.00037
Texas Rockville Granite	0.02113 \pm 0.00049	0.02063 \pm 0.00108

The fractional standard deviations calculated by program SIGMA average 5.8% for the gamma-ray data. Although significantly larger than the 3.7% average obtained for the thermal neutron detector, these results do not appear to warrant giving serious consideration to the inclusion of a thermal neutron detector in the combined experiment. As with the thermal neutron calibration, extrapolation should be safe enough for θ_2/v exceeding 0.025 cm⁻¹, but not for values less than 0.01.

A remote surface with θ_2/v less than 0.01 cm⁻¹ could be a rock composed largely of quartz and containing no strongly absorbing trace elements. This case could probably be handled by adding a calibration point for clean, quartz sand. We note in this connection that the macroscopic absorption cross section of a clean quartz sand was measured recently by the technique outlined earlier. The value obtained for Σ_a , 0.00280 cm⁻¹, agreed almost exactly with the cross section computed on the basis of the chemical analysis provided by the supplier.

A more serious problem is the possibility of encountering a very low-density rock having a very small macroscopic absorption cross section. Such a material could have a measured value of θ_2/v falling within the

calibration range, but one whose die-away rate would be governed by neutron leakage rather than absorption.

V. ANALYSIS OF VENUSIAN ATMOSPHERE AND SURFACE BY LIGHTWEIGHT CPNE PROBE

A CPNE experimenters' meeting was held at IIT Research Institute in Chicago on 7 October 1970 to discuss and organize a presentation to be made to planetology personnel in OSSA. The primary purpose of the meeting and presentation was to consider and propose the use of a very small lightweight CPNE probe on a surface mission to Venus. One new idea brought out was the possibility of utilizing the CPNE to analyze the dense Venusian atmosphere during the rather slow descent of the spacecraft through the atmosphere. The presentation was made at NASA headquarters on 22 October. As a result of the presentation, and discussions during and following the presentation, it was decided that high priority be given to studying the capabilities of a CPNE probe weighing less than 10 lbs.

A special problem which must be looked into is that of analyzing the Venusian atmosphere. The basic question is which, if any, of the measurements in the CPNE could yield useful information when carried out singly or repeatedly during the descent through the atmosphere. In order to answer this question one must estimate counting rates due to the desired signals and due to sources of interfering background. As was pointed out in the Introduction, this ultimately involves predictions of the variances of the variables being determined.

Data analysis procedures for the epithermal and thermal die-away measurements made on semi-infinite igneous rock models have been discussed

in preceding sections. From these results it should be possible to make some predictions about the capabilities of these two measurements in the Venusian atmosphere. Preliminary elemental detection thresholds have been obtained for semi-infinite models for the inelastic, capture, and cyclic activation gamma-ray spectral measurements.^(12, 3, 13) No similar estimates have been made for the case of an infinite medium such as the atmosphere of Venus, the composition of which is primarily CO₂ plus small amounts of N₂ and H₂O.^(14, 15)

We were asked to investigate the capabilities of the CPNE for Venusian atmosphere analysis on an "as-time-permits" basis. If the CPNE does prove to have significant promise for atmospheric analysis, it would considerably strengthen its position as a candidate for the first soft-landing mission on Venus. Unfortunately, time and money limitations did not permit us to look very extensively into this problem. This section describes the results of those studies which we were able to carry out.

It is unlikely that any approach could result in absolute predictions of detection thresholds or parameter variances which could be relied on as to accuracy. For this reason, it was decided to attempt to obtain relative values between the infinite Venusian atmosphere and semi-infinite rock models for which we have data. If this could be done, the performance of the CPNE in the atmosphere of Venus under given experimental conditions could be related to its performance in a known situation.

We consider first the epithermal die-away measurement. Recall that

the detector response is proportional to $R(r, z, t)$, where

$$R(r, z, t) = \int \phi(r, z, v, t) \epsilon(v) dv , \quad (99)$$

$\phi(r, z, v, t)$ is the velocity- and time-dependent epithermal neutron flux at a detector located at (r, z) , and $\epsilon(v)$ is the relative detection efficiency. An approximate expression for the flux for the case of a point source on a semi-infinite medium was given previously.⁽²⁾ If we assume that time channels of length τ and a total of N bursts are used, the number of counts accumulated in time channel i will be proportional to Y_i , where

$$Y_i = \eta N \int_{\text{Time channel } i} R(r, z, t) dt$$

$$\approx \eta N \tau R(r, z, t_i) ,$$

where η is the effective geometrical efficiency of the neutron detector. Using the expressions previously given for the flux and $\epsilon(v)$, the number of counts in channel i for a semi-infinite medium becomes

$$Y_i^s = \frac{1.43 \eta_{\tau NQ}}{(4\pi)^{3/2} \Gamma(\frac{2}{\gamma})} \int_{\frac{\sum t_i}{\gamma}}^{\infty} \left(1 - 0.715 \frac{\sum t_i}{\gamma x}\right) x^{\frac{2}{\gamma} - 1} e^{-x} e^{-\frac{x^2}{4\beta}} e^{-\frac{r^2}{4\beta} \left(1 - e^{-\frac{d^2}{\beta}}\right)} dx \quad (100)$$

where

$$\beta = \frac{D\gamma}{\xi \Sigma} \left\{ x + \frac{2}{\gamma} \left[\ln\left(\frac{\sum v_0 t_i}{\gamma}\right) - \psi\left(\frac{2}{\gamma}\right) - 1 \right] \right\}$$

Define the integral in Eq. (100) to J_i^s , so that

$$Y_i^s = \frac{1.43 \eta_{\tau NQ}}{(4\pi)^{3/2} \Gamma(\frac{2}{\gamma})} J_i^s \quad (101)$$

In Eq. (100) we have assumed that the detector is on the physical surface ($z=d$).

The expression for the number of counts in channel i for an infinite medium, such as the Venusian atmosphere, is similar to Eq. (100) except that the infinite medium flux must be used. This flux may be obtained from an analysis similar to that used in Appendix 3 of Reference 2. The approximate expression for the flux is

$$\phi(r, z, v, t) = \frac{Q}{\Gamma\left(\frac{2}{\gamma}\right)} \left(\frac{\xi \Sigma v t}{\gamma}\right)^{\frac{2}{\gamma}} \frac{e^{-\frac{\xi \Sigma v t}{\gamma}}}{(4\pi\beta)^{3/2}} e^{-\frac{(r^2+z^2)}{4\beta}} \quad (102)$$

In analogy with Eq. (101) we have, for the counts accumulated in channel i for an infinite medium,

$$Y_i^I = \frac{1.43 \eta \tau N Q}{(4\pi)^{3/2} \Gamma\left(\frac{2}{\gamma}\right)} J_i^I \quad (103)$$

where

$$J_i^I = \int_{\frac{\xi \Sigma t_i}{\gamma}}^{\infty} \left(1 - 0.715 \frac{\xi \Sigma t_i}{\gamma x}\right)^{\frac{2}{\gamma} - 1} e^{-x} \beta^{-3/2} e^{-\frac{r^2}{4\beta}} dx, \quad (104)$$

and we have assumed that the source-detector distance is r , the same as for the semi-infinite medium.

Although Eqs. (101) and (103) may not be extremely accurate in an absolute sense, the ratio of counts for the two situations is probably given to reasonable accuracy by

$$\frac{Y_i^I}{Y_i^S} = \frac{\left[\frac{\eta \tau N Q}{\Gamma(\frac{2}{\gamma})} \right]_I}{\left[\frac{\eta \tau N Q}{\Gamma(\frac{2}{\gamma})} \right]_S} \frac{J_j^I}{J_j^S} \quad (105)$$

In order to estimate the variance of a hydrogen determination from an epithermal die-away measurement in the Venusian atmosphere, we use the prediction analysis version of Eq. (80):

$$\hat{\sigma}_{\rho_H}^2 = F_Y^2 \hat{\sigma}_Y^2 + F_{\rho_E}^2 \hat{\sigma}_{\rho_E}^2 + \epsilon^2 \quad (106)$$

Predicted values of F_Y^2 , $F_{\rho_E}^2$, and ϵ^2 must be obtained from assumptions about the nature of the atmosphere and from a determination of the constants a_1 - a_6 in Eq. (68) appropriate to the infinite medium problem. A predicted value of $\hat{\sigma}_{\rho_E}^2$ must come from an analysis similar to the present one for the gamma-ray spectral portions of the CPNE. The method of predicting values of $\hat{\sigma}_Y^2$ is discussed below.

A general treatment of the prediction of variance for situations for which an exponential decay model is valid is given in Chap. 6 of the book by Wolberg.⁽⁴⁾ We have assumed that the epithermal die-away data will be analyzed over the range 40 to 60 μ sec by using the form

$$Y(t) = Ae^{-\gamma t} \quad (107)$$

and least squares fitting $\ln Y$ to a linear relation in t to determine y . For the above form, Wolberg shows that the predicted values of the matrix elements, C_{kl} , defined in Eq. (10), are as follows:

$$\hat{C}_{11} = \sum_{i=1}^n \frac{e^{-2yt_i}}{\sigma_{Y_i}^2} \quad (108)$$

$$\hat{C}_{12} = \hat{C}_{21} = \sum_{i=1}^n -\frac{At_i e^{-2yt_i}}{\sigma_{Y_i}^2} \quad (109)$$

$$\hat{C}_{22} = \sum_{i=1}^n \frac{A^2 t_i^2 e^{-2yt_i}}{\sigma_{Y_i}^2} \quad (110)$$

In the above equations it has been assumed that there is no error in the independent variable, t_i , and that it is measured in channels rather than time. Since 1- μ sec channels are usually used for the epithermal die-away measurement, the numerical value of y will be the same, whether measured in $(\mu\text{sec})^{-1}$ or $(\text{channels})^{-1}$. The quantity n is the number of data points used and $\sigma_{Y_i}^2$ is the predicted variance on the accumulated count in channel i representing the die-away signal.

Since there may be a non-negligible time-independent background present (e.g. from an RTG), we assume that the observed count in channel i is C_i , where

$$C_i = Y_i + b, \quad (111)$$

and b is an average background per channel determined from the portion of the data immediately preceding the fast neutron burst. This quantity would be determined by averaging the observed counts in some number, say m , of channels:

$$b = \frac{1}{m} \sum_{j=1}^m C_j \quad (112)$$

Now we have

$$Y_i = C_i - b$$

and by the law of propagation of errors,

$$\sigma_{Y_i}^2 = \sigma_{C_i}^2 + \sigma_b^2 \quad (113)$$

But

$$\sigma_{C_i}^2 = C_i$$

and

$$\sigma_b^2 = \sum_{j=1}^m \left(\frac{\partial b}{\partial c_j} \sigma_{c_j} \right)^2$$

$$= \frac{1}{m^2} \sum_{j=1}^m \sigma_{c_j}^2$$

$$= \frac{1}{m^2} \sum_{j=1}^m c_j$$

$$= \frac{b}{m}$$

Therefore,

$$\sigma_{Y_i}^2 = c_i + \frac{b}{m}$$

$$= Y_i + \left(1 + \frac{1}{m}\right)b$$

Finally,

$$\widehat{\sigma_{Y_i}^2} = \widehat{Y_i} + \left(1 + \frac{1}{m}\right)\widehat{b}$$

$$= \widehat{Ae^{-\widehat{Y}t_i}} + \left(1 + \frac{1}{m}\right)\widehat{b}$$

(114)

Equation (114) is to be used in Eqs. (108) - (110).

The sums in \hat{C}_{11} , \hat{C}_{12} , and \hat{C}_{22} are difficult to evaluate. However Wolberg points out that, if the independent variable values are evenly spaced, to a sufficiently good approximation we can write

$$\hat{C}_{11} = \sum_{i=1}^n \frac{e^{-2\hat{y}t_i}}{\hat{A}e^{-\hat{y}t_i} + (1 + \frac{1}{m})\hat{b}} \quad (115)$$

$$= n \left[\frac{e^{-2\hat{y}t}}{\hat{A}e^{-\hat{y}t} + (1 + \frac{1}{m})\hat{b}} \right]_{\text{average}} \quad (116)$$

$$\approx \frac{n}{t_b - t_a} \int_{t_a}^{t_b} \frac{e^{-2\hat{y}t}}{\hat{A}e^{-\hat{y}t} + (1 + \frac{1}{m})\hat{b}} dt, \quad (117)$$

where t_a and t_b are given by

$$t_a = t_1 - \frac{\tau}{2} \quad (118)$$

$$t_b = t_n + \frac{\tau}{2} \quad (119)$$

In Eqs. (118) and (119), τ is the channel length. If the convention is made that, insofar as the least squares fitting of Eq. (107) to the data is concerned, the first channel used in the fit will be channel 1, and we assume that 1- μ sec channels will be used, we have

$$\hat{c}_{11} \approx \int_{0.5}^{n+0.5} \frac{e^{-2\hat{\gamma}t}}{\hat{A}e^{-\hat{\gamma}t} + (1 + \frac{1}{m})\hat{b}} dt \quad (120)$$

Similarly, the following approximate expressions for \hat{c}_{12} and \hat{c}_{22} may be obtained:

$$\hat{c}_{12} \approx -A \int_{0.5}^{n+0.5} \frac{te^{-2\hat{\gamma}t}}{\hat{A}e^{-\hat{\gamma}t} + (1 + \frac{1}{m})\hat{b}} dt \quad (121)$$

$$c_{22} \approx A^2 \int_{0.5}^{n+0.5} \frac{t^2 e^{-2\hat{\gamma}t}}{\hat{A}e^{-\hat{\gamma}t} + (1 + \frac{1}{m})\hat{b}} dt \quad (122)$$

A predicted estimate of σ_y^2 can be obtained from the matrix elements

\hat{c}_{11} , \hat{c}_{12} , and \hat{c}_{22} as follows:

$$\hat{\sigma}_y^2 = \hat{c}_{22}^{-1} = \frac{\hat{c}_{11}}{\hat{c}_{11} \cdot \hat{c}_{22} - \hat{c}_{12}^2} \quad (123)$$

In principle, an estimate of the variance of a hydrogen determination from an epithermal die-away measurement in the Venusian atmosphere can be made by using Eqs. (105), (106), (120), (121), (122), and (123). Although time did not permit us to carry out any numerical calculations, we feel that the foregoing analysis is reasonable and could provide meaningful results if and when it seems desirable and justifiable to obtain them.

Analyses similar to the foregoing could be carried out for the thermal die-away and gamma-ray spectral measurements. These analyses will probably be more complicated than the epithermal die-away problem, but at the least the above approach might serve as a model upon which the other analyses could be based. Active work in this area will have to await the decisions required to commit the necessary funds and manpower to the task.

VI. MISCELLANEOUS TOPICS

A. Neutron Output Monitor

The possibility and desirability of remotely measuring the neutron output of the neutron generator which will be used in the CPNE has been discussed informally in the past among the experimenters. Such a measurement could be useful in several ways. It would provide a positive indication of how the generator was performing. A comparison between observed counting rates in the parts of the CPNE and the measured neutron output could yield some additional information about the surface being analyzed that is not available otherwise. Finally, normalization of measurements made in the CPNE to a known neutron output would allow direct comparisons among several sites which were analyzed in a mission that employed some type of roving vehicle or similar means for carrying out multi-site analyses.

In laboratory measurements with the Sandia generator, the neutron output has been measured by either activation of Cu foils through the Texas Convention⁽¹⁶⁾ or activation of F in Teflon cylinders, followed by counting in a NaI well crystal.⁽²⁾ Clearly such methods are impossible for remote applications of the CPNE. A satisfactory monitoring method must be an integral part of the CPNE probe and must be capable of operating within the overall constraints of the experiment.

We have done some preliminary tests on a monitoring method which would utilize the $^3\text{He}/\text{Cd}$ detector used for the epithermal die-away measurement. The only additional items required to make the monitoring measure-

ment would be a pulse height discriminator and a scaler. The method is based on detecting 14-Mev neutrons produced by the generator by means of ^3He recoils from the $^3\text{He}(n,n)^3\text{He}$ elastic scattering reaction. From the mechanics of elastic scattering, the maximum energy which would be imparted by a neutron with energy E to a nucleus of mass M (relative to the neutron mass) is (5)

$$E_{\text{max}} = \left[1 - \left(\frac{M-1}{M+1} \right)^2 \right] E \quad (124)$$

For $M=3$ and $E=14$ Mev, this gives $E_{\text{max}}=10.5$ Mev. The reaction by which epithermal neutrons are detected is $^3\text{He}(n,p)^3\text{H}$, which has a Q -value of 0.77 Mev. (17) Since epithermal neutrons bring very little kinetic energy to the reaction, the pulses produced in the ^3He detector from them are much smaller than those from the ^3He recoils due to 14-Mev neutrons. Pulses from the recoils will extend from 10.5 Mev down to zero, and some reasonable bias level, corresponding to a lower energy value, must be selected in order to achieve adequate counting rates. The question that then must be answered is whether this lower bias level will permit fast neutrons which have been scattered off the surface being analyzed (and possibly off of various structural parts of the probe) to be detected in sufficient quantity as to cause the proposed monitoring scheme to be too environment sensitive.

In order to investigate the possibilities of realizing the method

proposed above, the $^3\text{He}/\text{Cd}$ detector used in the epithermal die-away measurements described in section III-B was set up near the Van de Graaff target in a position identical to that used for the epithermal experiments. Initially the small tank was empty. A pulse height spectrum of pulses from the $^3\text{He}/\text{Cd}$ detector was taken with the Van de Graaff producing 14-Mev neutrons in a steady state condition. This spectrum is shown as solid points in Fig. 41. For comparison purposes, an Am-Be source was put in a paraffin moderator and the spectrum of pulses recorded. These data are shown as open circles in Fig. 41. The spectra have been normalized to equal intensity at channel 20.

The spectrum from the moderated Am-Be source shows the familiar epithermal distribution rising to a peak at channel 20, which corresponds to an energy of 0.77 Mev, and then dropping rapidly to a component which tails off to higher energies and presumably results from detection of fast neutrons which have escaped from the moderator. The spectrum from the D-T neutron source shows an intense continuum which monotonically decreases towards higher energy. It was decided to use a bias level corresponding to 3 Mev to carry out the ensuing monitor tests.

With the $^3\text{He}/\text{Cd}$ detector positioned over the empty tank, a series of runs was made at various beam currents on the Van de Graaff. For each run, a Teflon cylinder in our standard monitoring position was exposed and counted in the NaI well crystal to measure the neutron output. Following this, the small tank was filled with crushed granite

and the $^3\text{He}/\text{Cd}$ detector repositioned exactly the same as in the runs with the empty tank. A series of runs was made at various beam currents and the neutron output monitored by Teflon activation.

All observed count rates were corrected for background and each of the two sets of data were fitted to the form

$$^3\text{He recoils} = k(^{18}\text{F counts}).$$

The values of k were as follows:

$$\text{Empty tank: } k = 0.96 \pm 0.04$$

$$\text{Granite filled: } k = 1.15 \pm 0.06$$

There thus seems to be a statistically significant environmental effect on the high energy ^3He -recoil monitor. It is in the expected direction, since the presence of the granite will scatter some fast neutrons into the $^3\text{He}/\text{Cd}$ detector and increase the ^3He recoil counts, thus increasing the observed value of k . Since the effect is only about 20%, this might be an acceptable influence. The high-energy bias point could also be raised to diminish the environmental effect, but at the expense of ^3He recoil counting rate.

The standard conditions which were used in these tests were as follows: 1" active diameter by 4" active length, 10 atm. $^3\text{He}/\text{Cd}$ detector; cylindrical axis of detector passed through ^3H target at 0° to the $^2\text{H}^+$

beam; geometrical center of detector located 11.4 cm. from the target. Under these conditions, we observed a monitoring sensitivity of 6.75×10^5 neutrons/ ^3He recoil count. For the anticipated combinations of repetition rates and neutron output per burst, we estimate that the above sensitivity would lead to approximately 100 ^3He recoil counts per minute. Unless the ambient fast neutron background is unusually high, this should be an acceptable counting rate. The possibility of using a monitoring technique based on the foregoing approach should be considered for the future.

B. Flight-Qualified ^3He Detector

One problem which we had not specifically looked into during the Phase I and II work is the availability of flight-qualified ^3He detectors of the type needed to do the epithermal die-away measurement. As a result of an inquiry made in July 1970, it was learned that such detectors are available from Reuter-Stokes of Cleveland, Ohio. A series of Reuter-Stokes' Model RS-P4-0806-10 detectors were tested by Reuter-Stokes under contract to TRW, Inc., and passed all requirements for space flight. This detector model has a 1" active diameter and an active length of up to 8". ^3He fill pressures up to 20 atm. are available.

As a result of the CPNE meeting at Sandia Laboratories in June, 1971, it appears that a 1" diam. x 6 or 8" active length ^3He detector would not fit into the new CPNE probe which is being designed as well as a detector which has a shorter active length and a larger diameter.

By keeping the volume of ^3He gas approximately the same, however, it should be possible to keep the epithermal neutron counting rate unchanged.

A second inquiry was made of Reuter-Stokes, and they stated that a Model SK-678 could be modified to meet our requirements. Two versions were suggested: a $1\frac{1}{2}$ in. diam. x 3 in. length counter or a $1\frac{1}{2}$ in. diam. x $4\frac{1}{2}$ in. length counter. Either one could be filled with 10 atm. of ^3He plus a small amount of CO_2 , and would operate at less than 2000 volts. It appears that the shorter detector is probably most suitable from the standpoint of dimensional considerations in the new probe.

VII. SUMMARY

It is evident from the nature of this report that our main occupation during the work of Phase III has been in the area of data analysis and interpretation of the epithermal and thermal neutron die-away measurements. By and large, our efforts have been successful. Although it would have been desirable to carry out an experimental calibration of the epithermal die-away measurement, we feel that the theoretically-based data analysis procedure which has been devised is adequate for the immediate application at hand, viz., the analysis of data which will be obtained with the new lightweight CPNE probe. The successful analysis of the thermal neutron and capture gamma-ray die-away data, and the unravelling of the problems associated with it, is particularly gratifying since this situation had represented something of a "thorn-in-the-side" matter to us since the work done in Phase I. Analysis of thermal neutron capture gamma-ray die-away data obtained with the new CPNE probe in the upcoming field test will be carried out by the technique described in the present report.

Some problems associated with the die-away measurements remain which need working on, but these are not regarded as having sufficiently high priority to justify proposing another phase of work in the near future. Rather, these can be reconsidered at the time, if and when, the CPNE is taken off the shelf to get it prepared for a campaign to have it accepted for use on a suitable approved mission. Specific problems which could be worked on are as follows:

1. The basic method of analyzing the epithermal neutron die-away data should be extended, probably on the basis of theoretical work, in order to permit more of the data obtained in a measurement to be used in the analysis.
2. The finite theory of epithermal die-away must be worked out for a true three-dimensional cylinder before a combined experimental and theoretical calibration can be satisfactorily carried out.
3. Actual calculations involving prediction of variance should be carried out for both epithermal and thermal die-away for cases of future interest.

LIST OF SYMBOLS

- Y_i = observed value of the dependent variable at the i 'th data point.
- σ_{Y_i} = standard deviation of Y_i .
- X_{ji} = observed value of the j 'th independent variable at the i 'th data point.
- $\sigma_{X_{ji}}$ = standard deviation of X_{ji} .
- y_i = calculated (or adjusted) value of the dependent variable at the i 'th data point.
- x_{ji} = calculated (or adjusted) value of the j 'th independent variable at the i 'th data point.
- η_i = true (or mean) value of the dependent variable at the i 'th data point.
- ξ_{ji} = true (or mean) value of the j 'th independent variable at the i 'th data point.
- n = number of data points.
- m = number of independent variables.
- a_k = calculated values of the unknown parameters.
- α_k = true values of the unknown parameters.
- σ_{a_k} = standard deviation of a_k .
- s_{a_k} = unbiased estimate of σ_{a_k} .
- p = number of unknown parameters.

- v = neutron speed.
- v_0 = speed of source neutrons.
- u = neutron lethargy.
- Σ = macroscopic scattering cross section
- D = diffusion coefficient.
- ξ = average logarithmic energy decrement per collision.
- γ = characteristic constant defined in equation (41).
- σ = microscopic scattering cross section.
- M = mass of nucleus/mass of neutron.
- w = weight fraction of element.
- d = extrapolation distance.
- Γ = gamma function.
- ψ = digamma function.

REFERENCES

1. W. R. Mills and W. W. Givens, "Neutron Die-Away Experiment for Lunar and Planetary Surface Analysis", Final Report - Phase I, 26 July 1966-26 March 1967, Mobil Oil Corporation.
2. W. R. Mills and W. W. Givens, "Neutron Die-Away Experiment for Lunar and Planetary Surface Analysis - Phase II", 3 July 1967-28 June 1969, Mobil Research and Development Corporation.
3. J. H. Reed and J. W. Mandler, "Compositional Analysis of Lunar and Planetary Surfaces Using Neutron Capture Gamma Rays", July 1, 1968 to March 31, 1970, Report No. IITRI-V6032-16, IIT Research Institute, April, 1970.
4. J. R. Wolberg, Prediction Analysis, D. Van Nostrand Co., Inc. (1967).
5. S. Glasstone and M. C. Edlund, The Elements of Nuclear Reactor Theory, D. Van Nostrand Co., Inc., p. 144, (1952).
6. D. J. Hughes and R. B. Schwartz, eds., Neutron Cross Sections, BNL-325, Second Edition, July 1, 1958.
7. J. Green, "Geochemical Table of the Elements for 1959", Bull. of the Geol. Soc. of Amer. 70, 1127-1184, Sept. (1959).
8. J. W. Meadows and J. F. Whalen, "Thermal Neutron Absorption Cross Sections by the Pulsed Source Method", Nuc. Sci. & Eng. 9, 132-136 (1961).
9. D. J. Behrens, "Some Notes on the Nature of Experiments, on the Statistics of Counting, and on the Fitting of Exponential Decay to the Results of Counting Experiments", AERE T/R 629, Atomic Energy Research Establishment, Harwell, Berks., England (1951).
10. E. Martinho and M. M. Costa Paiva, "Thermal-Neutron Diffusion Parameters in Water by the Poisoning Method", Nuc. Sci. & Eng. 45, 308-313 (1971).
11. CO-OP Class/Index Code E2 WISC GAUSHAUS, "Non-Linear Least Squares (GAUSHAUS)", contributed by University of Wisconsin Computing Center.
12. J. A. Waggoner and R. J. Knox, "Elemental Analysis Using Neutron Inelastic Scattering", UCRL-14654, Rev. 1, Lawrence Radiation Laboratory, University of California, Livermore, December 1, 1968.

13. J. H. Reed, J. W. Mandler, and D. L. Riley, "Continued Development of the Combined Pulsed Neutron Experiment (CPNE) for Lunar and Planetary Surfaces", June 15, 1971 to December 15, 1971, Report No. IITRI-V6121-1, IIT Research Institute, January 15, 1972.
14. D. M. Hunten and R. M. Goody, "Venus: The Next Phase of Planetary Exploration", *Science* 165, 1317-1323, 26 September 1969.
15. V. P. Vinogradov, et. al., "Chemical Composition of the Venus Atmosphere", V. I. Vernadsky Institute of Geochemistry and Analytical Chemistry, USSR Academy of Sciences, (1969).
16. J. H. Reed, "Compositional Analysis of Lunar and Planetary Surfaces Using Neutron Capture Gamma Rays", May 1, 1966 to June 30, 1967, Report No. IITRI-A6155-5, IIT Research Institute, July 1, 1967.
17. J. B. Marion and J. L. Fowler, eds., Fast Neutron Physics, Part I, Section III. C, Interscience Publishers, Inc., New York (1960).

APPENDIX 1

We wish to solve the Boltzmann transport equation for the semi-infinite slab shown in the upper part of Fig. 13. This problem is similar to the three-dimensional problem solved previously⁽²⁾ and the solution outlined below will lean heavily on the exposition given in Appendix 3 of Reference 2.

The same assumptions and boundary conditions are used in the one-dimensional problem as in the three-dimensional one. With definitions and notation the same as used before, the equation to be solved along with the appropriate boundary conditions is as follows:

$$\frac{1}{v_0} e^{\frac{u}{2}} \frac{\partial \phi}{\partial t} + \Sigma \phi - D \frac{\partial^2 \phi}{\partial z^2} =$$

$$\Sigma \int_0^u \left[\frac{\xi}{\gamma^2} e^{\frac{u'-u}{\gamma}} + \left(1 - \frac{\xi}{\gamma}\right) \delta(u'-u) \right] \phi \, du' + \delta(z-d) \delta(u) \delta(t) \quad (\text{A1.1})$$

$$\phi(0, u, t) = \phi(z, u, 0) = 0$$

$$\lim_{z \rightarrow \infty} \phi(z, u, t) = \lim_{z \rightarrow \infty} \frac{\partial \phi}{\partial z} = 0$$

In Eq. (A1.1) we have explicitly assumed a unit plane impulse source located at $z=d$. The second part of the integral in Eq. (A1.1) can be

carried out, and the equation to be solved becomes

$$\frac{1}{v_0} e^{\frac{u}{2}} \frac{\partial \phi}{\partial t} + \frac{\xi \Sigma}{\gamma} \phi - D \frac{\partial^2 \phi}{\partial z^2} = \frac{\xi \Sigma}{\gamma^2} \int_0^u e^{\frac{u'-u}{\gamma}} \phi du' + \delta(z-d) \delta(u) \delta(t) \quad (\text{A1.2})$$

Define the Laplace transform of ϕ with respect to t and the Fourier sine transform with respect to z by

$$\phi^{LF}(k, u, s) = \sqrt{\frac{2}{\pi}} \int_0^\infty \sin kzdz \int_0^\infty e^{-st} \phi(r, z, u, t) dt$$

Taking the Laplace - Fourier transform of Eq. (A1.2), and using the boundary and initial conditions and well-known properties of the transforms, we obtain

$$\left(\frac{s}{v_0} e^{\frac{u}{2}} + \frac{\xi \Sigma}{\gamma} + Dk^2 \right) \phi^{LF} = \frac{\xi \Sigma}{\gamma^2} \int_0^u e^{\frac{u'-u}{\gamma}} \phi^{LF} du' + \sqrt{\frac{2}{\pi}} \sin kd \delta(u) \quad (\text{A1.3})$$

Define a new function ψ^{LF} by

$$\psi^{LF} = \phi^{LF} - \sqrt{\frac{2}{\pi}} \frac{\sin kd \delta(u)}{\frac{se^{\frac{u}{2}}}{v_0} + \frac{\xi \Sigma}{\gamma} + Dk^2} \quad (\text{A1.4})$$

Substituting ϕ^{LF} from Eq. (A1.4) into Eq. (A1.3) gives

$$\left(\frac{se^{\frac{u}{2}}}{v_0} + \frac{\xi \Sigma}{\gamma} + Dk^2 \right) \psi^{LF} =$$

$$\frac{\xi \Sigma}{\gamma^2} \int_0^u e^{\frac{u'-u}{\gamma}} \psi^{LF} du' + \sqrt{\frac{2}{\pi}} \frac{\xi \Sigma}{\gamma^2} \frac{e^{-\frac{u}{\gamma}} \sin kd}{\frac{s}{v_0} + \frac{\xi \Sigma}{\gamma^2} + Dk^2} \quad (A1.5)$$

The next series of steps in the solution is formally identical with those following Eq. (A3.6) in Appendix 3 of Reference 2. Noting that ψ and ϕ differ only at zero lethargy and recalling the fact that the $^3\text{He}/\text{Cd}$ detector response is essentially negligible at $u=0$, we have the analog of Eq. (A3.9) of Reference 2:

$$\phi(z, v, t) = \frac{2}{\pi} e^{-\frac{\xi \Sigma v t}{\gamma}} I(z, v, t) \quad (A1.6)$$

where

$$I(z, v, t) = \int_0^\infty dk \sin kz \sin kd e^{-v D t k^2} g(k)$$

and

$$g(k) = \frac{\left[vt \left(\frac{\xi \Sigma}{\gamma} + Dk^2 \right) \left(\frac{v}{v_0} \right)^{\frac{D\gamma k^2}{\xi \Sigma}} \right]^{\frac{2\xi \Sigma}{\gamma^2 \left(\frac{\xi \Sigma}{\gamma} + Dk^2 \right)}}}{\Gamma \left[\frac{2\xi \Sigma}{\gamma^2 \left(\frac{\xi \Sigma}{\gamma} + Dk^2 \right)} \right]}$$

In obtaining Eq. (A1.6) we have changed variables from lethargy to velocity by using the relation

$$\phi(z, v, t) = \phi(z, u, t) \left| \frac{du}{dv} \right|$$

It is convenient to change the variable of integration in the expression for $l(z, v, t)$ to $x^2 = vDt k^2$. When this is done we have finally

$$\phi(z, v, t) = \frac{2}{\pi} \frac{e^{-\frac{\xi \Sigma vt}{\gamma}}}{(vDt)^{\frac{1}{2}}} \int_0^{\infty} dx \sin\left(\frac{z}{\sqrt{vDt}} x\right) \sin\left(\frac{d}{\sqrt{vDt}} x\right) e^{-x^2} g(x) \quad (\text{A1.7})$$

where

$$g(x) = \frac{\left[\left(\frac{\xi \Sigma v t}{\gamma} + x^2 \right) \left(\frac{v}{v_0} \right)^{\frac{\gamma}{\xi \Sigma v t} x^2} \right]}{\Gamma \left(\frac{2/\gamma}{1 + \frac{\gamma}{\xi \Sigma v t} x^2} \right)} \quad (\text{A1.8})$$

It should be remarked, as a point of comparison, that the closed form expression for $\phi(r, z, v, t)$ which is given in Eq. (A3.12) in Reference 2 was obtained by writing $g(x)$ as $e^{-f(x)}$, expanding $f(x)$ in a Taylor's series about $x=0$, and retaining terms through x^2 . The accuracy of this approximation was unknown and, consequently, the usefulness of the closed form solution remained to be demonstrated. We avoid the above approximation in this treatment and leave $\phi(z, v, t)$ in the form given by Eq. (A1.7).

APPENDIX 2

In this appendix we wish to solve the Boltzmann transport equation for the finite slab shown in the lower part of Fig. 13. The basic equation to be solved is Eq. (A1.1). The boundary and initial conditions are

$$\phi(0, u, t) = \phi(a, u, t) = 0$$

$$\phi(z, u, 0) = 0.$$

Define the Laplace transform of ϕ with respect to t by

$$\phi^L(z, u, s) = \int_0^{\infty} e^{-st} \phi(z, u, t) dt$$

Taking the Laplace transform of Eq. (A1.2) and using the initial condition we obtain

$$\left(\frac{s}{v_0} e^{\frac{u}{2}} + \frac{\xi \Sigma}{\gamma} \right) \phi^L - D \frac{\partial^2 \phi^L}{\partial z^2} = \frac{\xi \Sigma}{\gamma^2} \int_0^u e^{\frac{u'-u}{\gamma}} \phi^L du' + \delta(u) \delta(z-d) \quad (\text{A2.1})$$

In order to satisfy the boundary conditions at $z=0$ and $z=a$, we try a Fourier series solution of the following form:

$$\phi^L(z, u, s) = \sum_{n=1}^{\infty} \phi_n(u, s) \sin\left(\frac{n\pi z}{a}\right) \quad (\text{A2.2})$$

It is also necessary to expand $\delta(z-d)$ in a Fourier series:

$$\delta(z-d) = \sum_{n=1}^{\infty} A_n \sin\left(\frac{n\pi z}{a}\right)$$

By a straightforward calculation, we find

$$A_n = \frac{2}{a} \sin\left(\frac{n\pi d}{a}\right)$$

Substitution of the above quantities in Eq. (A2.1) yields the following equation which must be satisfied by $\phi_n(u, s)$:

$$\left[\frac{s}{v_0} e^{\frac{u}{2}} + \frac{\xi \Sigma}{\gamma} + D \left(\frac{n\pi}{a} \right)^2 \right] \phi_n(u, s) = \frac{\xi \Sigma}{\gamma} \int_0^u e^{\frac{u'-u}{\gamma}} \phi_n(u', s) du' + \frac{2}{a} \sin\left(\frac{n\pi d}{a}\right) \delta(u) \quad (\text{A2.3})$$

Define a new function $\psi_n(u, s)$ by

$$\psi_n(u, s) = \phi_n(u, s) - \frac{2}{a} \sin\left(\frac{n\pi d}{a}\right) \frac{\delta(u)}{\frac{s}{v_0} e^{\frac{u}{2}} + \frac{\xi\Sigma}{\gamma} + D\left(\frac{n\pi}{a}\right)^2} \quad (\text{A2.4})$$

Substituting $\phi_n(u, s)$ from Eq. (A2.4) into Eq. (A2.3) gives the following equation to be solved for $\psi_n(u, s)$:

$$\left[\frac{s}{v_0} e^{\frac{u}{2}} + \frac{\xi\Sigma}{\gamma} + D\left(\frac{n\pi}{a}\right)^2 \right] \psi_n(u, s) = \frac{\xi\Sigma}{\gamma^2} \int_0^u e^{-\frac{u'-u}{\gamma}} \psi_n(u', s) du' + \frac{2}{a} \frac{\xi\Sigma}{\gamma^2} \sin\left(\frac{n\pi d}{a}\right) \frac{e^{-\frac{u}{\gamma}}}{\frac{s}{v_0} + \frac{\xi\Sigma}{\gamma} + D\left(\frac{n\pi}{a}\right)^2} \quad (\text{A2.5})$$

From this point on in the development, as in Appendix 1, the series of steps is formally the same as those following Eq. (A3.6) in Appendix 3 of Reference 2. Again noting that ψ_n and ϕ_n differ only at zero lethargy where the $^3\text{He}/\text{Cd}$ detector response is very small, the analog of Eq. (A1.6) in the preceding appendix is

$$\phi(z, v, t) = \frac{2}{a} e^{-\frac{\xi\Sigma vt}{\gamma}} \sum_{n=1}^{\infty} \sin\left(\frac{n\pi d}{a}\right) \sin\left(\frac{n\pi z}{a}\right) e^{-vDt} \left(\frac{n\pi}{a}\right)^2 h_n(v, t) \quad (\text{A2.6})$$

where

$$h_n(v, t) = \frac{\left\{ \left[\frac{\xi \Sigma v t}{\gamma} + v D t \left(\frac{n\pi}{a} \right)^2 \right] \left(\frac{v}{v_0} \right)^{\frac{D\gamma}{\xi \Sigma} \left(\frac{n\pi}{a} \right)^2} \right\} \left[\frac{2/\gamma}{1 + \frac{D\gamma}{\xi \Sigma} \left(\frac{n\pi}{a} \right)^2} \right]}{\Gamma \left[\frac{2/\gamma}{1 + \frac{D\gamma}{\xi \Sigma} \left(\frac{n\pi}{a} \right)^2} \right]} \quad (\text{A2.7})$$

Similar to the final result given by Eqs. (A1.7) and (A1.8) in Appendix 1, no approximations have been made in arriving at Eqs. (A2.6) and (A2.7) that are not reasonable and of an estimable accuracy.

TABLE 1 - VALUES OF NEUTRON-NUCLEUS CONSTANTS

Element	M_i	ξ_i	γ_i	σ_i (Barns)	r_i	$\frac{r_i}{r_o}$	$\frac{r_i \xi_i}{r_o \xi_o}$	$\frac{r_i \xi_i \gamma_i}{r_o \xi_o \gamma_o}$
H	1	1.000	1.000	21	12.64	-	-	-
C	12	0.158	0.108	4.7	0.236	1.65	2.17	2.87
O	16	0.120	0.0816	3.8	0.143	1.00	1.00	1.00
Na	23	0.0845	0.0571	3.3	0.0864	0.604	0.426	0.298
Mg	24	0.0811	0.0548	3.5	0.0878	0.614	0.415	0.279
Al	27	0.0723	0.0488	1.4	0.0312	0.218	0.131	0.0783
Si	28	0.0698	0.0470	2.2	0.0473	0.331	0.193	0.111
K	39	0.0504	0.0339	2.0	0.0309	0.216	0.0907	0.0377
Ca	40	0.0492	0.0330	3.0	0.0452	0.316	0.130	0.0524
Fe	56	0.0353	0.0237	11.5	0.124	0.867	0.255	0.0741

TABLE 2 - SUMMARY OF THEORETICAL EPITHERMAL
DIE-AWAY CALCULATIONS

Rock Type	ρ	w_H	ρ_H	ρ_Σ	ρ_ξ	ρ_γ	y
Basalt	1.5	0	0	1.0425	0.84180	0.75420	0.01329
"	2	0	0	1.3900	1.1224	1.0056	0.01663
"	2.5	0	0	1.7375	1.4030	1.2570	0.02379
"	1.5	0.0015	0.00225	1.0425	0.84180	0.75420	0.05288
"	2	0.0015	0.00300	1.3900	1.1224	1.0056	0.07274
"	2.5	0.0015	0.00375	1.7375	1.4030	1.2570	0.09310
"	1.5	0.0030	0.00450	1.0425	0.84180	0.75420	0.08473
"	2	0.0030	0.00600	1.3900	1.1224	1.0056	0.11446
"	2.5	0.0030	0.00750	1.7375	1.4030	1.2570	0.14420
Granite	1.5	0	0	1.0251	0.90645	0.82650	0.01390
"	2	0	0	1.3668	1.2086	1.1020	0.01820
"	2.5	0	0	1.7085	1.5108	1.3775	0.02883
"	1.5	0.0015	0.00225	1.0251	0.90645	0.82650	0.05491
"	2	0.0015	0.00300	1.3668	1.2086	1.1020	0.07581
"	2.5	0.0015	0.00375	1.7085	1.5108	1.3775	0.09723
"	1.5	0.0030	0.00450	1.0251	0.90645	0.82650	0.08687
"	2	0.0030	0.00600	1.3668	1.2086	1.1020	0.11752
"	2.5	0.0030	0.00750	1.7085	1.5108	1.3775	0.14820
Dunite	1.5	0	0	1.1224	0.93360	0.83325	0.01408
"	2	0	0	1.4966	1.2448	1.1110	0.01885
"	2.5	0	0	1.8708	1.5560	1.3888	0.03117
"	1.5	0.0015	0.00225	1.1224	0.93360	0.83325	0.05572
"	2	0.0015	0.00300	1.4966	1.2448	1.1110	0.07699
"	2.5	0.0015	0.00375	1.8708	1.5560	1.3888	0.09882
"	1.5	0.0030	0.00450	1.1224	0.93360	0.83325	0.08768
"	2	0.0030	0.00600	1.4966	1.2448	1.1110	0.11861
"	2.5	0.0030	0.00750	1.8708	1.5560	1.3888	0.14959

All densities in gm/cc y in units of μsec^{-1}

TABLE 3 - ELEMENTAL COMPOSITIONS OF ROCK MODELS
(WEIGHT PERCENT)

	Burnet Red Granite $\rho = 1.38 \text{ gm/cm}^3$	Texas Rockville Granite $\rho = 2.63 \text{ gm/cm}^3$	Knippa Basalt $\rho = 1.60 \text{ gm/cm}^3$	Dunite, Balsam, N.C. $\rho = 1.75 \text{ gm/cm}^3$
O	47.74 \pm 1.06	47.82 \pm .76	43.95 \pm 2.51	44.12 \pm .97
Si	33.06 \pm .75	32.66 \pm .45	19.13 \pm 1.69	20.37 \pm .27
Al	7.79	8.11	5.53	0.52
Fe	2.24	2.78	9.07	7.04
Ca	0.94	1.30	9.09	0.24
Mg	0.14	0.06	8.53	27.19
Na	3.02	2.95	2.09	0.01
K	3.57	3.77	1.20	0.008
Ti	0.20	0.25	1.92	0.0006
Li	0.001	0.001	0.0017	< 0.00005
B	< 0.0003	< 0.0003	< 0.0003	-
Cl	0.01	0.01	0.01	0.02
P	0.04	0.07	0.37	0.01
H	0.077	0.075	0.316	0.077

TABLE 4 - SUMMARY OF ANALYSIS OF EPITHERMAL
DIE-AWAY DATA

Rock Type	ρ (gm/cc)	ρ_{ξ} (gm/cc)	γ (μsec^{-1})	ρ_H (gm/cc)
Burnet Red Granite	1.38	0.7935	0.0323 ± 0.0037	0.001090
Texas Rockville Granite	2.63	1.517	0.0606 ± 0.0029	0.001533
Knippa Basalt	1.60	0.9024	0.0942 ± 0.0067	0.005017
Dunite	1.75	1.072	0.0485 ± 0.0041	0.001645

TABLE 5 - WEIGHT PERCENT WATER IN ROCK MODELS

	USGS 12-6-67	Mobil FRL (NMR)	Mobil FRL (weight loss)	USGS (Bound) Mobil FRL (absorbed)
Burnet Red Granite				
Absorbed H ₂ O	0.08	-	0.13	0.13
Bound H ₂ O	<u>0.56</u>	<u>-</u>	<u>0.36</u>	<u>0.56</u>
Total H ₂ O	0.64	0.36	0.49	0.69
Texas Rockville Granite				
Absorbed H ₂ O	0.05	-	0.12	0.12
Bound H ₂ O	<u>0.55</u>	<u>-</u>	<u>0.19</u>	<u>0.55</u>
Total H ₂ O	0.60	0.37	0.31	0.67
Knippa Basalt				
Absorbed H ₂ O	0.57	-	0.82	0.82
Bound H ₂ O	<u>2.0</u>	<u>-</u>	<u>1.42</u>	<u>2.0</u>
Total H ₂ O	2.57	0.92	2.24	2.82
Dunite, Balsam, N.C.				
Absorbed H ₂ O	0.05	-	0.03	0.03
Bound H ₂ O	<u>1.0</u>	<u>-</u>	<u>0.61</u>	<u>1.0</u>
Total H ₂ O	1.05	-	0.64	1.03

TABLE 6 - COMPARISON OF ANALYSES OF WATER CONTENT OF ROCK
MODELS DEDUCED FROM DIE-AWAY AND FROM COMBUSTION

Rock Type	$\gamma (\mu\text{sec}^{-1})$	$w_{\text{H}_2\text{O}}$ (%,"BEST" CHEMICAL)	$w_{\text{H}_2\text{O}}$ (%,"DIE-AWAY")
Burnet Red Granite	0.0323 ± 0.0037	0.69	0.71 ± 0.14
Texas Rockville Granite	0.0606 ± 0.0029	0.55	0.52 ± 0.07
Knippa Basalt	0.0942 ± 0.0067	2.82	2.83 ± 0.28
Balsam Dunite	0.0485 ± 0.0041	1.03	0.85 ± 0.13

TABLE 7 - MACROSCOPIC ABSORPTION CROSS SECTIONS FOR ROCK MODELS

<u>Model</u>	$\Sigma_a(\text{CHEM. ANAL.})\text{-cm}^{-1}$	$\Sigma_a(\text{MEASURED})\text{-cm}^{-1}$	<u>Density-gm/cc</u>
Balsam, N.C. Olivine	0.00592	0.00659 ± 0.00030	1.75
Burnet Red Granite	0.00601	0.01149 ± 0.00035	1.38
Knippa Basalt	0.01160	0.01698 ± 0.00030	1.60
Texas Rockville Granite	0.01215	0.02113 ± 0.00049	2.63

TABLE 8 - NEUTRON AGES DETERMINED BY
LEAST-SQUARES FITS TO THERMAL DIE-AWAY DATA

<u>Model</u>	<u>D-cm</u>	<u>$\Sigma_a - \text{cm}^{-1}$</u>	<u>$\theta - \text{cm}^2$</u>	<u>Fit Range - Channels</u>
Balsam, N.C., Olivine	1.55	0.00659	676 \pm 30	74 - 140
Burnet Red Granite	2.17	0.01149	1244 \pm 179	77 - 120
Knippa Basalt	1.33	0.01698	638 \pm 42	64 - 108
Texas Rockville Granite	1.13	0.02113	297 \pm 40	61 - 90

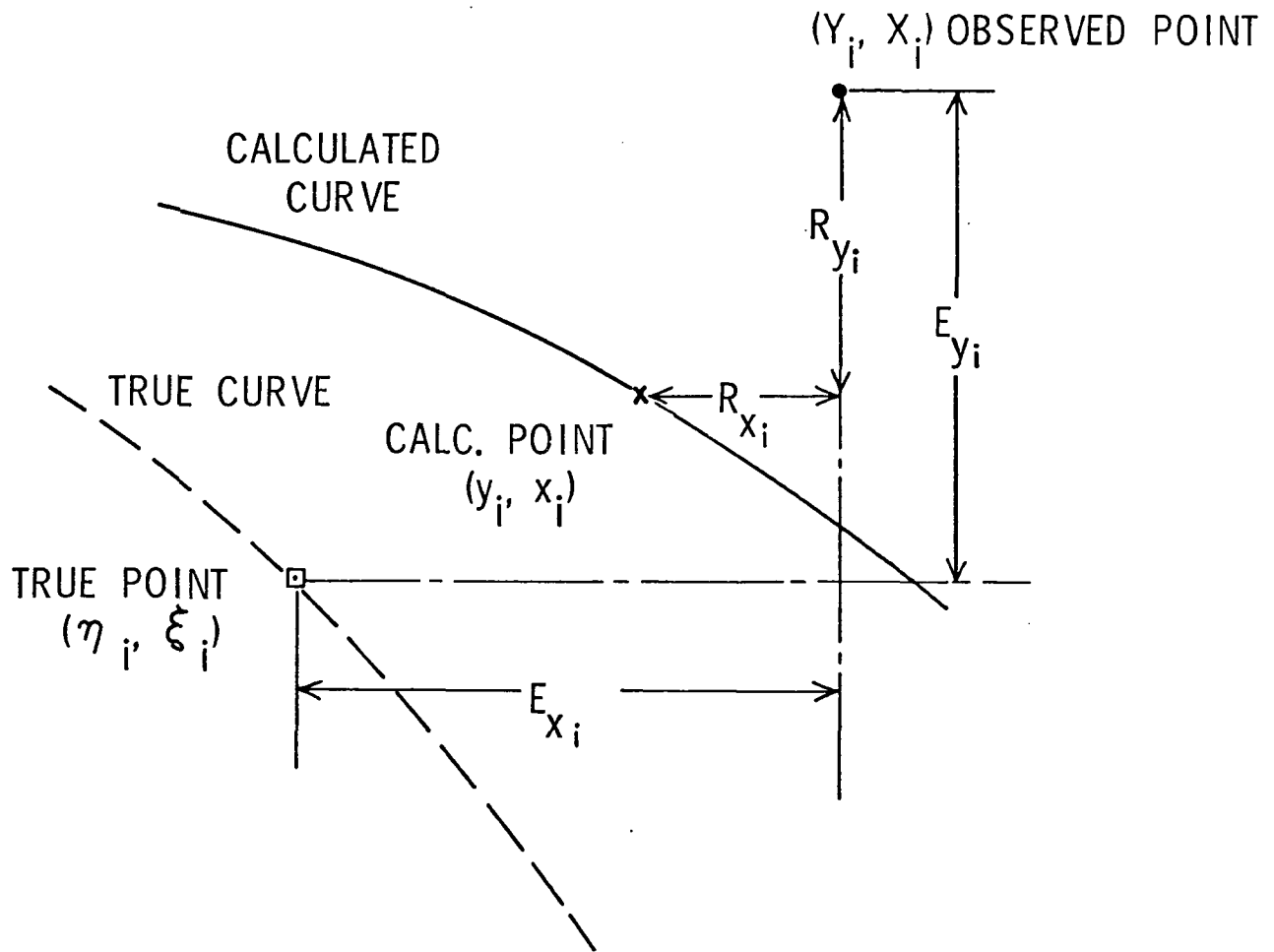


FIGURE 1

TYPICAL DATA ANALYSIS SITUATION (TWO-DIMENSIONAL)
SHOWING RELATION BETWEEN OBSERVED, CALCULATED, AND
TRUE DATA POINTS. R_{y_i} AND R_{x_i} ARE RESIDUALS; E_{y_i} AND E_{x_i} ARE ERRORS.

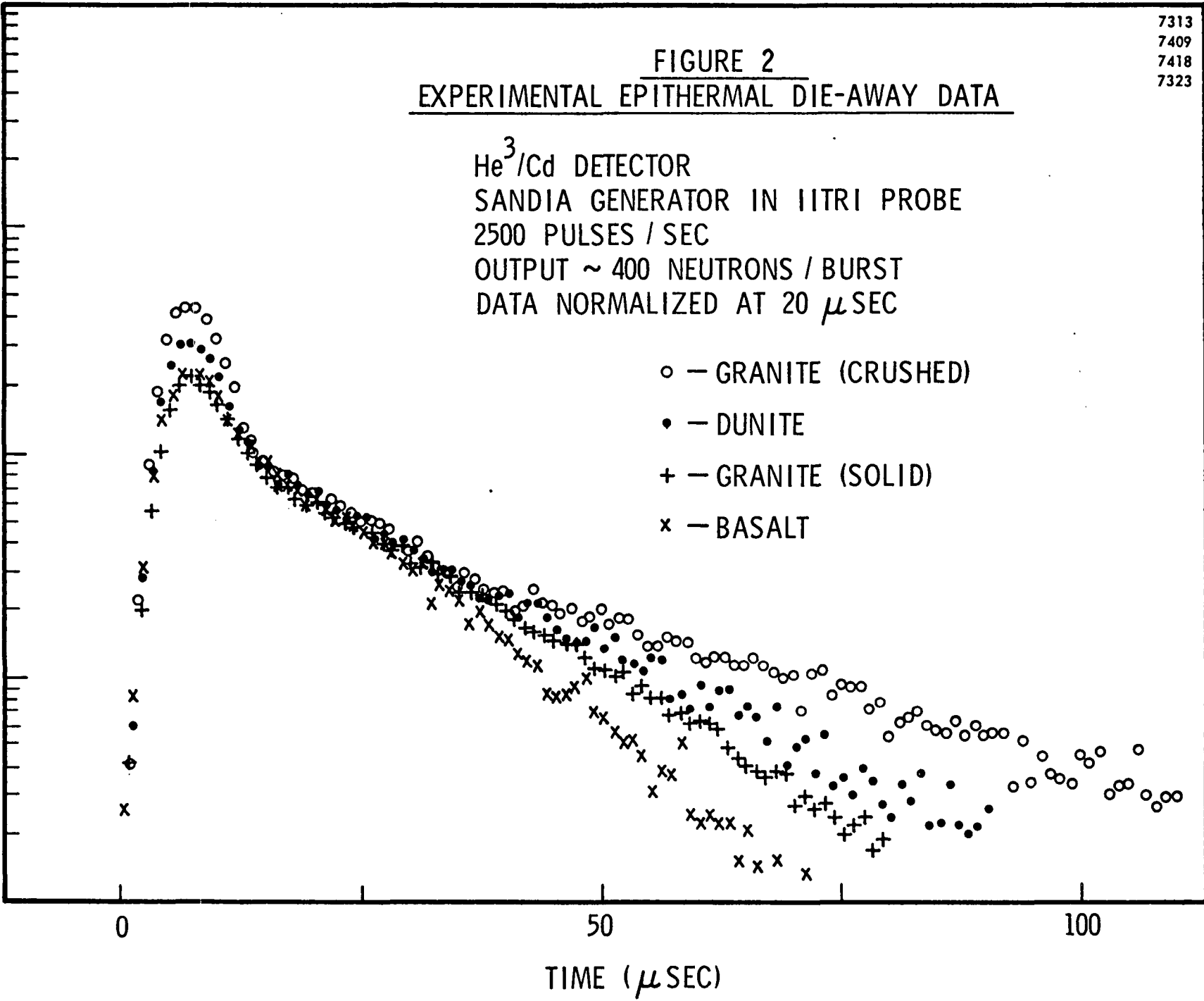
7313
7409
7418
7323

FIGURE 2
EXPERIMENTAL EPITHERMAL DIE-AWAY DATA

He³/Cd DETECTOR
SANDIA GENERATOR IN IITRI PROBE
2500 PULSES / SEC
OUTPUT ~ 400 NEUTRONS / BURST
DATA NORMALIZED AT 20 μSEC

- - GRANITE (CRUSHED)
- - DUNITE
- + - GRANITE (SOLID)
- x - BASALT

COUNTS / 1 μSEC / 30 MIN



0

50

100

TIME (μSEC)

FIGURE 3
EXPERIMENTAL STUDY OF $^3\text{He}/\text{Cd}$ DETECTOR POSITIONS

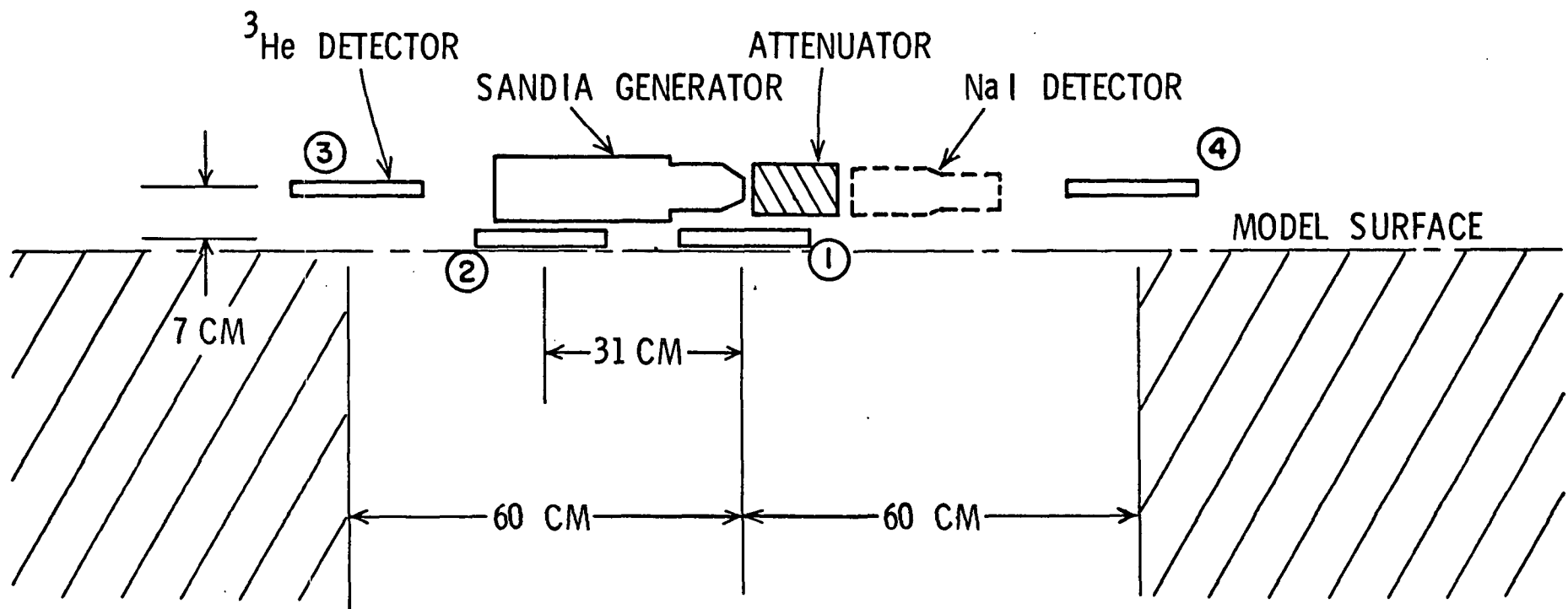
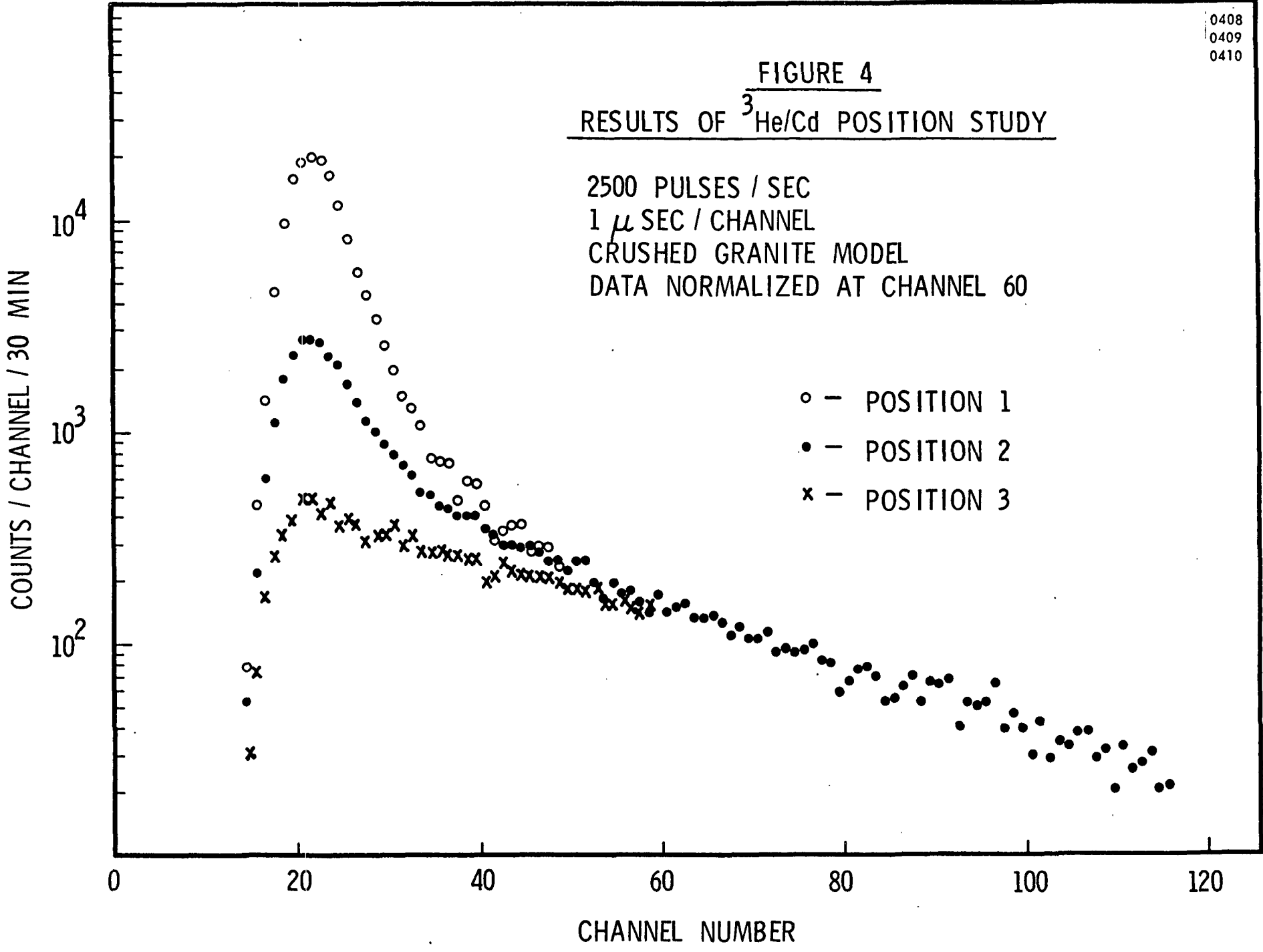


FIGURE 4
RESULTS OF ³He/Cd POSITION STUDY

2500 PULSES / SEC
1 μ SEC / CHANNEL
CRUSHED GRANITE MODEL
DATA NORMALIZED AT CHANNEL 60

- - POSITION 1
- - POSITION 2
- x - POSITION 3



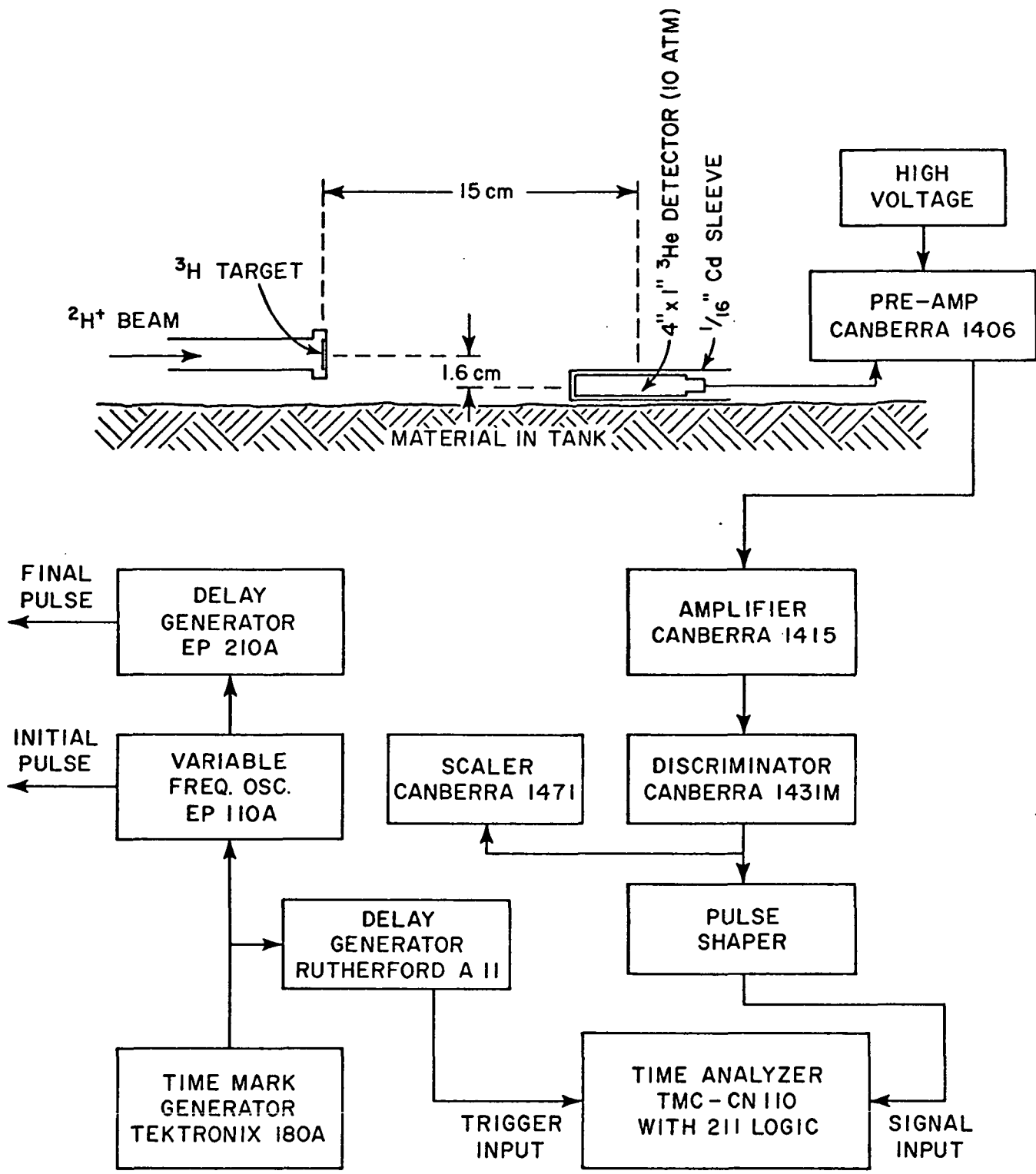


FIGURE 5

BLOCK DIAGRAM OF ELECTRONICS FOR
EPITHERMAL DIE-AWAY MEASUREMENTS

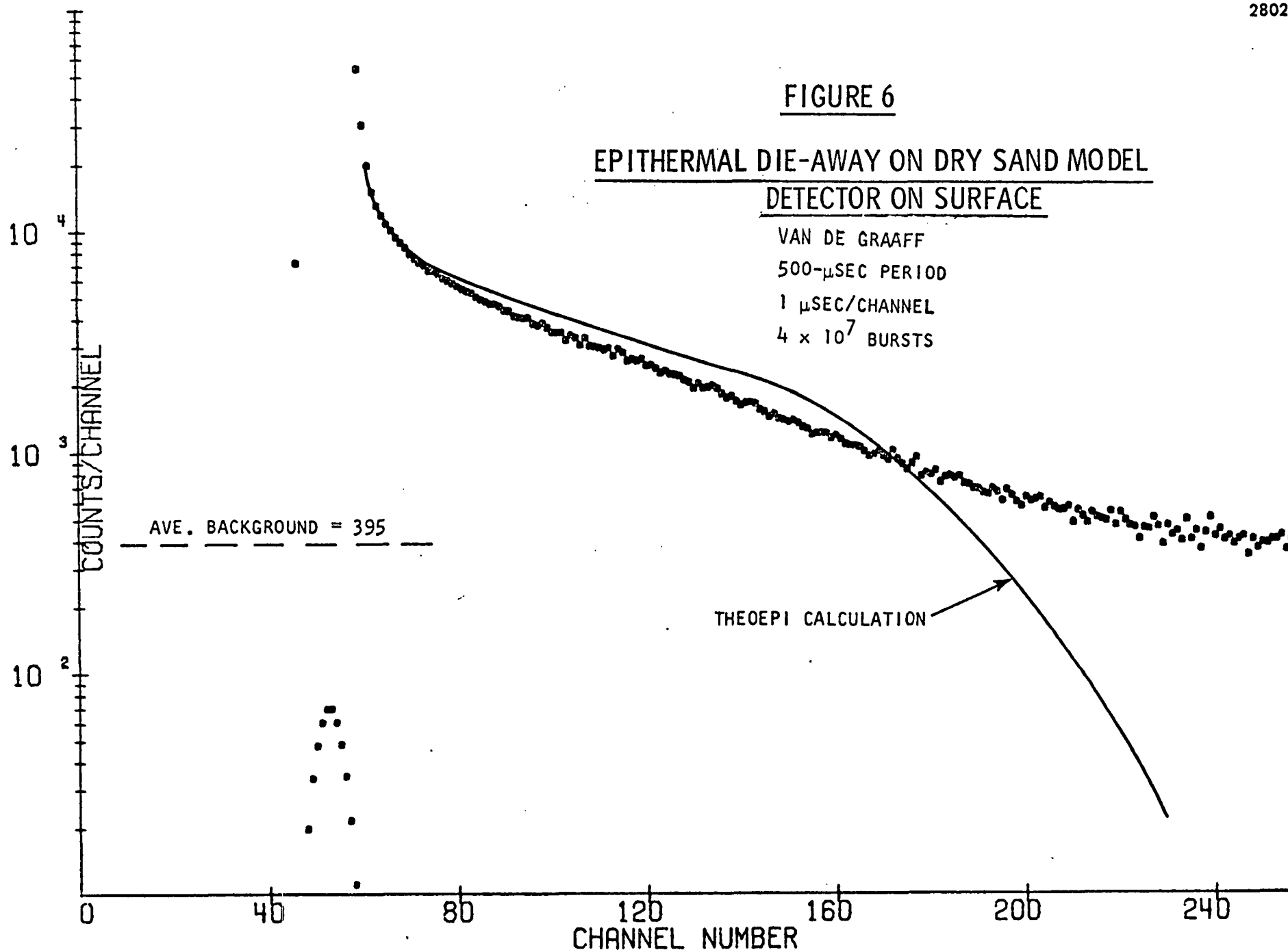
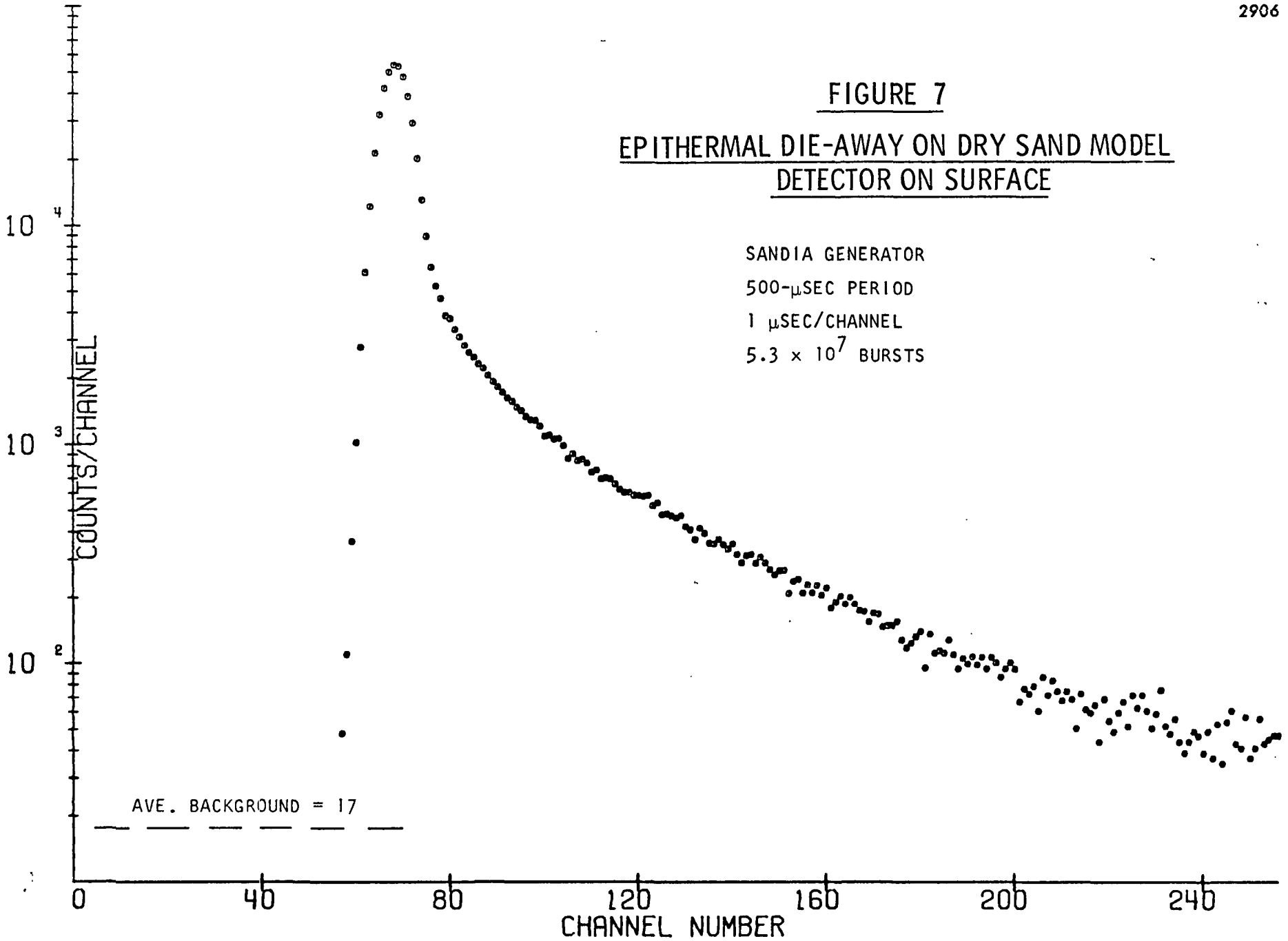


FIGURE 7
EPITHERMAL DIE-AWAY ON DRY SAND MODEL
DETECTOR ON SURFACE

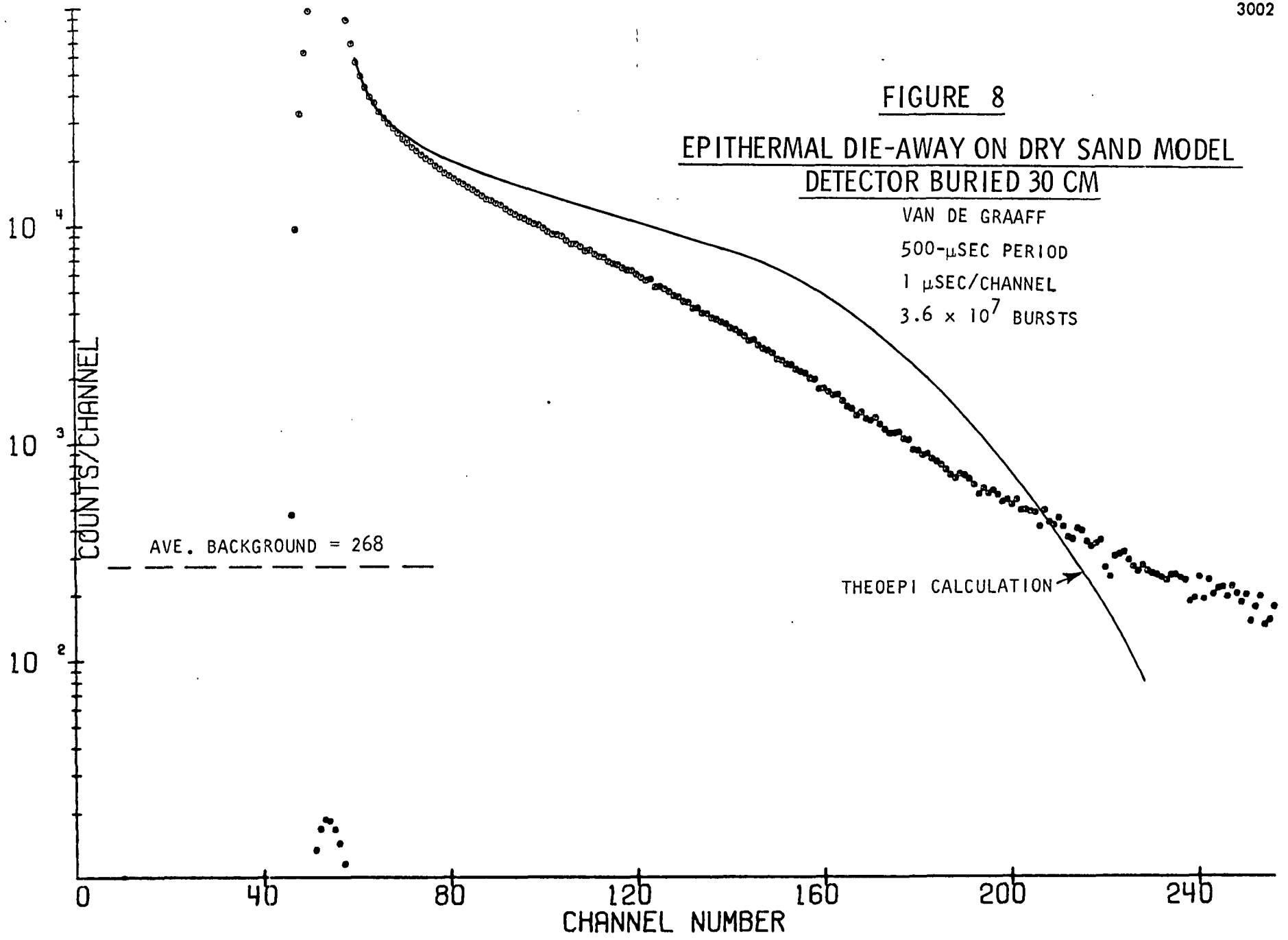
SANDIA GENERATOR
500- μ SEC PERIOD
1 μ SEC/CHANNEL
 5.3×10^7 BURSTS



AVE. BACKGROUND = 17

FIGURE 8
EPITHERMAL DIE-AWAY ON DRY SAND MODEL
DETECTOR BURIED 30 CM

VAN DE GRAAFF
500- μ SEC PERIOD
1 μ SEC/CHANNEL
 3.6×10^7 BURSTS



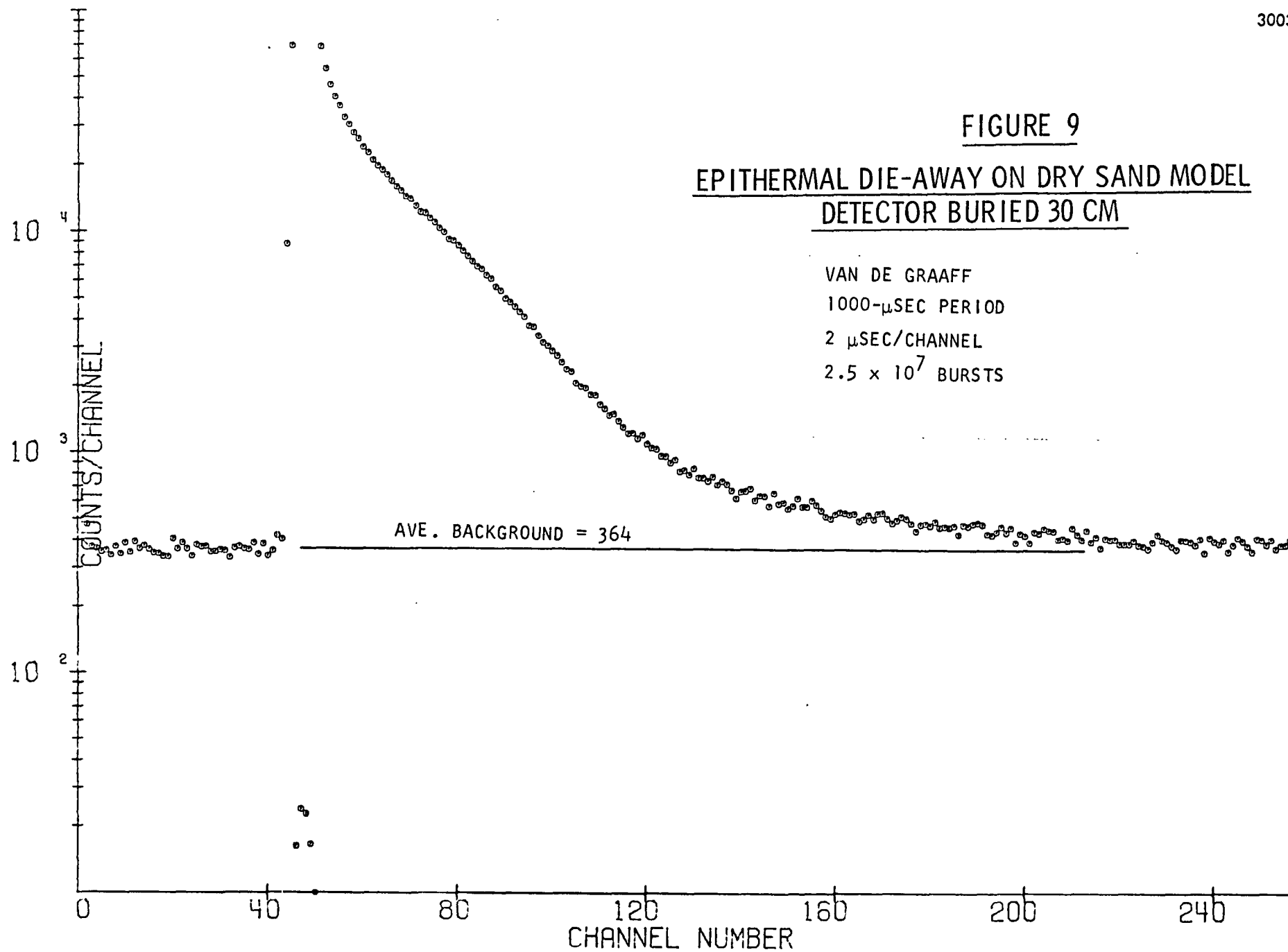


FIGURE 10
EPITHERMAL DIE - AWAY ON DRY SAND MODEL
DETECTOR ON SURFACE

VAN DE GRAAFF
1000- μ SEC PERIOD
2 μ SEC/CHANNEL
2.5 $\times 10^7$ BURSTS

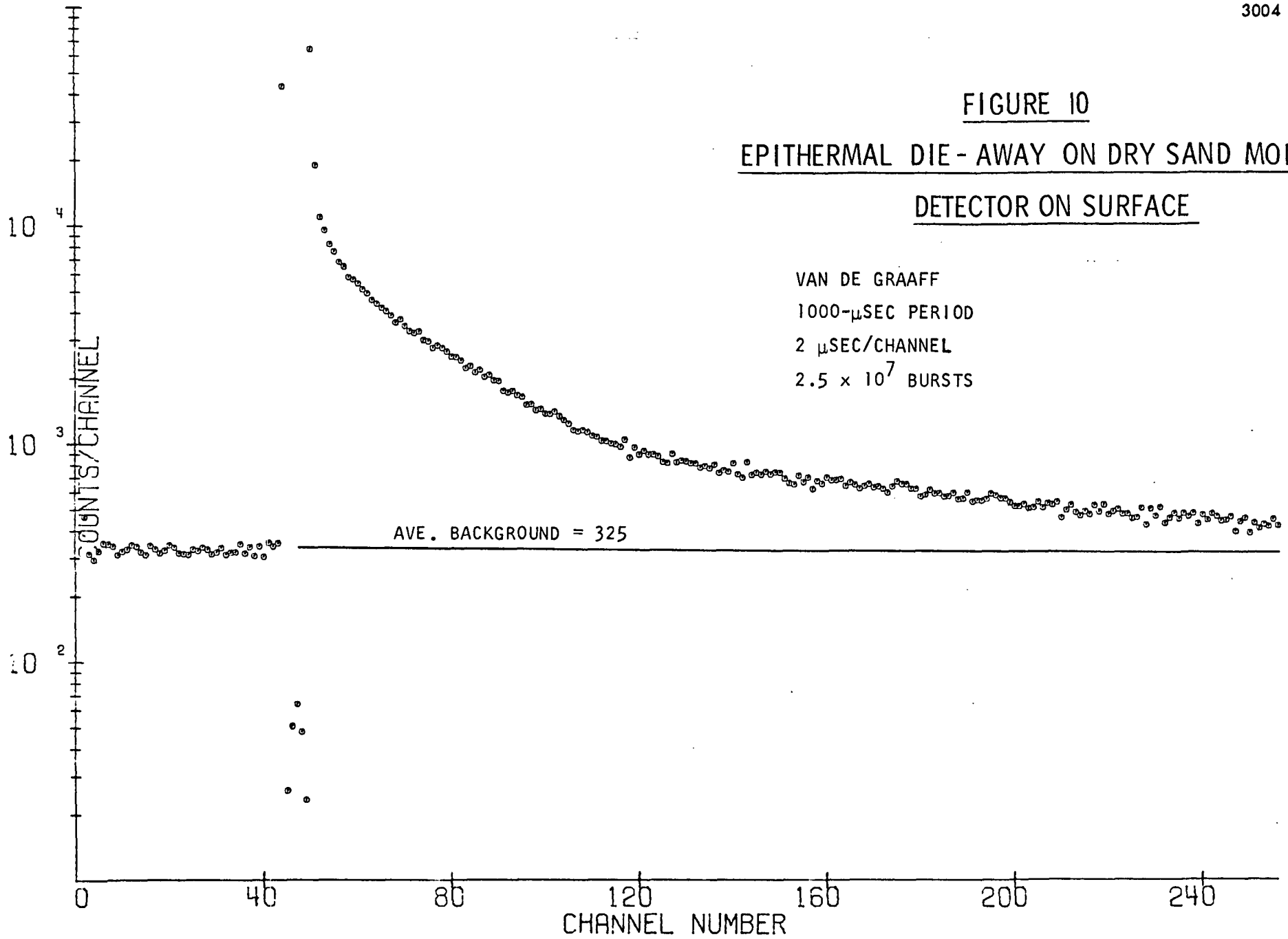


FIGURE 11
EPITHERMAL DIE-AWAY WITH EMPTY TANK
DETECTOR IN SURFACE POSITION

VAN DE GRAAFF
2000- μ SEC PERIOD
4 μ SEC/CHANNEL
1.1 x 10⁷ BURSTS

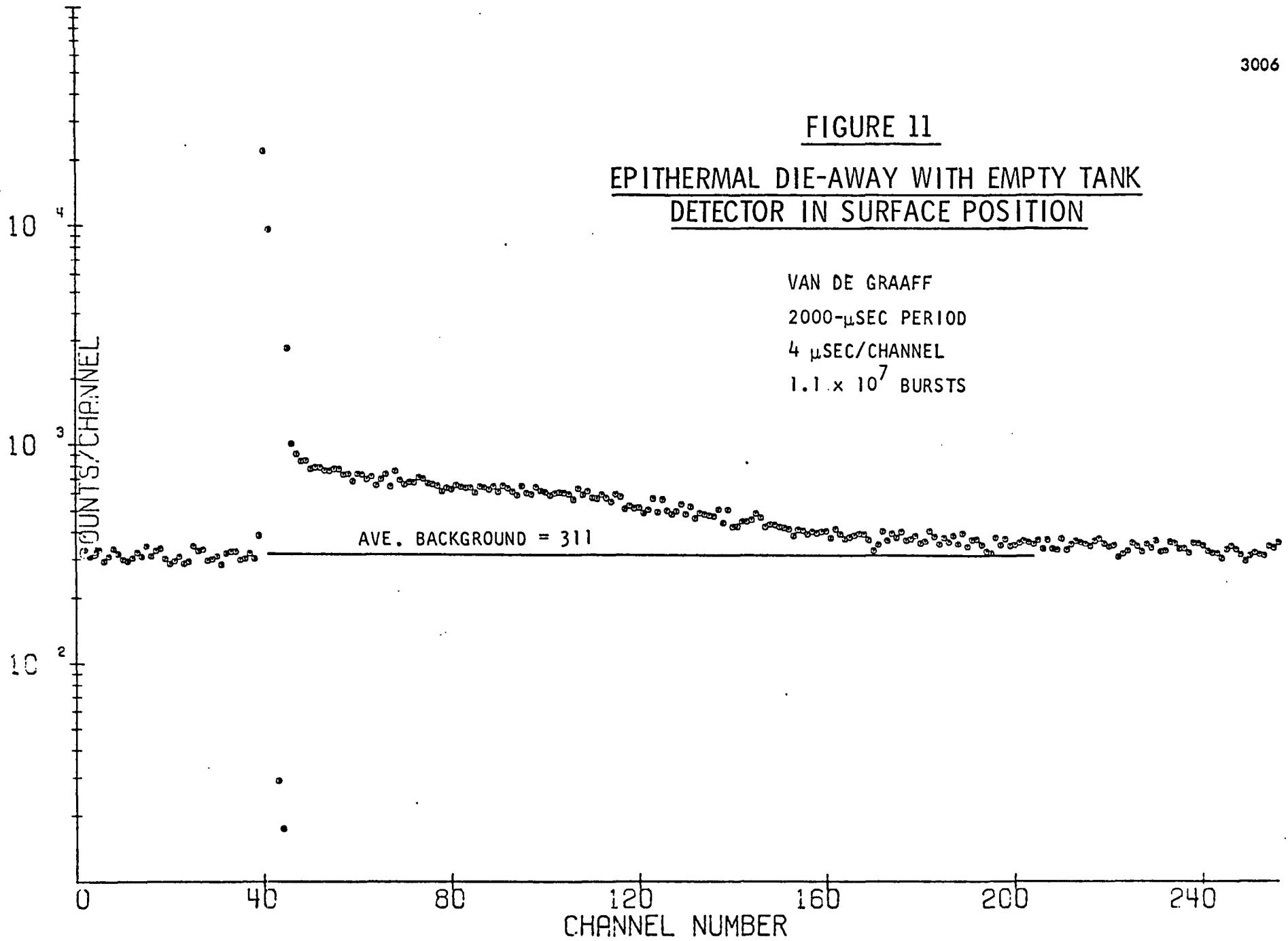
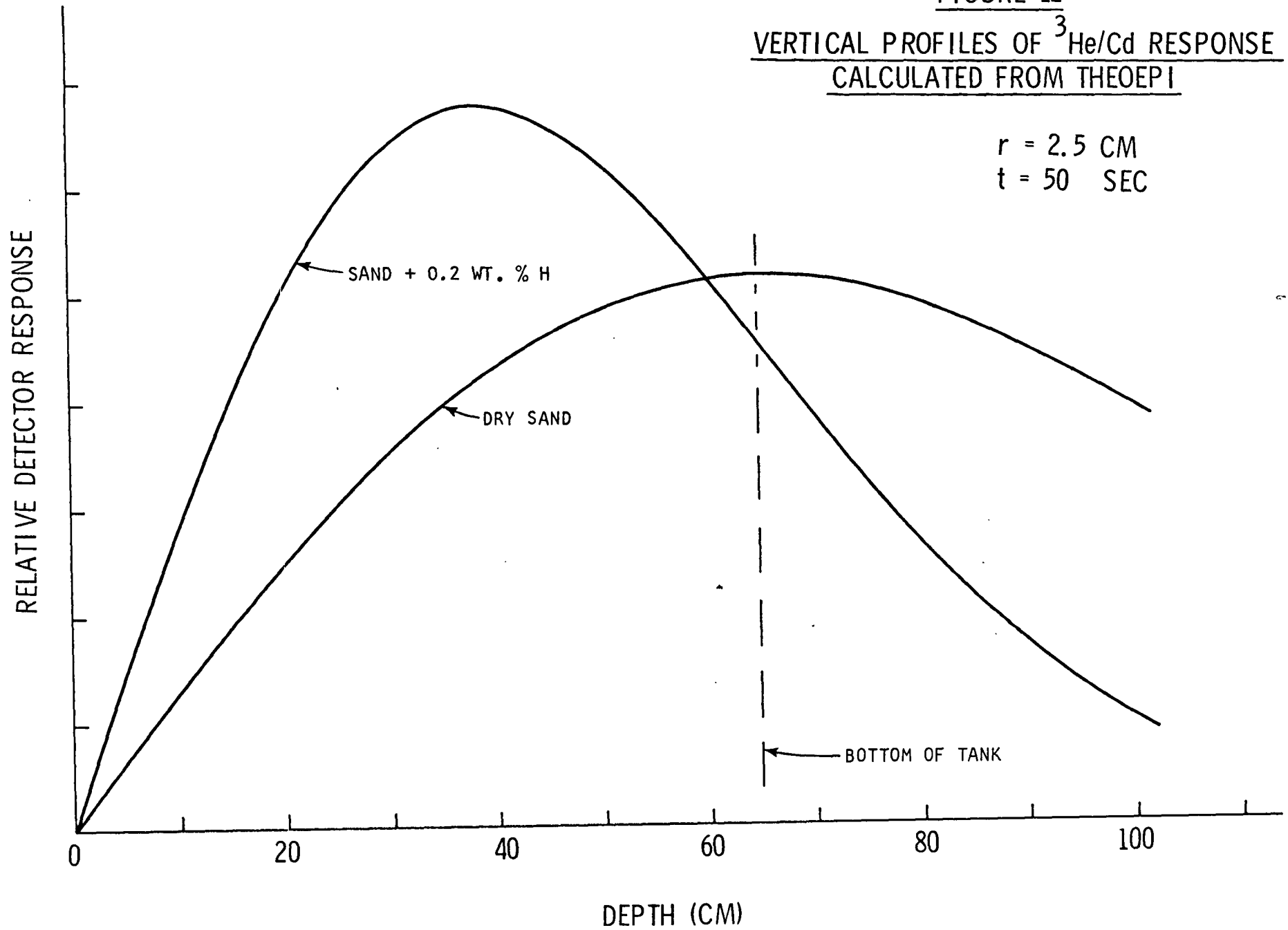
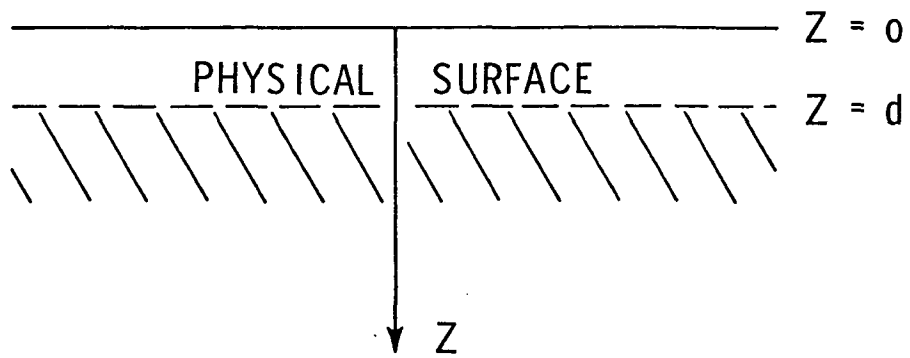


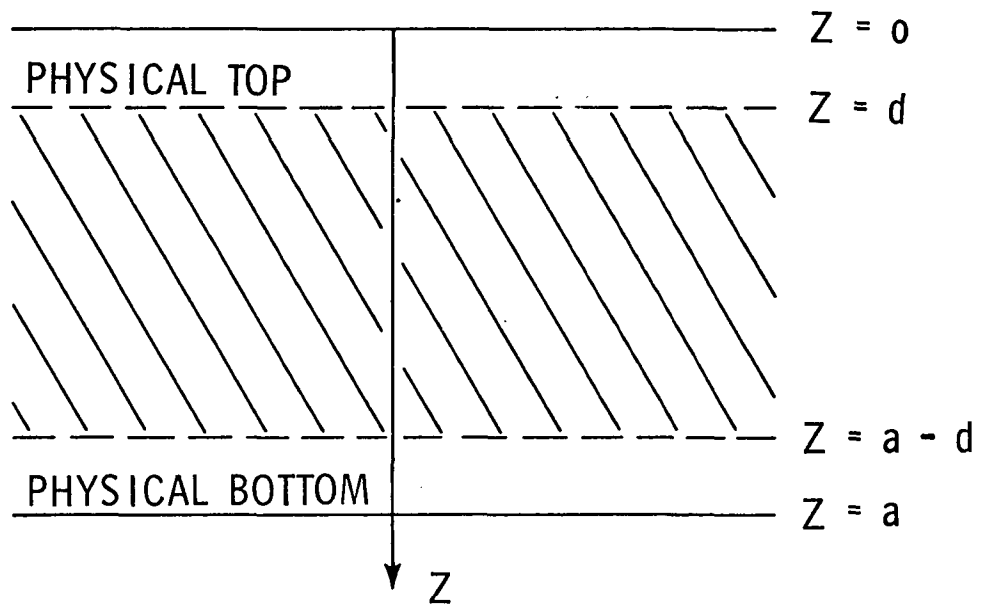
FIGURE 12
VERTICAL PROFILES OF $^3\text{He}/\text{Cd}$ RESPONSE
CALCULATED FROM THEOEPI

$r = 2.5 \text{ CM}$
 $t = 50 \text{ SEC}$





SEMI-INFINITE SLAB



FINITE SLAB

FIGURE 13

GEOMETRICAL CONFIGURATIONS FOR
ONE-DIMENSIONAL CALCULATIONS

FIGURE 14

$^3\text{He}/\text{Cd}$ EFFICIENCY CURVES

— $\epsilon = e^{-0.00736\sigma_{\text{Cd}}} (1 - e^{-\frac{1.43}{v}})$

--- $\epsilon = \begin{cases} 0, & v < 1 \\ \frac{1.43}{v} (1 - \frac{0.715}{v}), & v \geq 1 \end{cases}$

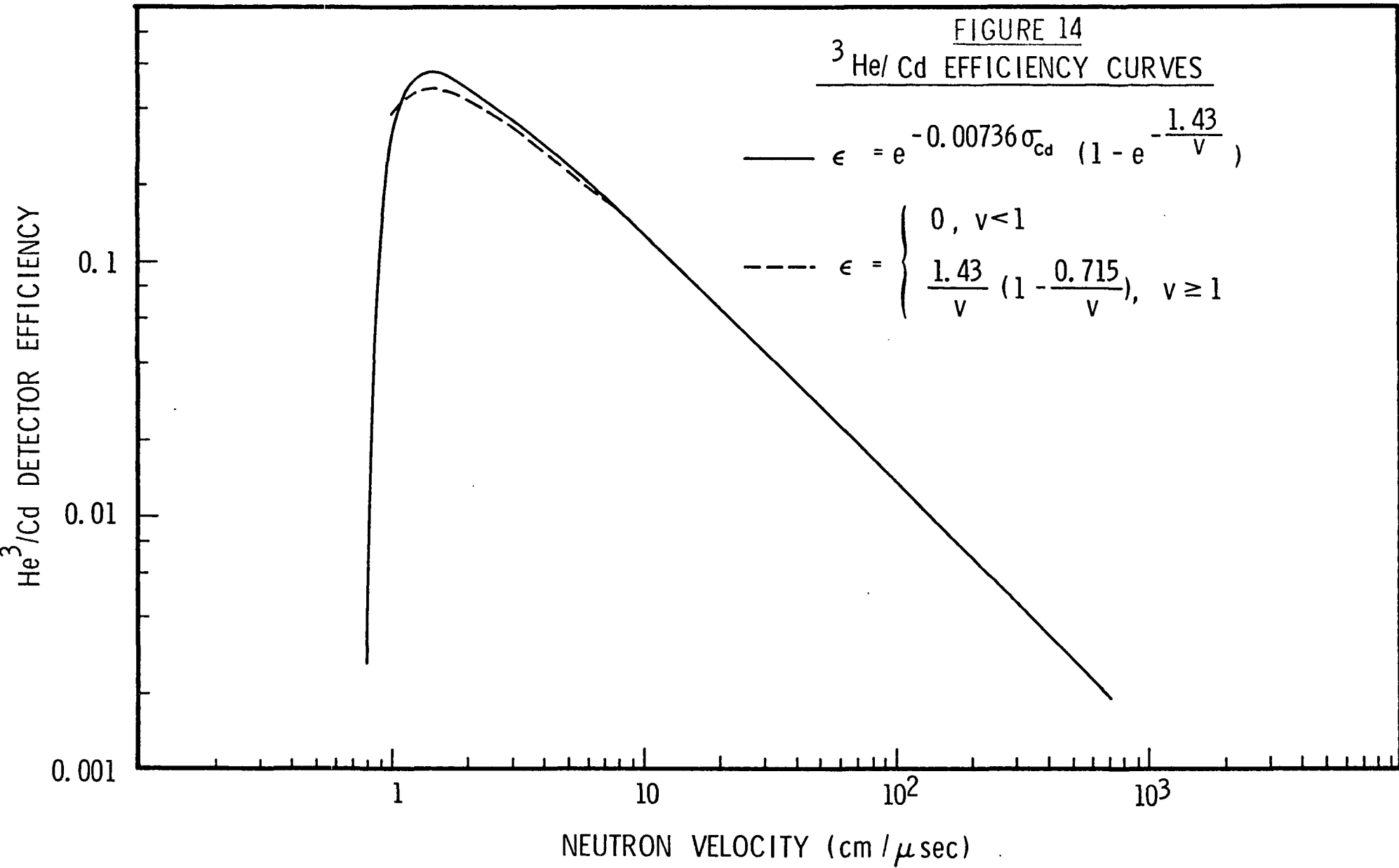


FIGURE 15
COMPARISON OF EXPERIMENTAL
EPITHERMAL DIE-AWAY AND THEORETICAL
CALCULATIONS

DRY SAND
DETECTOR ON SURFACE

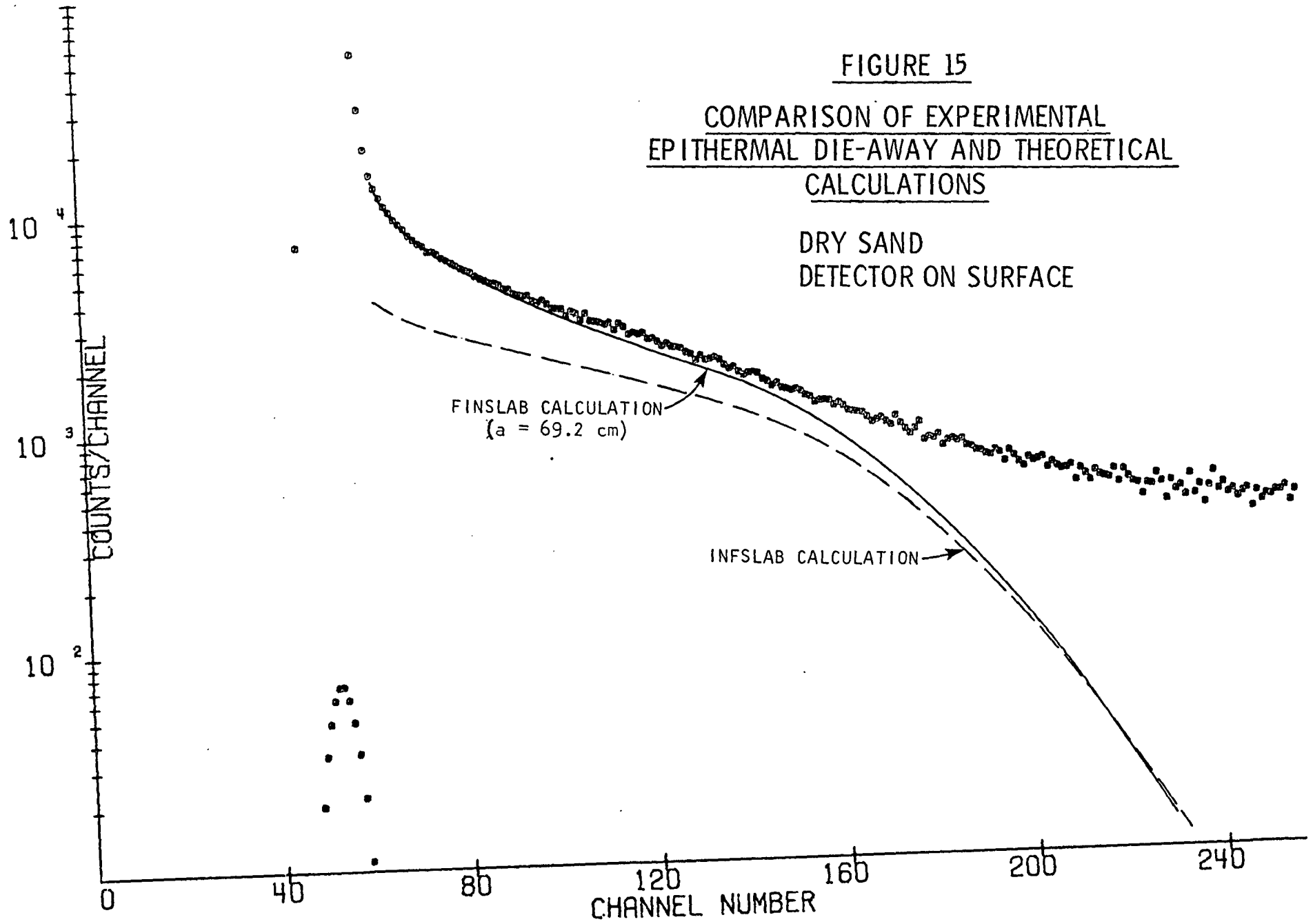


FIGURE 16

COMPARISON OF THEORETICALLY
CALCULATED DIE-AWAY CURVES WITH
PROGRAMS INFSLAB AND FINSLAB

DETECTOR ON SURFACE ($Z = d$)
FOR FINSLAB, $a = 60 + 2d$ cm

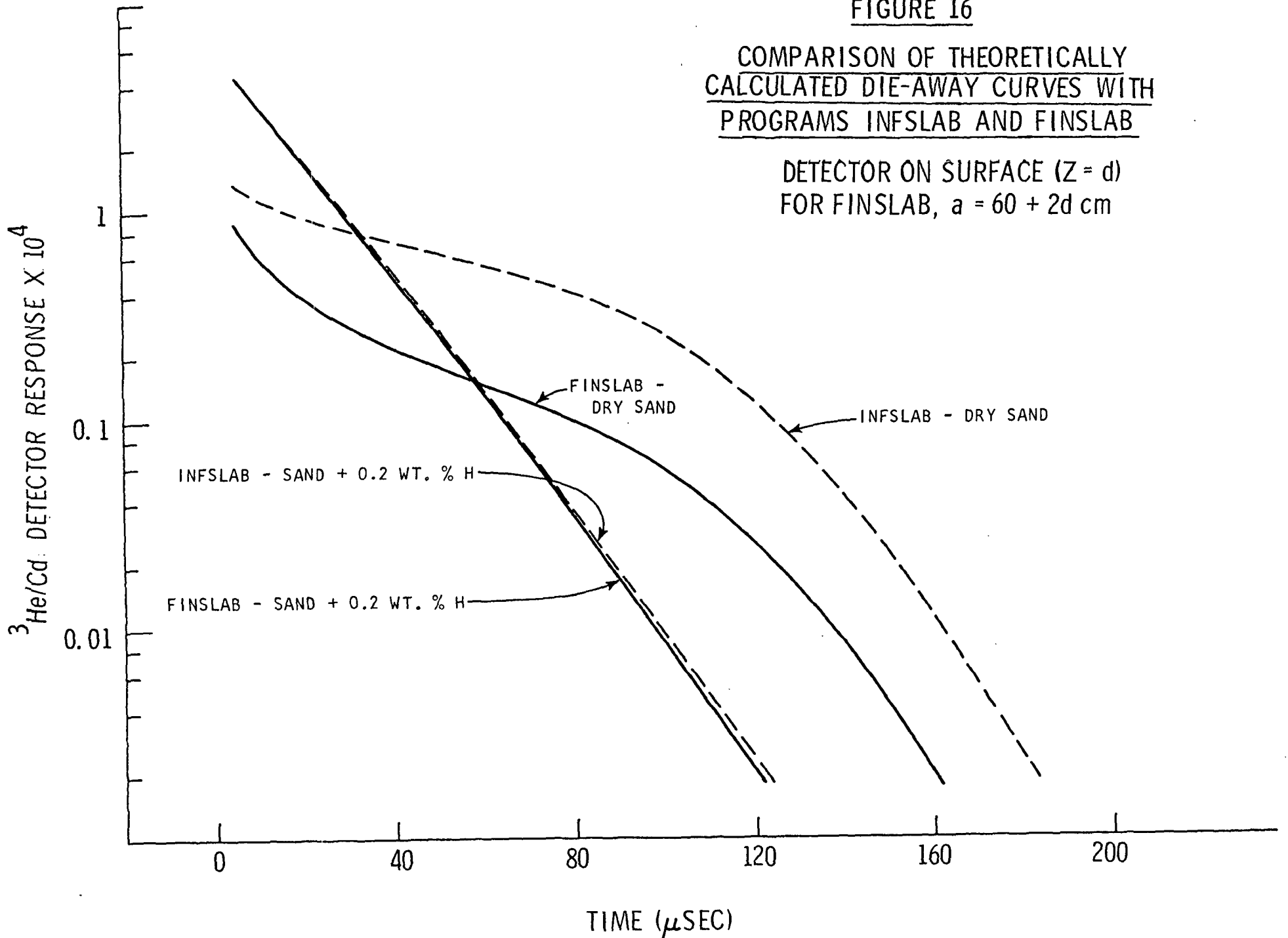


FIGURE 17
COMPARISON OF EXPERIMENTAL
EPITHERMAL DIE-AWAY AND THEORETICAL
CALCULATIONS

DRY SAND
BURIED DETECTOR (Z = 35 cm)

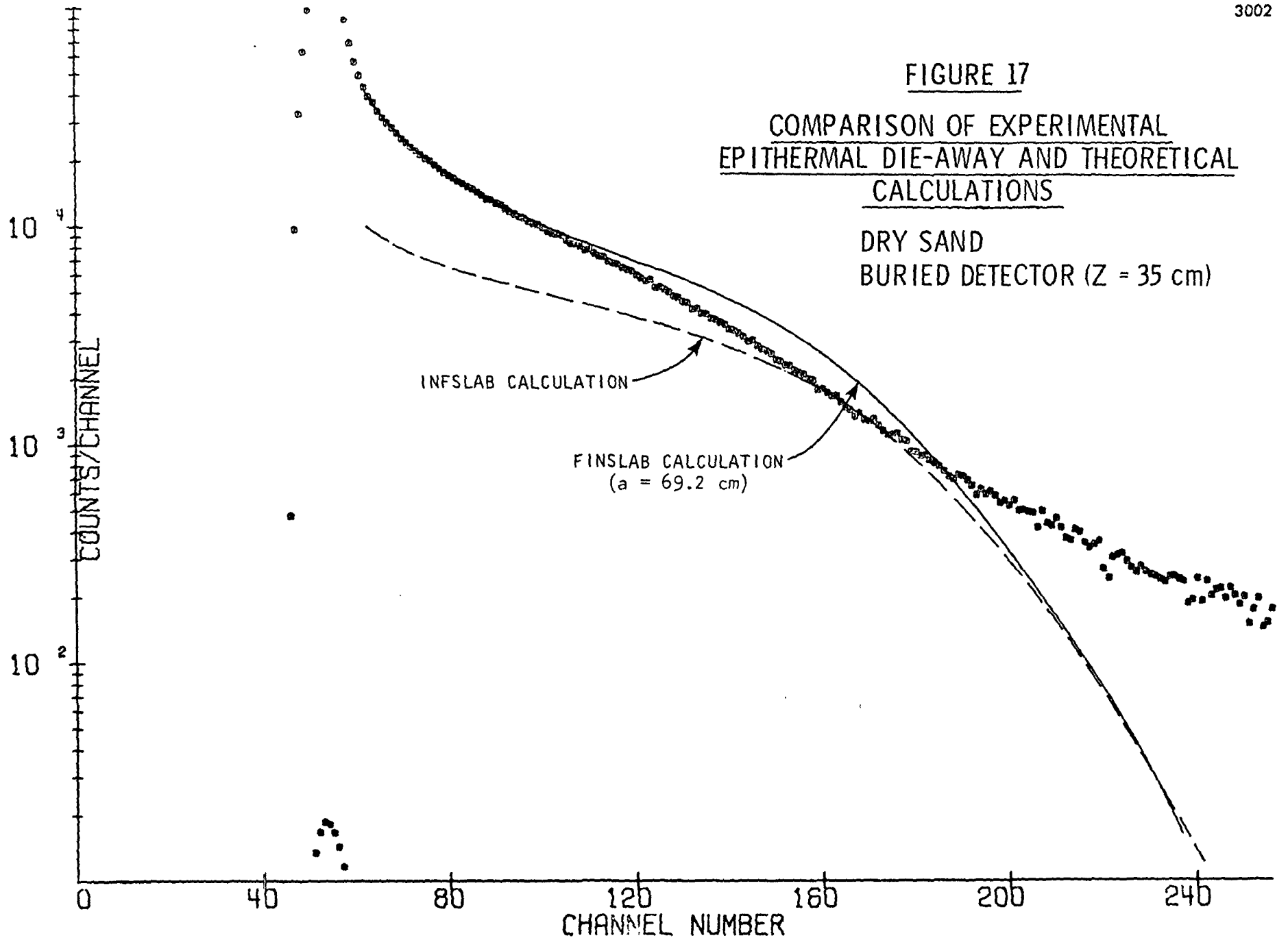


FIGURE 18
VERTICAL PROFILES OF $^3\text{He}/\text{Cd}$ DETECTOR
RESPONSE FOR DRY SAND

$t = 60 \mu\text{SEC}$

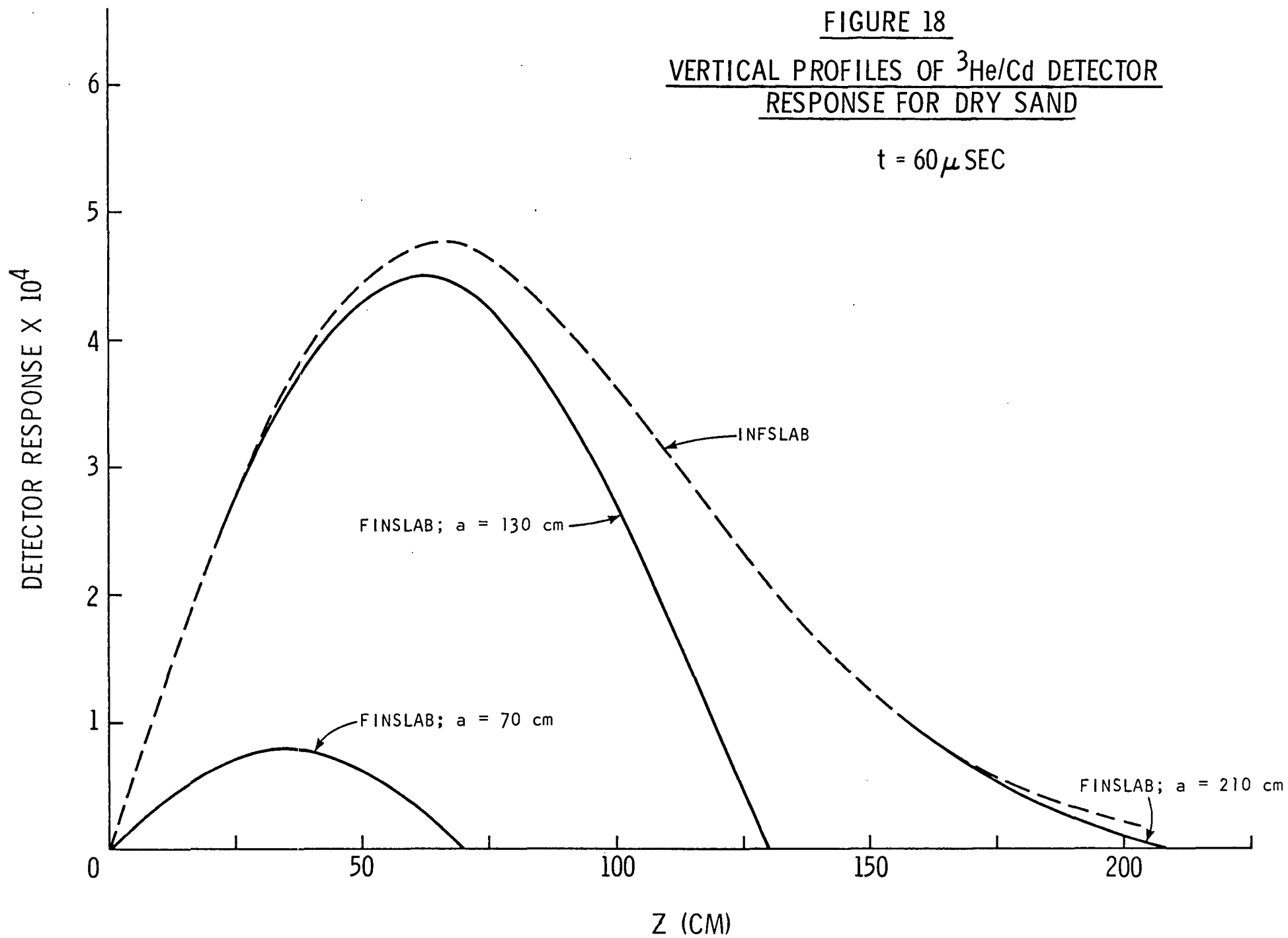


FIGURE 19
VERTICAL PROFILES OF $^3\text{He}/\text{Cd}$ DETECTOR
RESPONSE FOR SAND + 0.2 WT. % H
 $t = 60 \mu\text{SEC}$

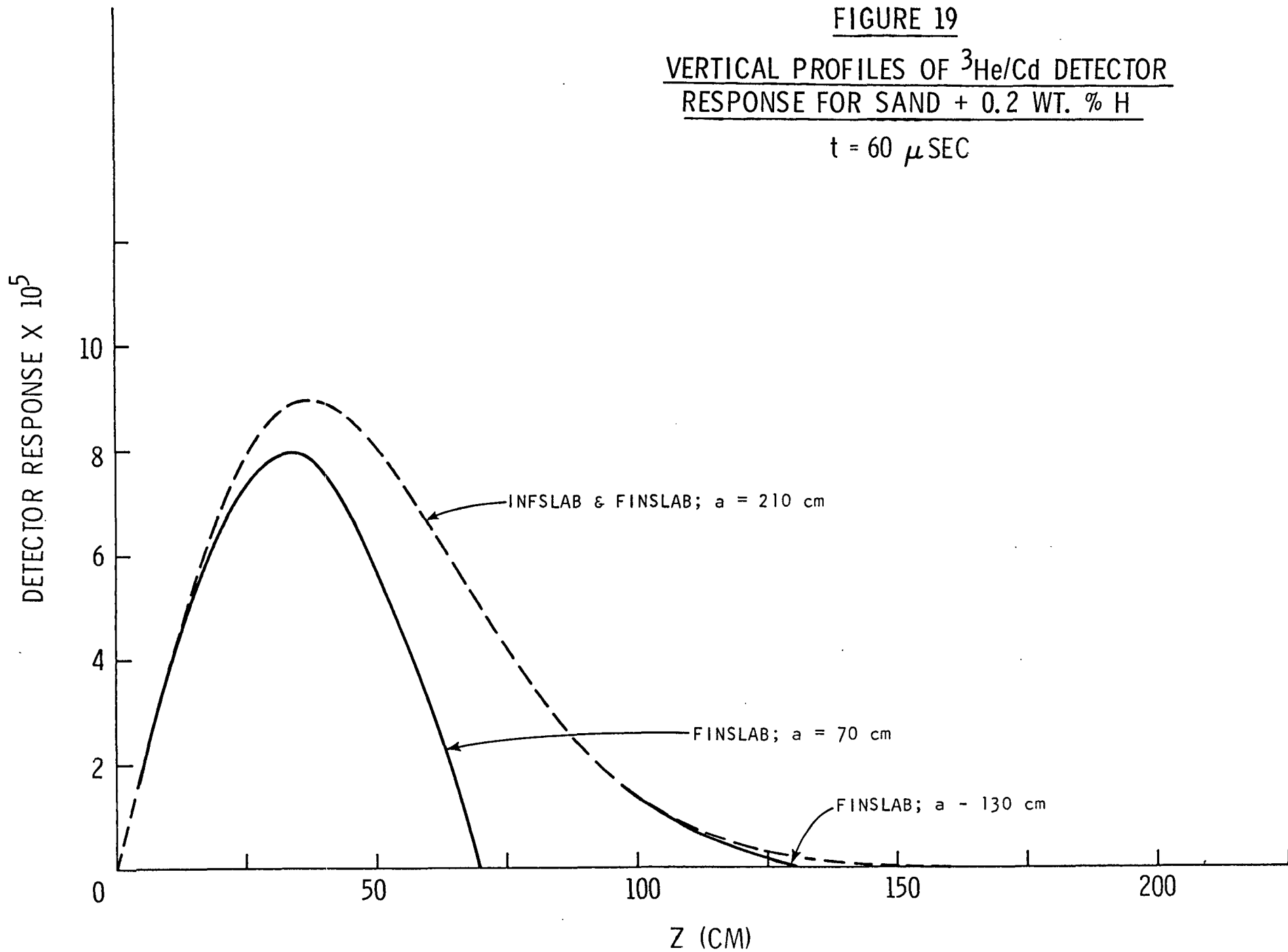


FIGURE 20

NEUTRON VELOCITY PROFILES FROM
INFSLAB

— DRY SAND; -- SAND + 0.2 WT. % H

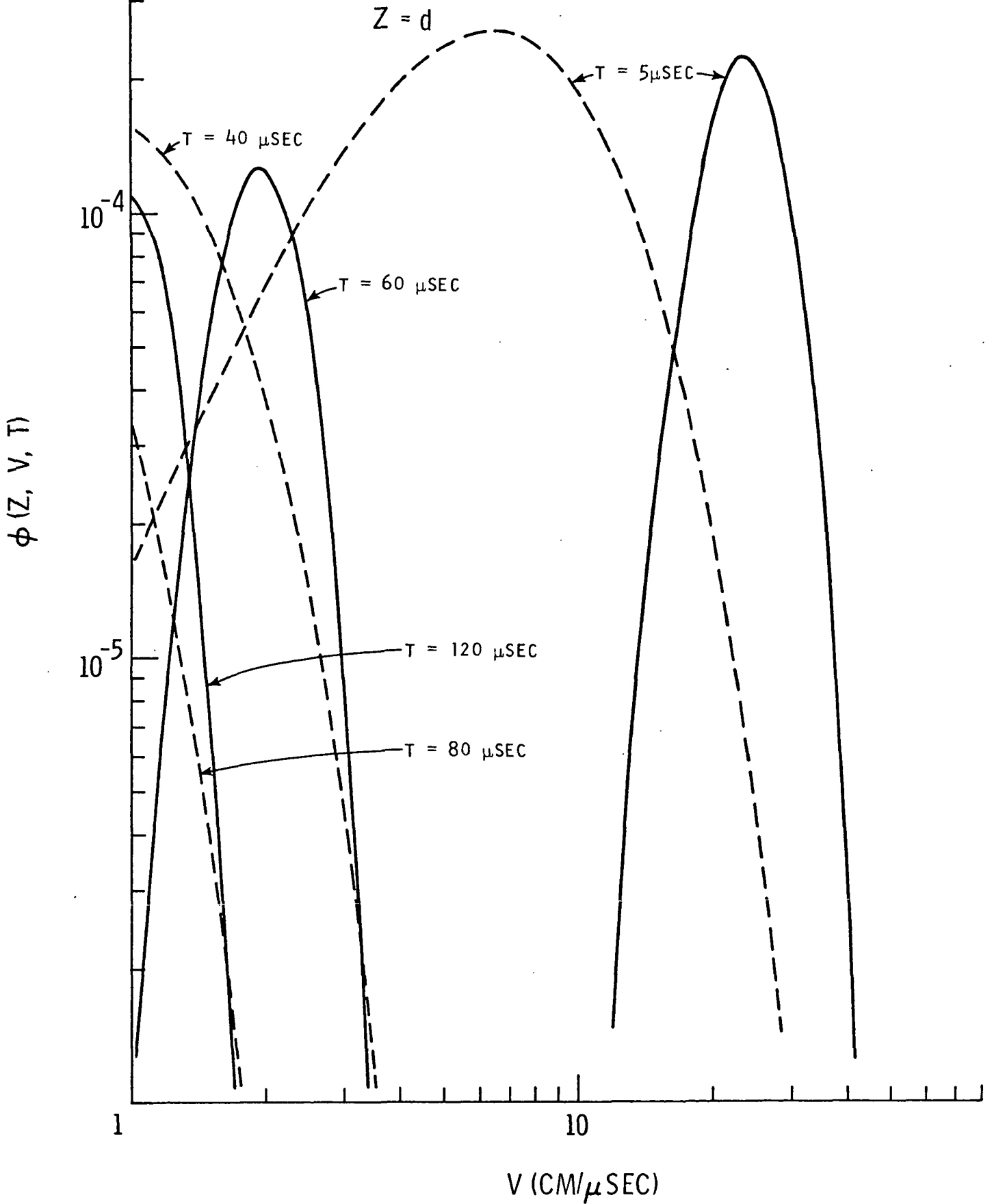


FIGURE 21
THERMAL DIE-AWAY OF PURE WATER IN
SMALL RESERVOIR

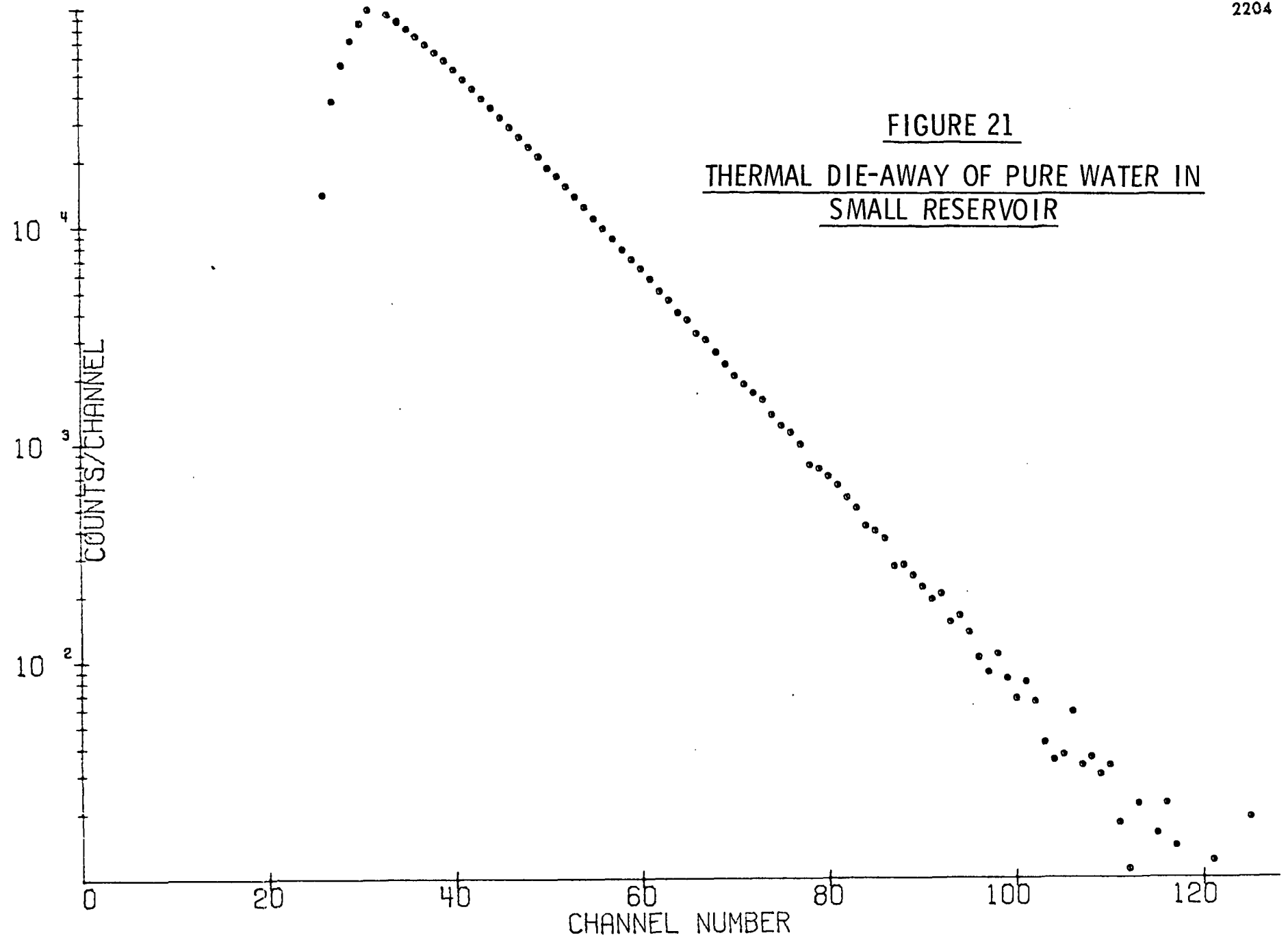


FIGURE 22
THERMAL DIE-AWAY OF CRUSHED DUNITE
SATURATED WITH PURE WATER IN SMALL
RESERVOIR

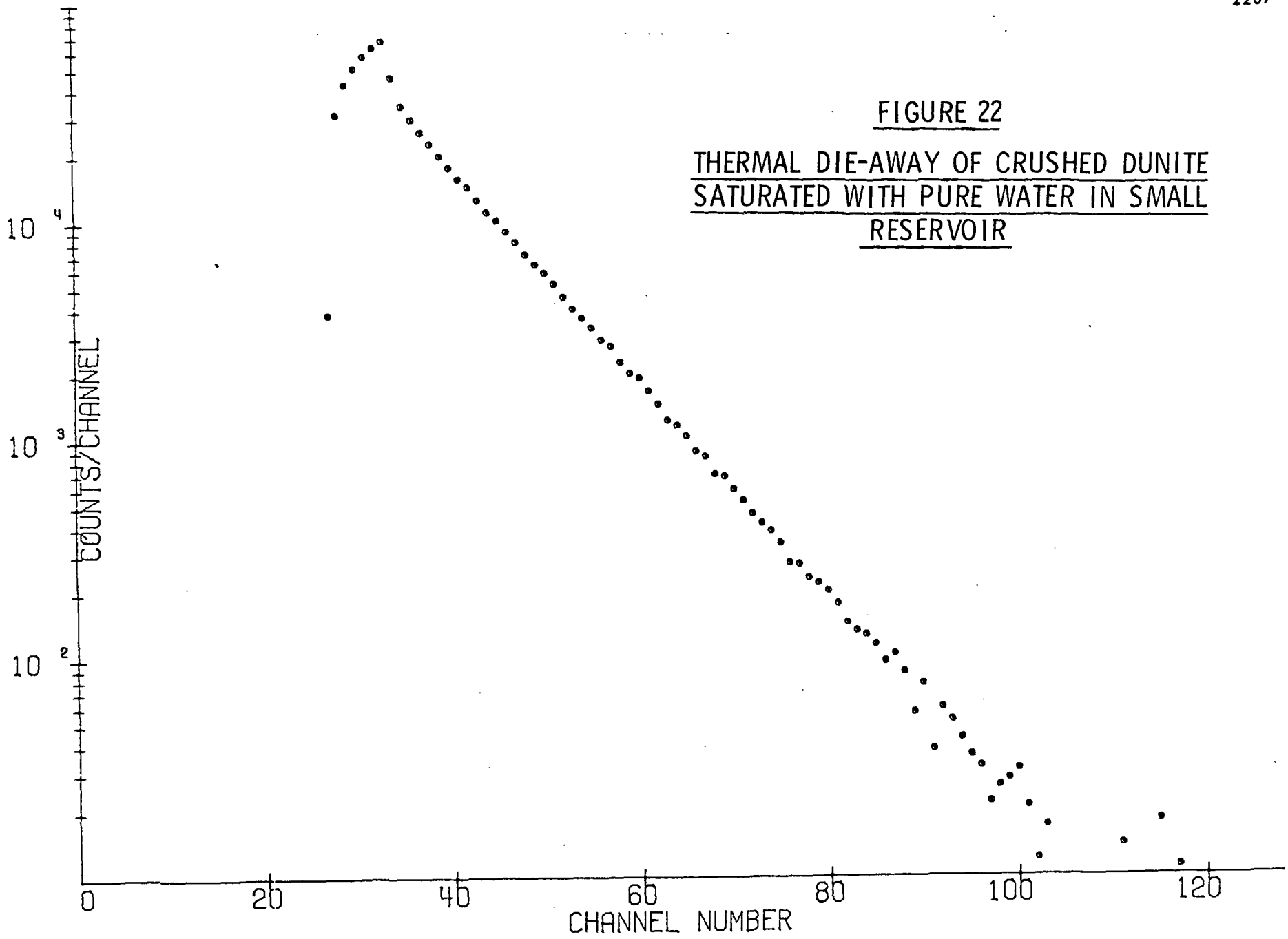


FIGURE 23
THERMAL DIE-AWAY OF CRUSHED BURNET
RED GRANITE SATURATED WITH PURE
WATER IN SMALL RESERVOIR

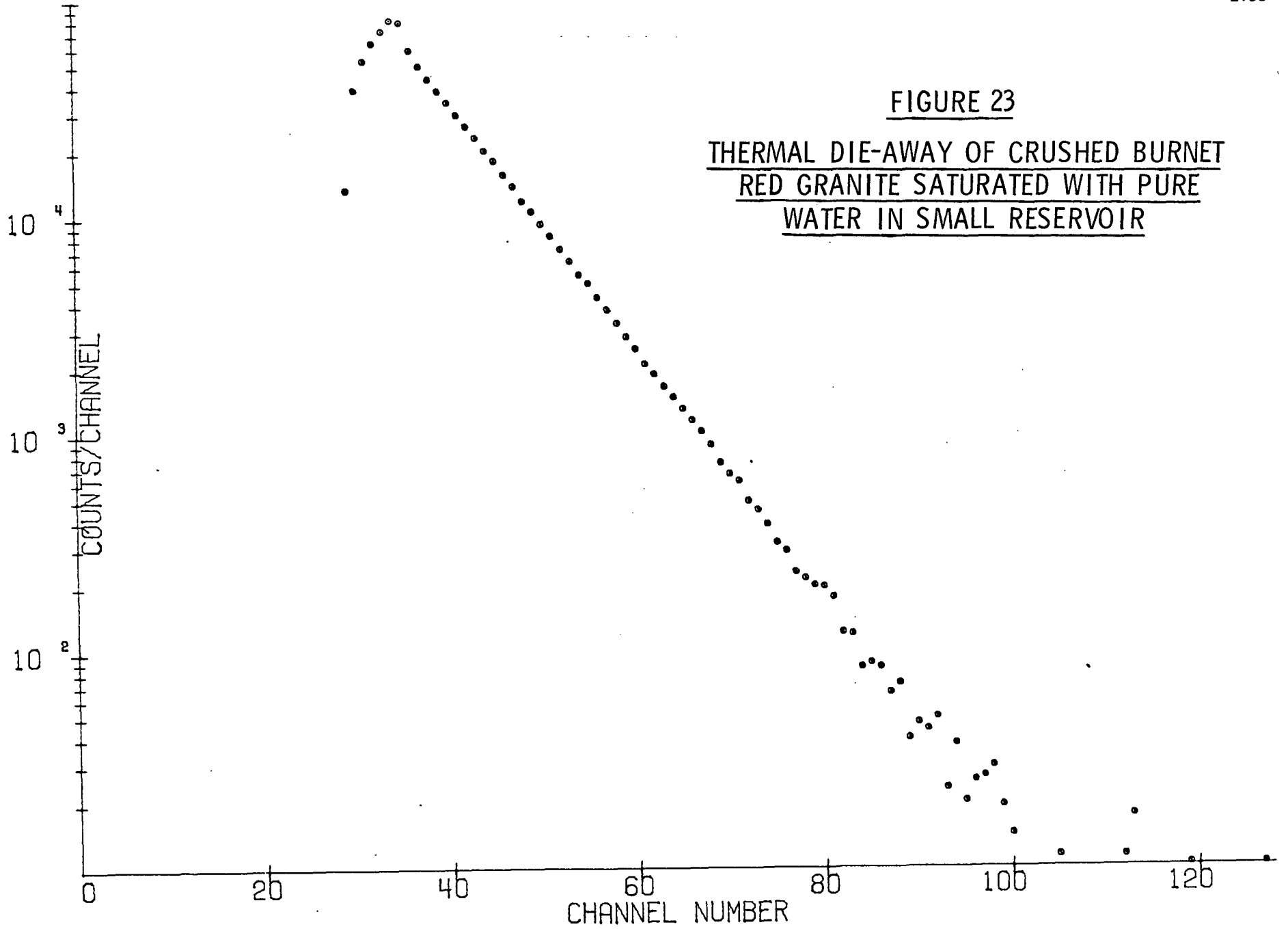
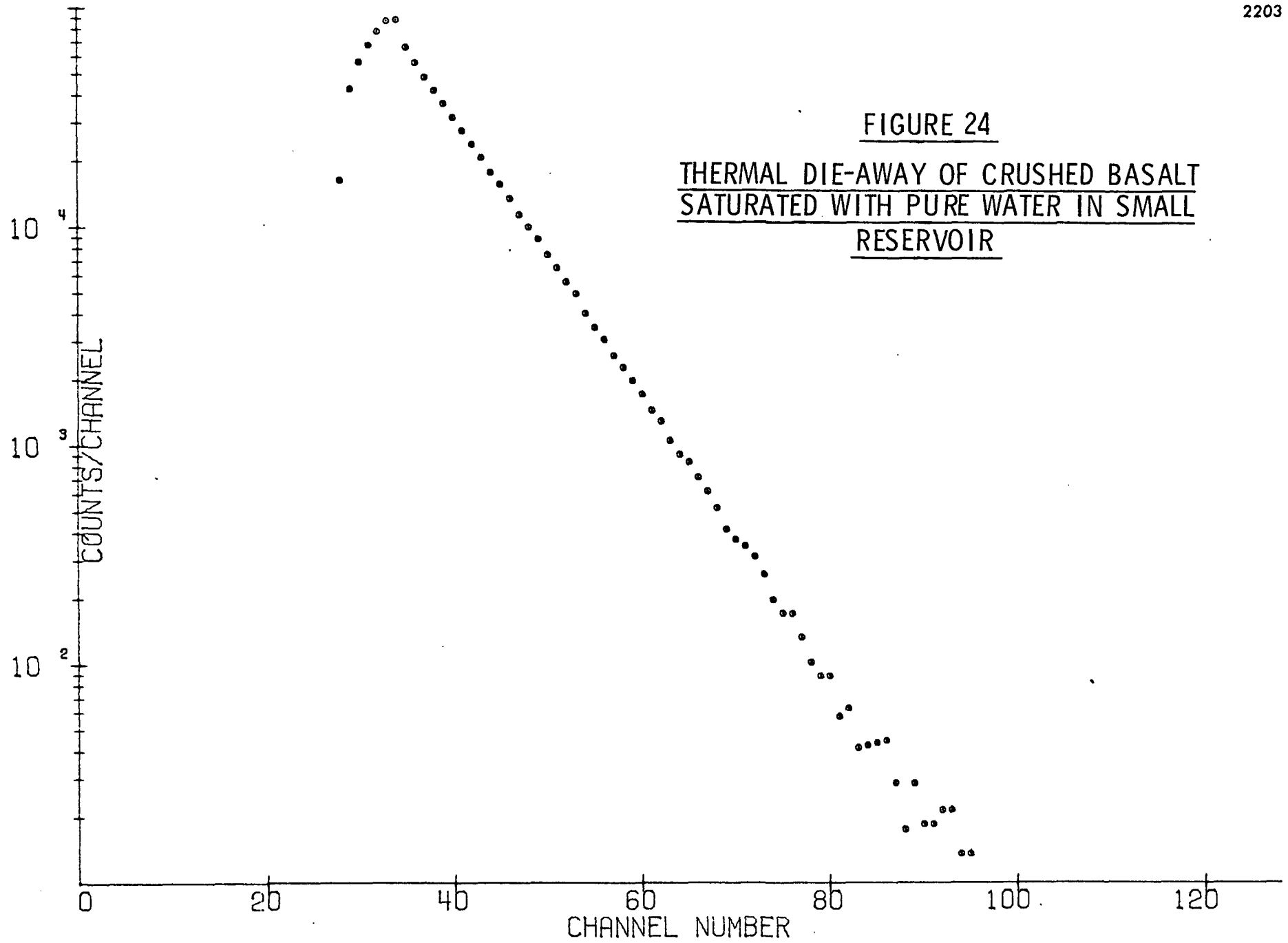


FIGURE 24
THERMAL DIE-AWAY OF CRUSHED BASALT
SATURATED WITH PURE WATER IN SMALL
RESERVOIR



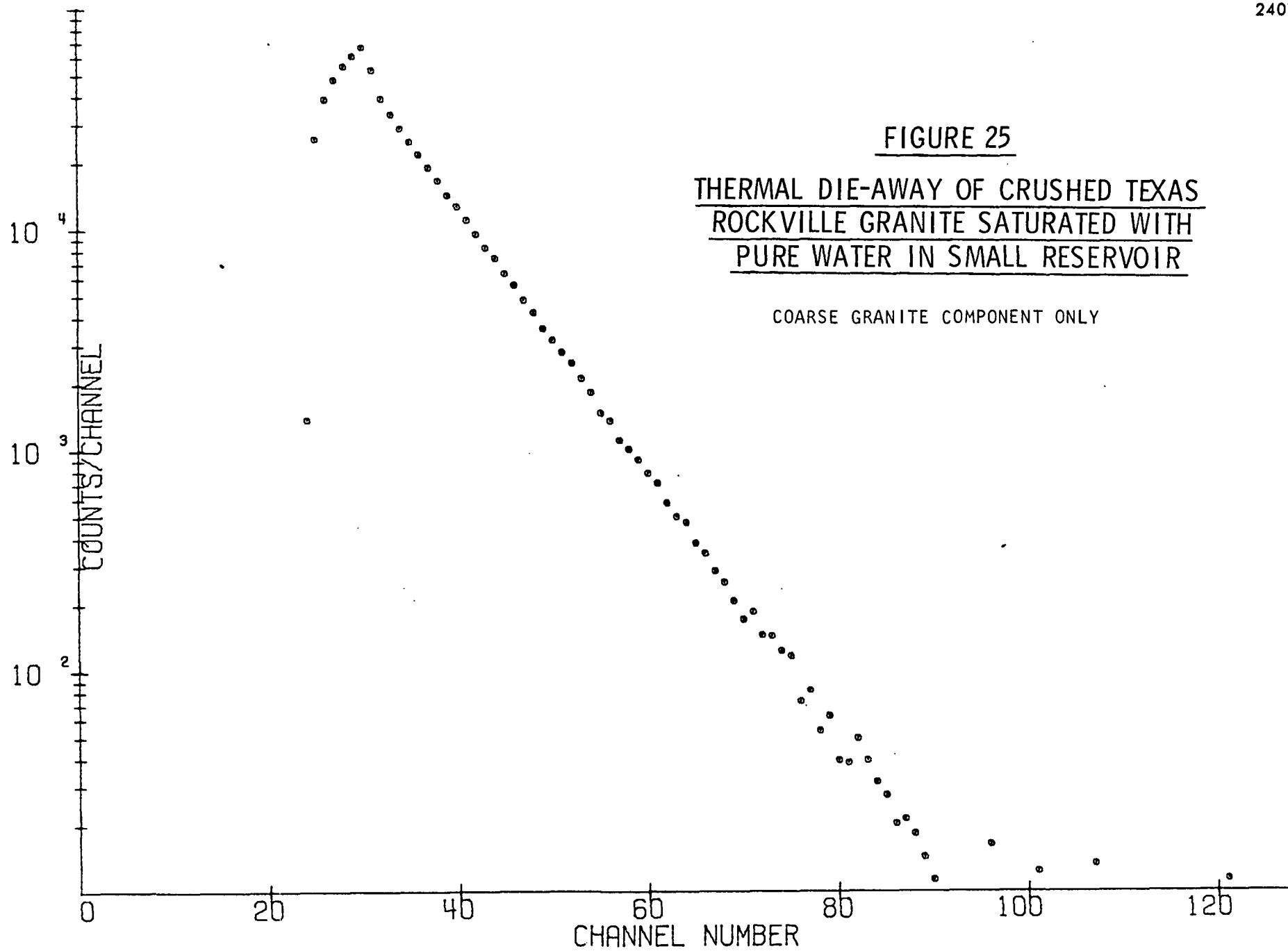


FIGURE 26

PROBE CONFIGURATION FOR
THERMAL DIE-AWAY EXPERIMENTS

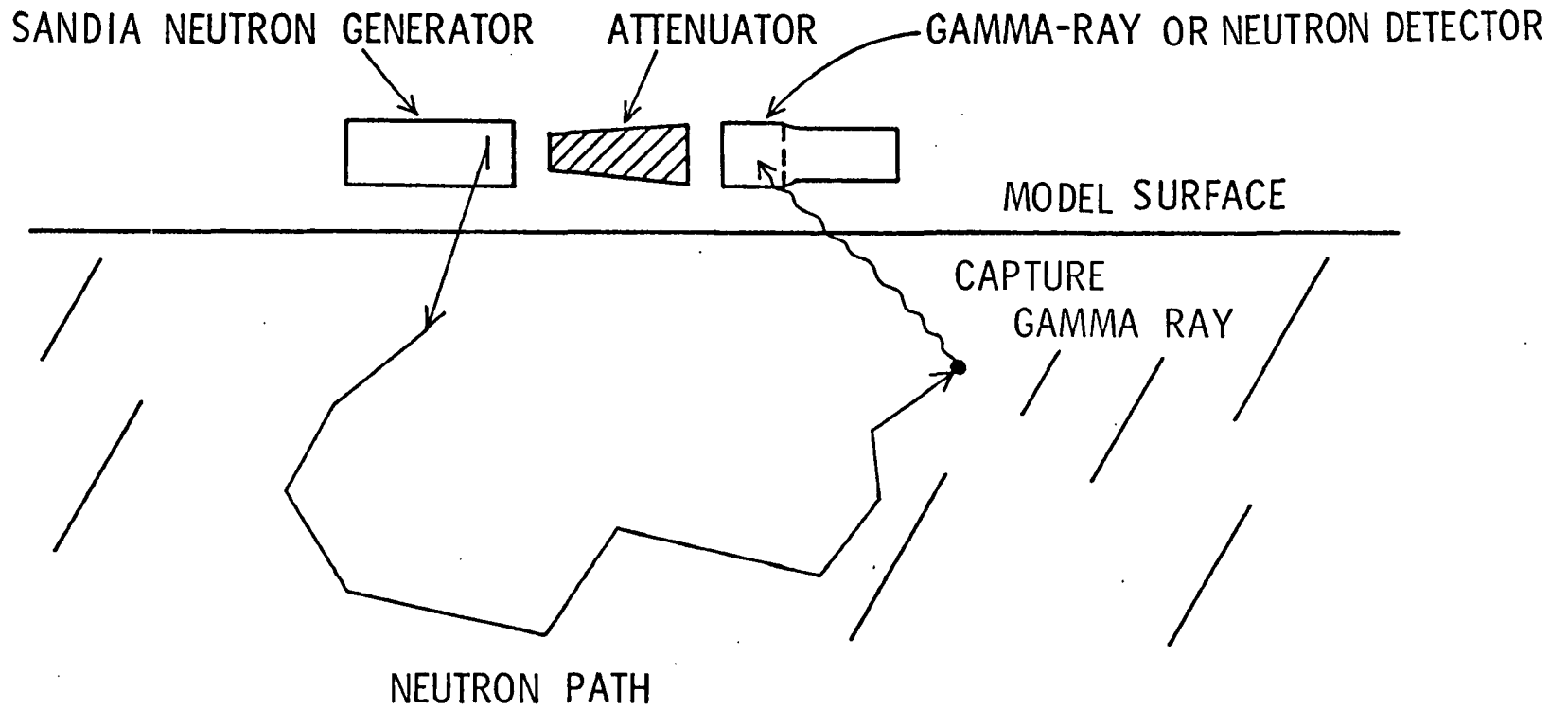


FIGURE 27

THERMAL NEUTRON DIE-AWAY DATA ON
KNIPPA BASALT MODEL

- - PROBE UNSHIELDED
- - PROBE SHIELDED WITH CADMIUM

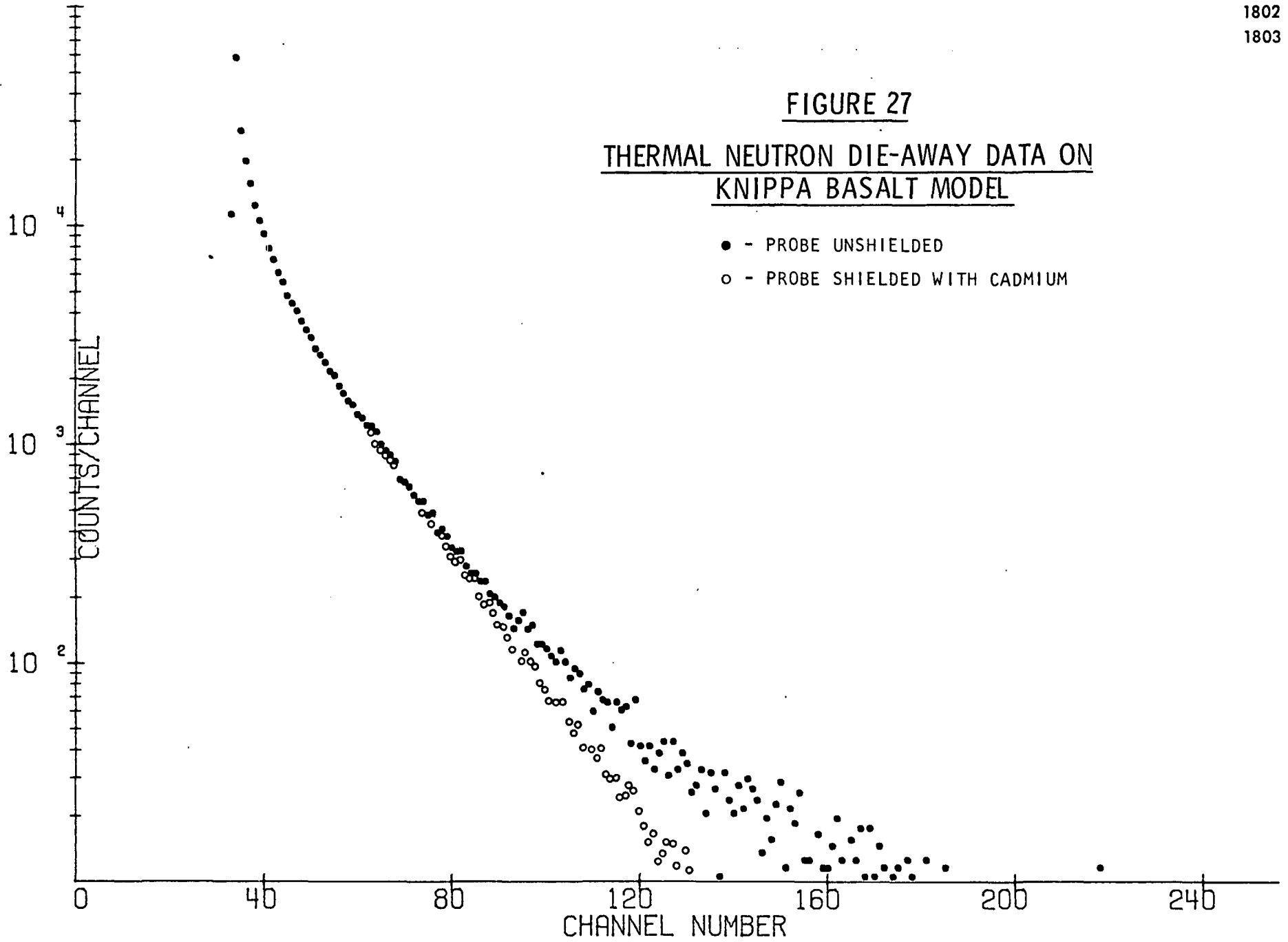


FIGURE 28

THERMAL NEUTRON DIE-AWAY DATA FOR
FOR ALL FOUR LARGE ROCK MODELS

2012
1807
1803
2010

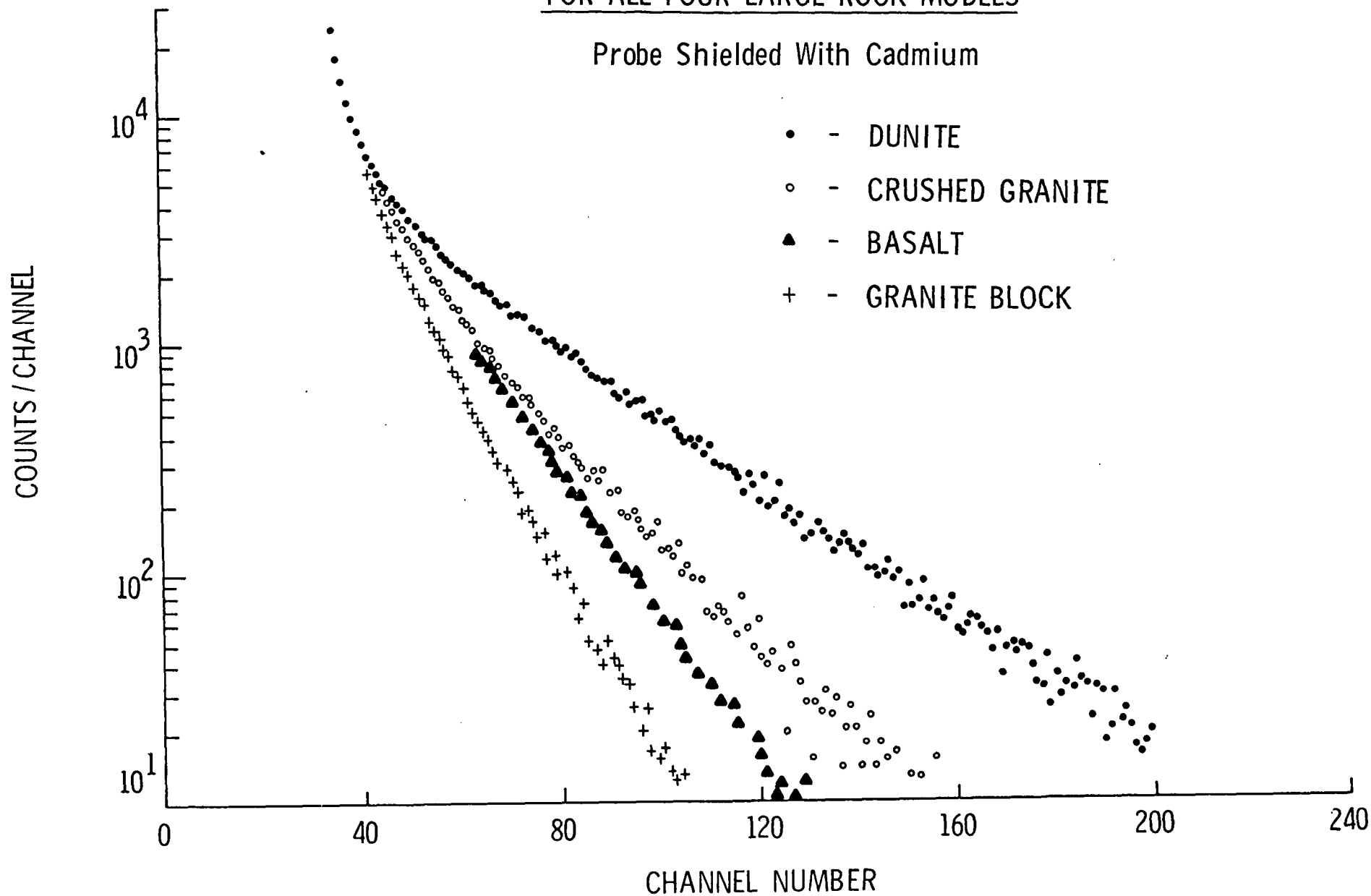


FIGURE 29
THERMAL NEUTRON DIE-AWAY DATA FOR
DUNITE MODEL FITTED OVER CHANNELS
50 - 140

$$\ln \phi(t) = \theta_1 - \theta_2 t + \theta_3 / t^2$$

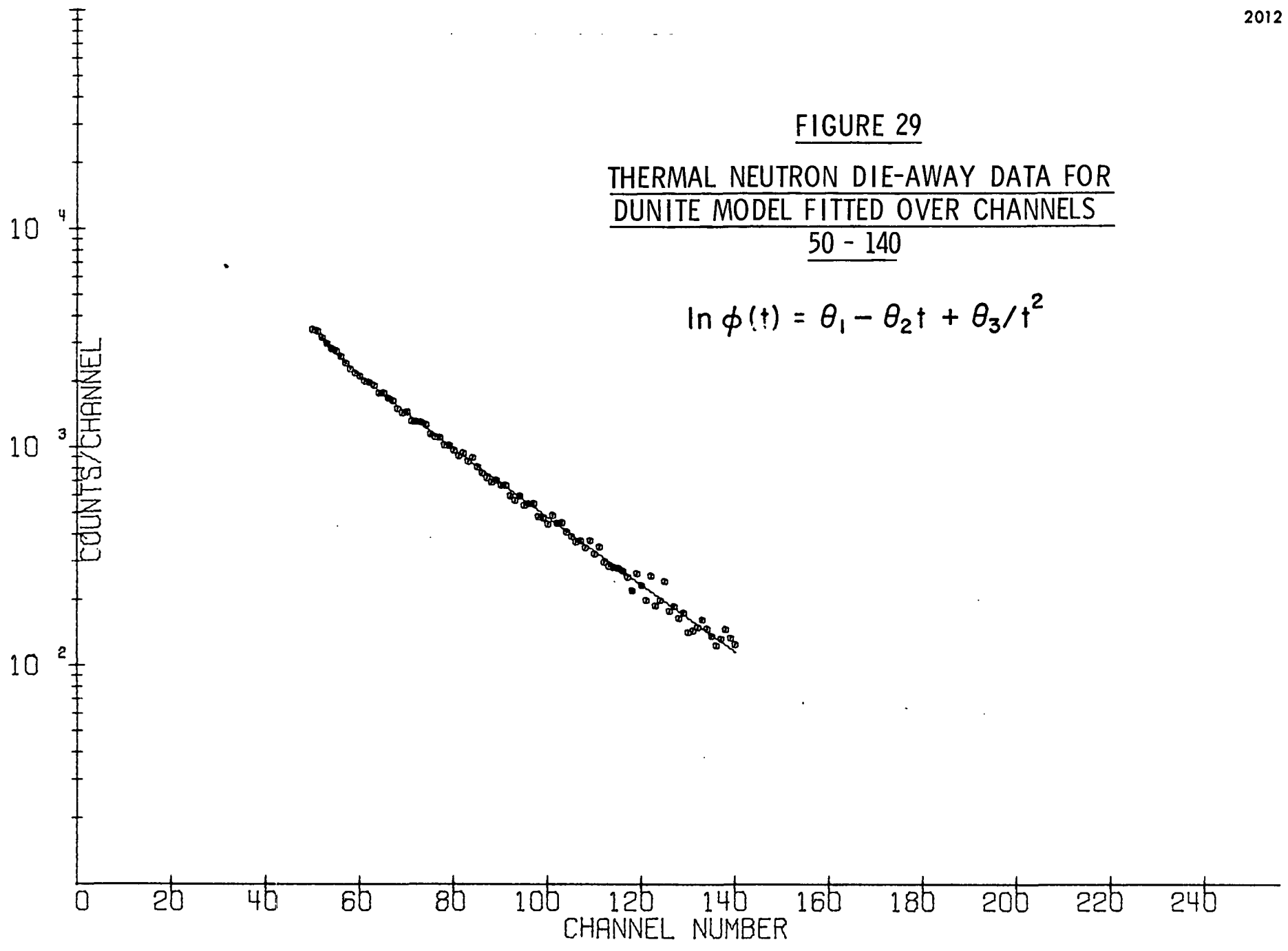


FIGURE 30
THERMAL NEUTRON DIE-AWAY DATA FOR
BURNET RED GRANITE MODEL FITTED OVER
CHANNELS 50 - 120

$$\ln \phi(t) = \theta_1 - \theta_2 t + \theta_3 / t^2$$

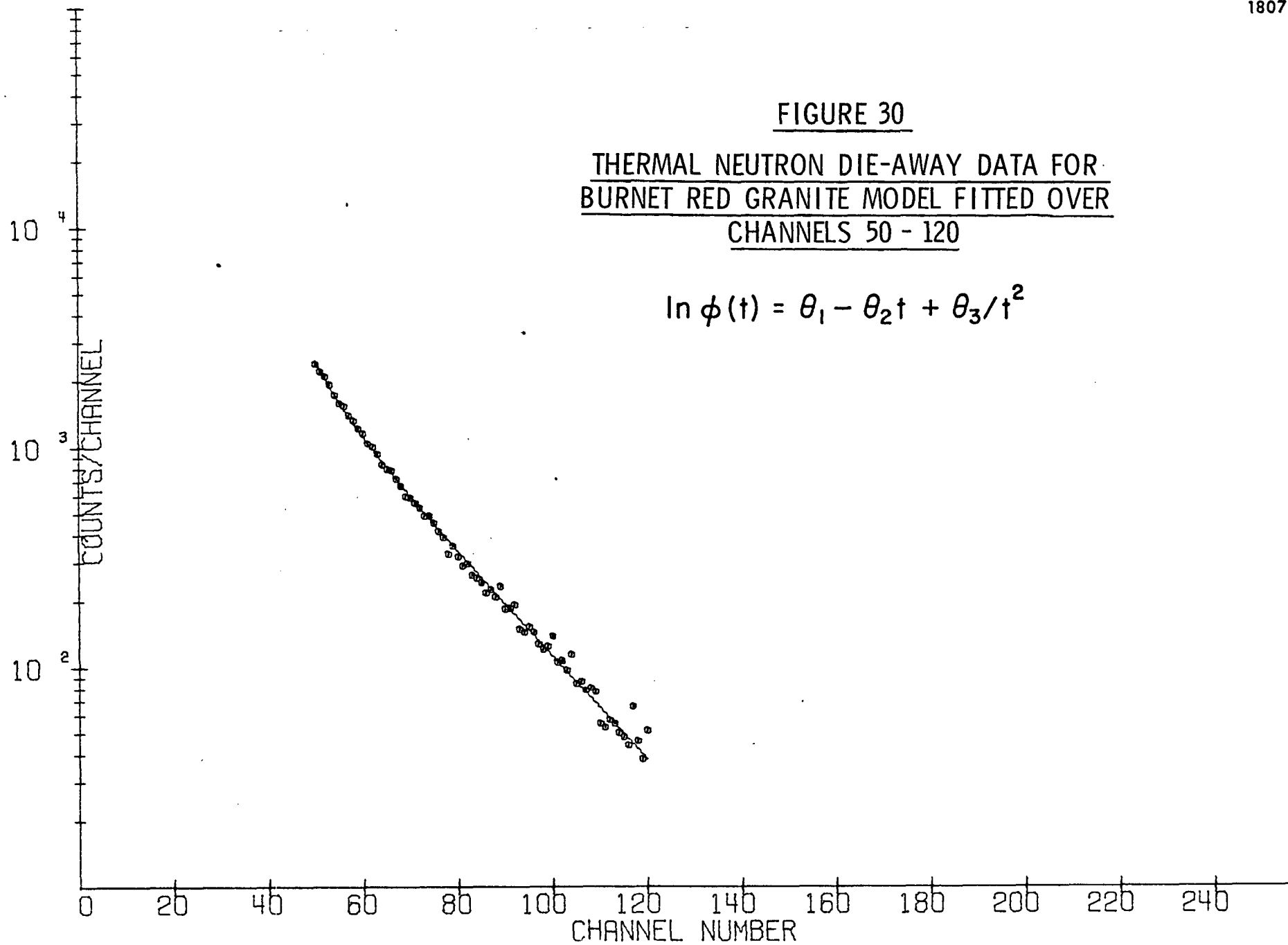


FIGURE 31

THERMAL NEUTRON DIE-AWAY DATA FOR
KNIPPA BASALT MODEL FITTED OVER
CHANNELS 50 - 108

$$\ln \phi(t) = \theta_1 - \theta_2 t + \theta_3 / t^2$$

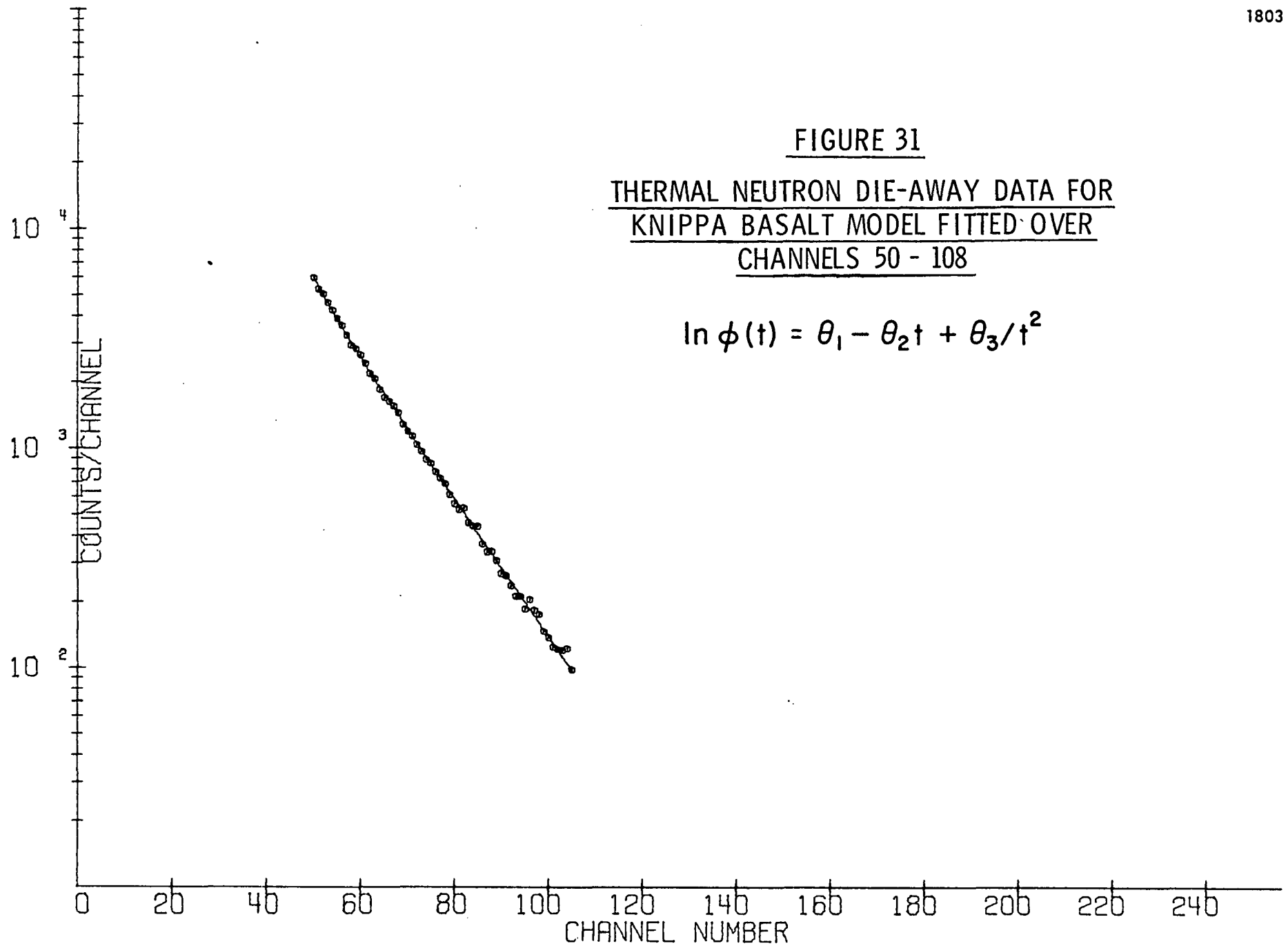


FIGURE 32

THERMAL NEUTRON DIE-AWAY DATA FOR
TEXAS ROCKVILLE GRANITE MODEL FITTED
OVER CHANNELS 50 - 90

$$\ln \phi(t) = \theta_1 - \theta_2 t + \theta_3 / t^2$$

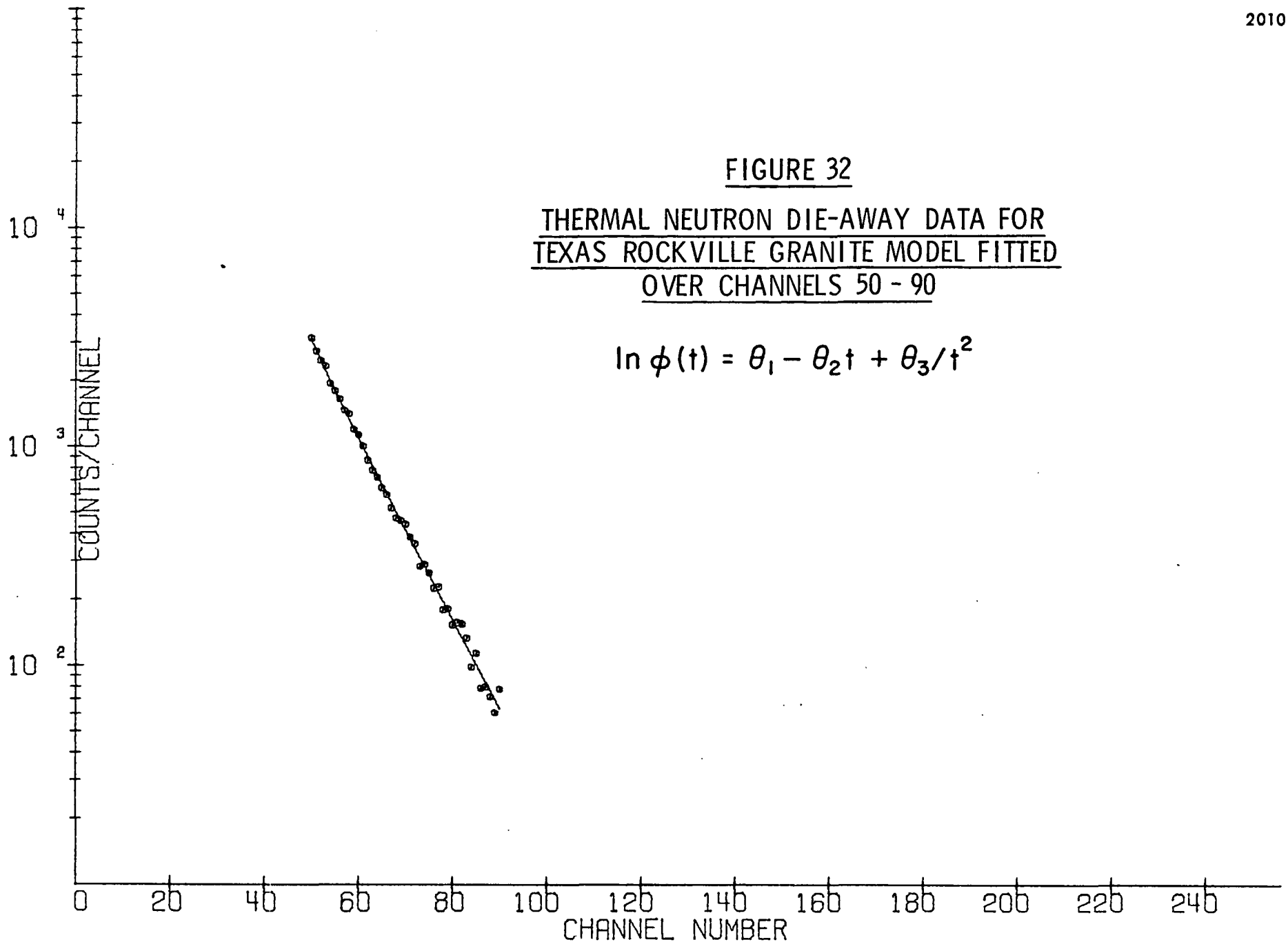
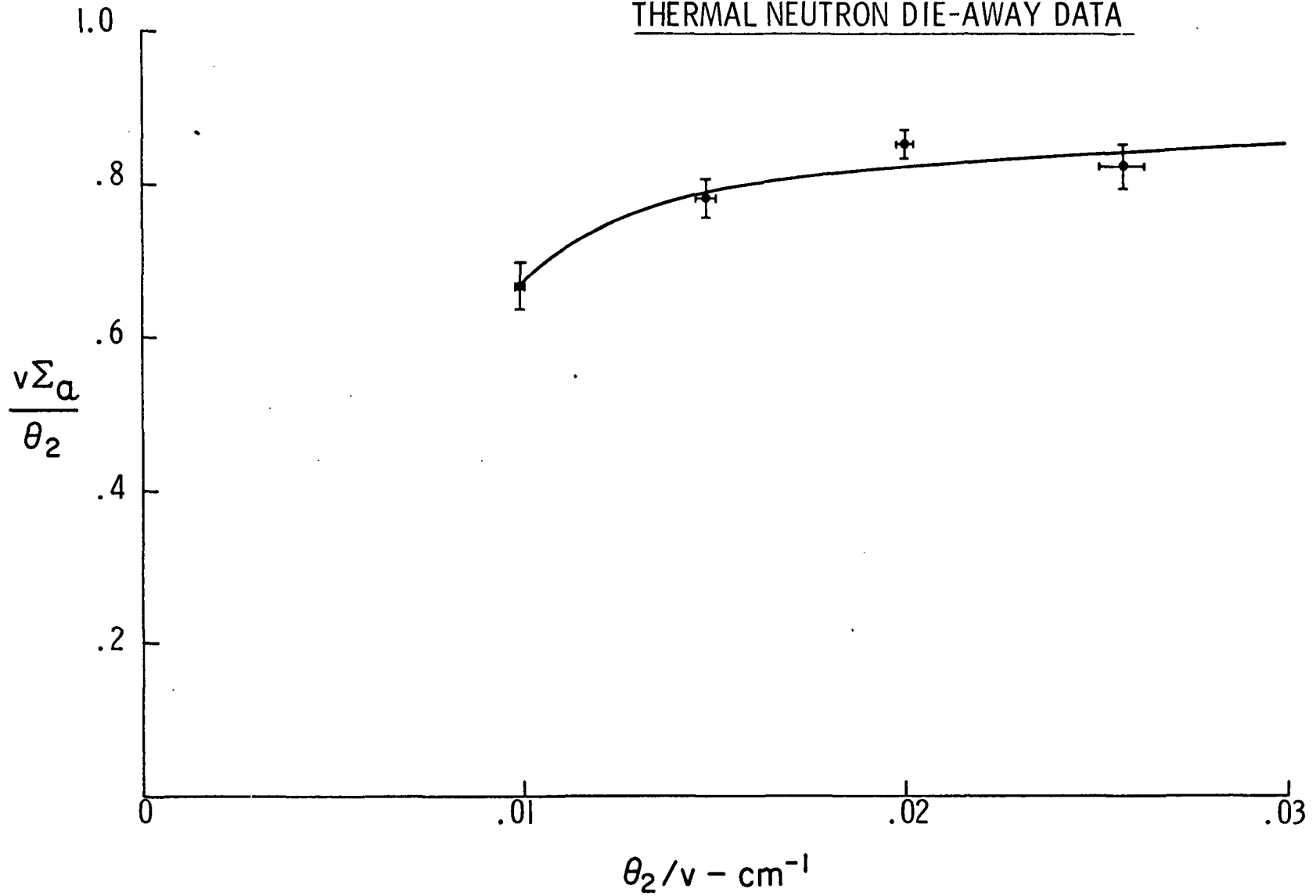


FIGURE 33

CALIBRATION CURVE FOR
THERMAL NEUTRON DIE-AWAY DATA



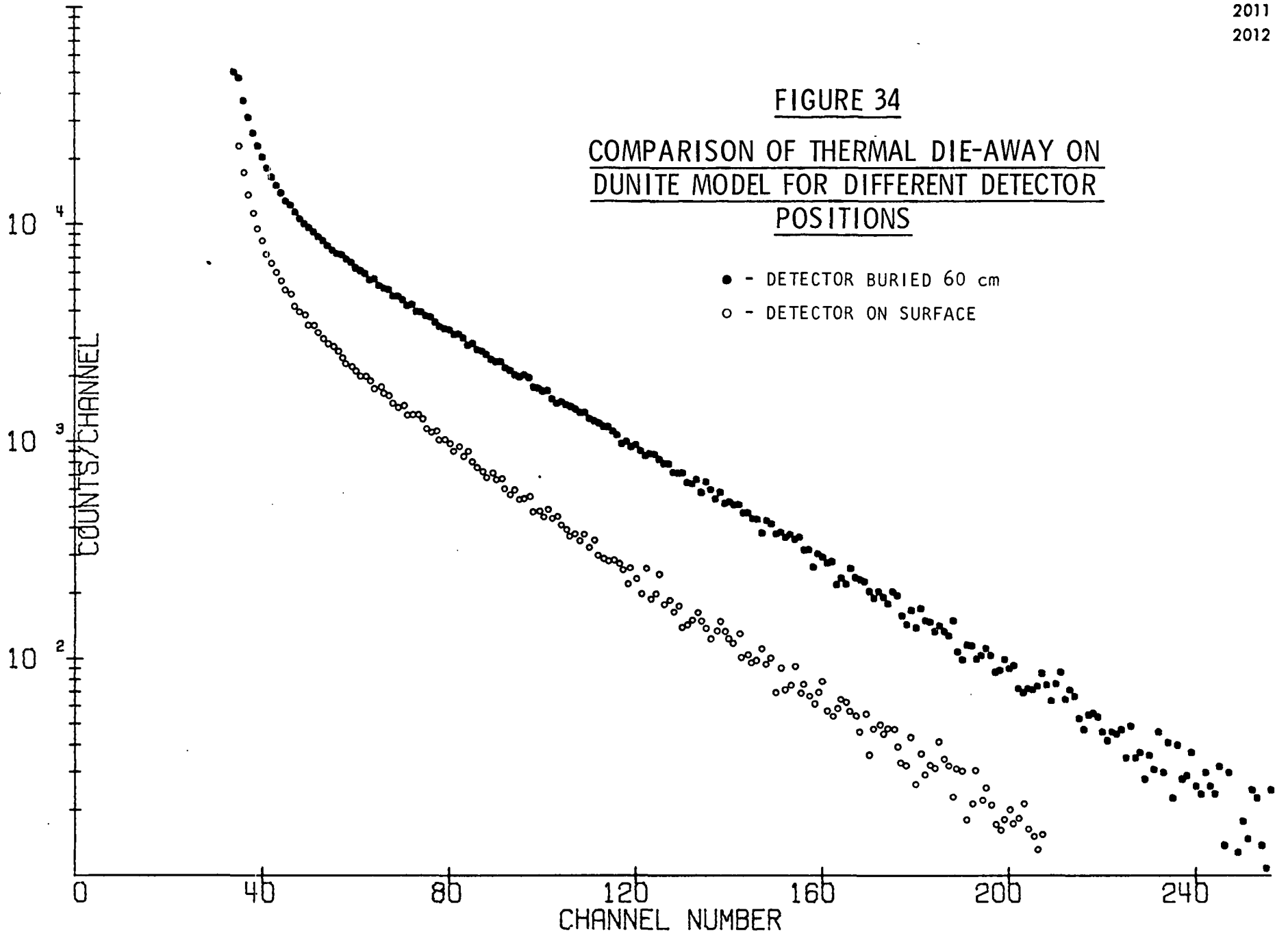


FIGURE 35
GAMMA-RAY DIE-AWAY DATA
FOR ALL FOUR LARGE ROCK MODELS

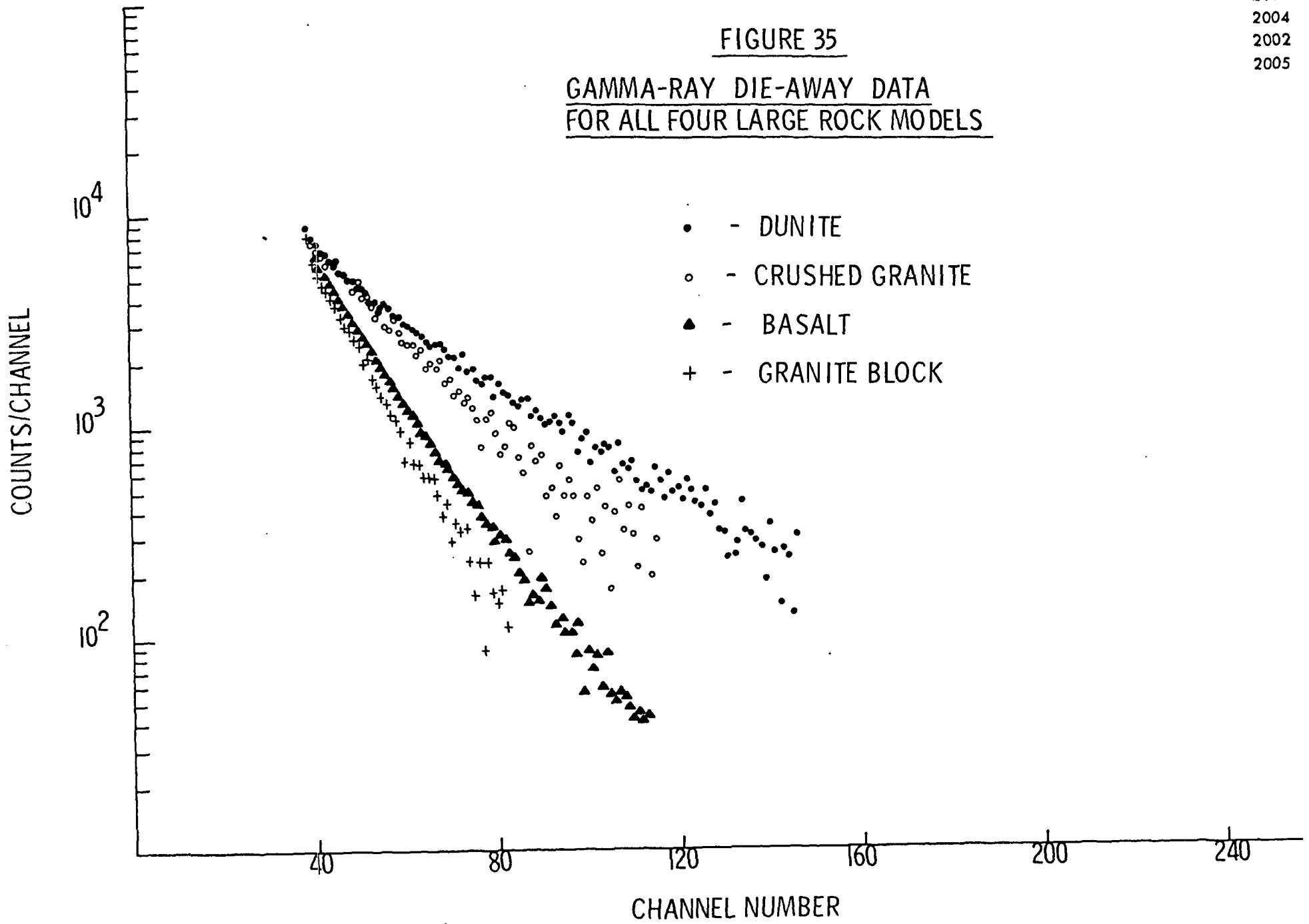


FIGURE 36

GAMMA-RAY DIE-AWAY DATA FOR DUNITE
MODEL FITTED OVER CHANNELS 44 - 90

$$\ln \phi(t) = \theta_1 - \theta_2 t + \theta_3 / t^2$$

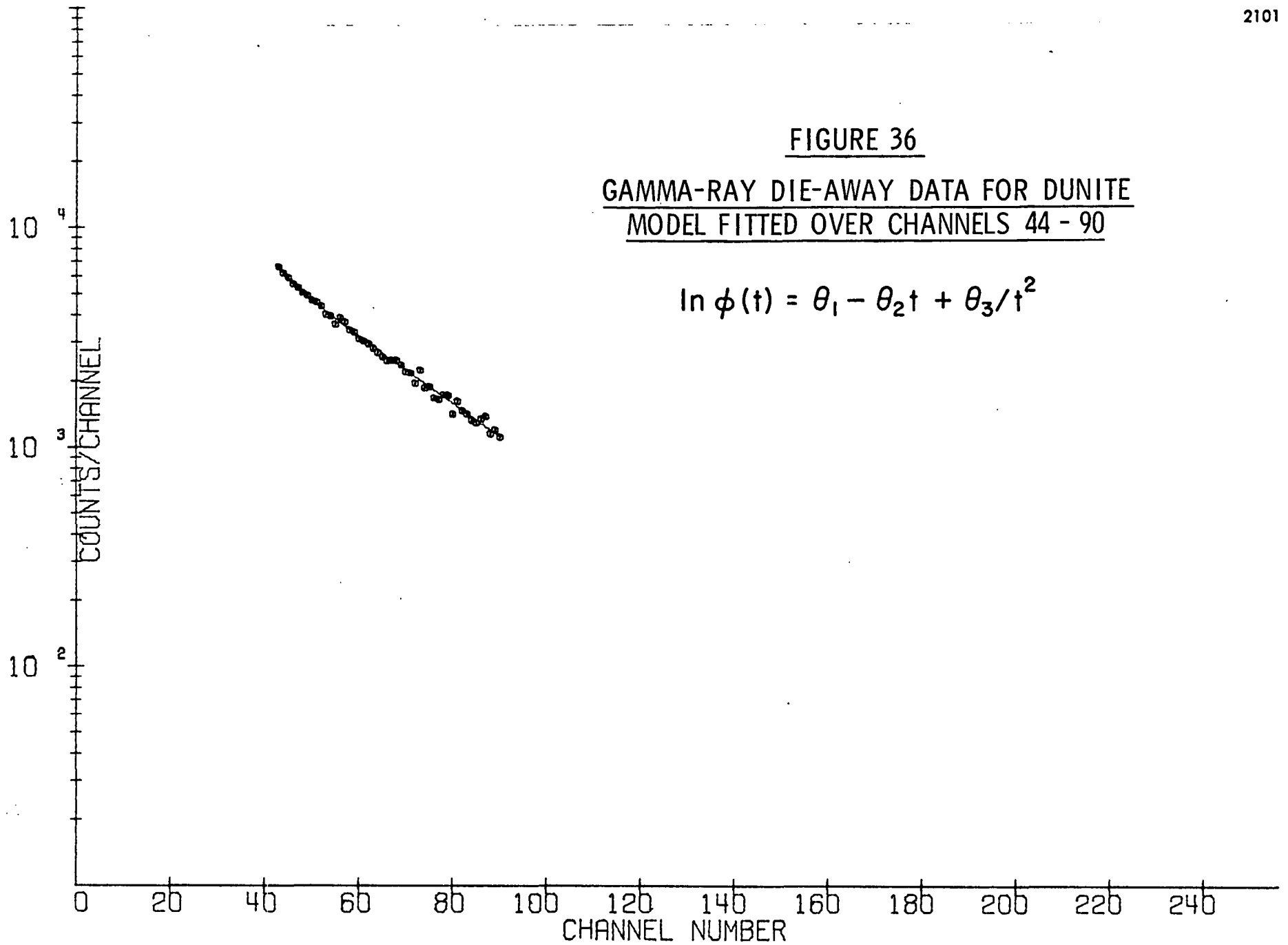


FIGURE 37

GAMMA-RAY DIE-AWAY DATA FOR BURNET
RED GRANITE MODEL FITTED OVER
CHANNELS 44 - 86

$$\ln \phi(t) = \theta_1 - \theta_2 t + \theta_3 / t^2$$

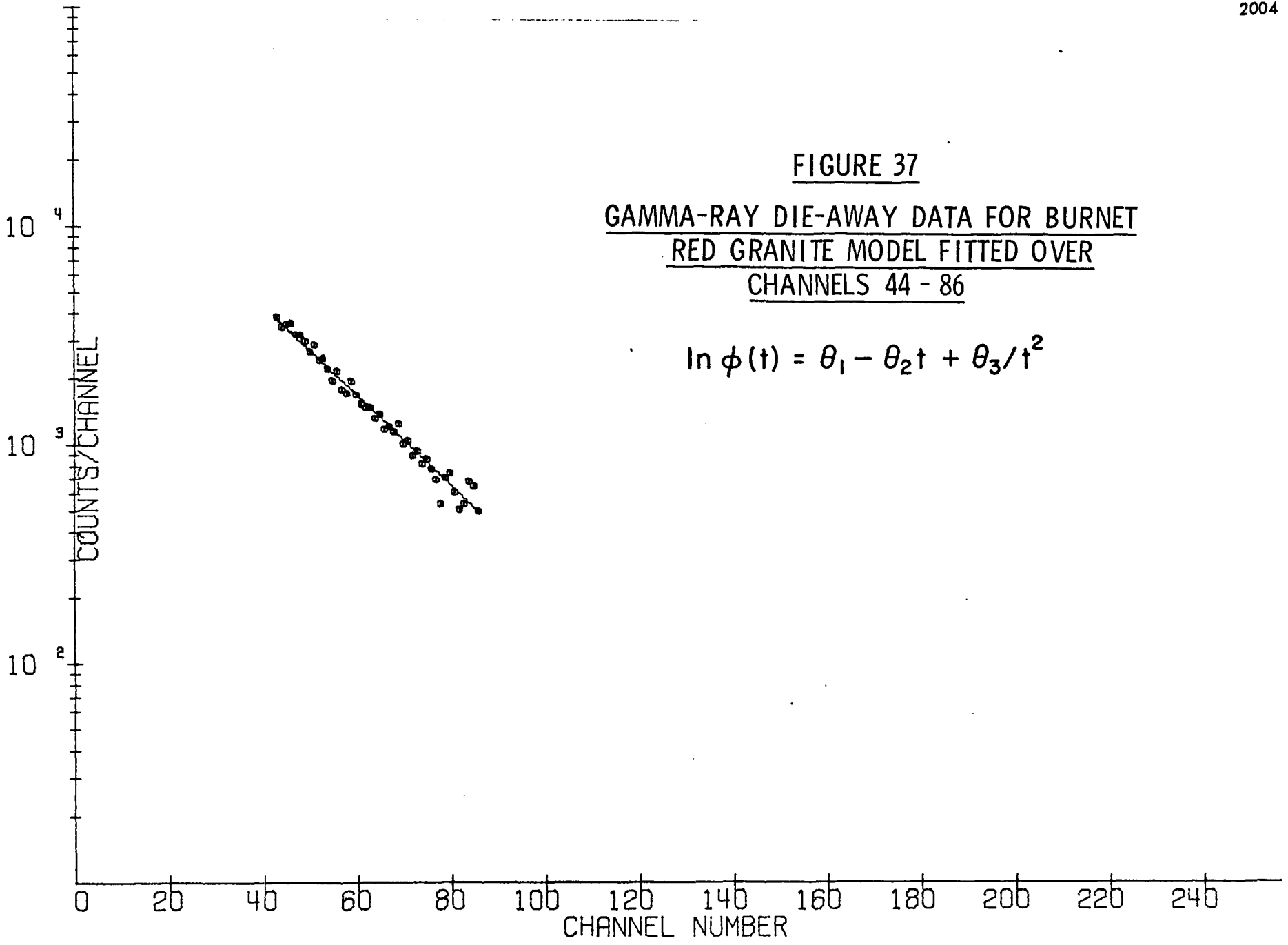
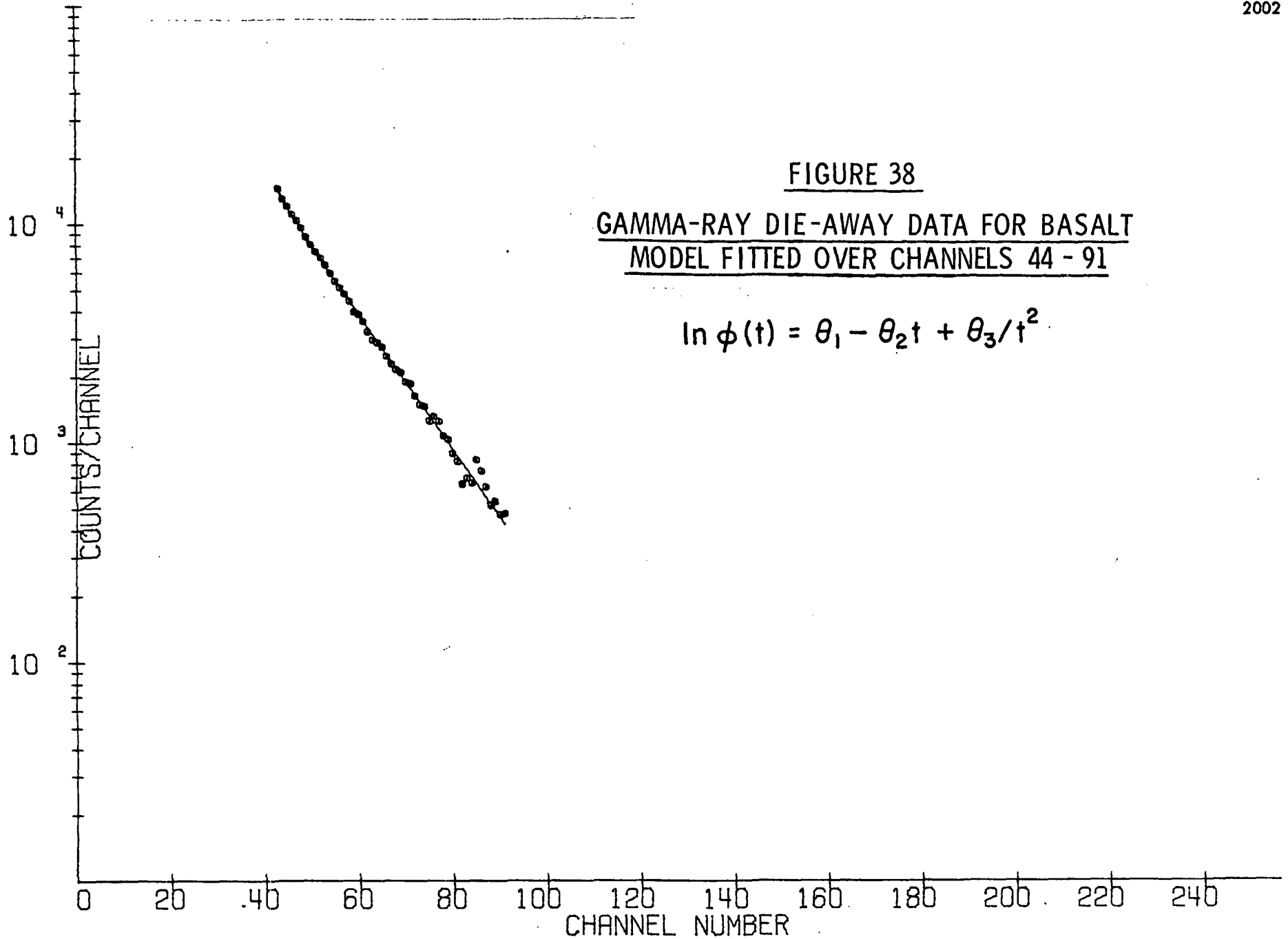


FIGURE 38

GAMMA-RAY DIE-AWAY DATA FOR BASALT
MODEL FITTED OVER CHANNELS 44 - 91

$$\ln \phi(t) = \theta_1 - \theta_2 t + \theta_3 / t^2$$



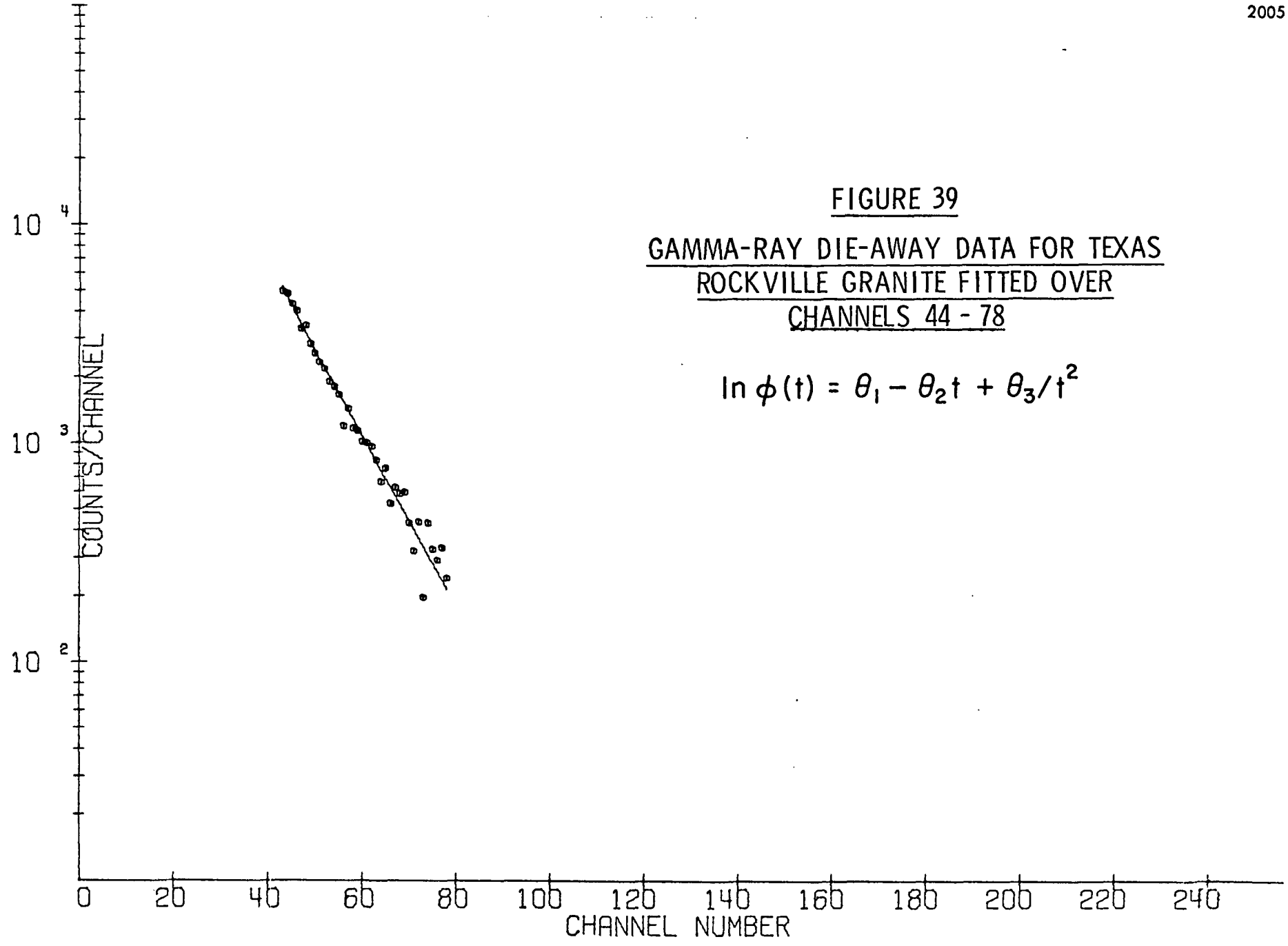


FIGURE 40

CALIBRATION CURVE FOR
CAPTURE GAMMA-RAY DIE-AWAY DATA

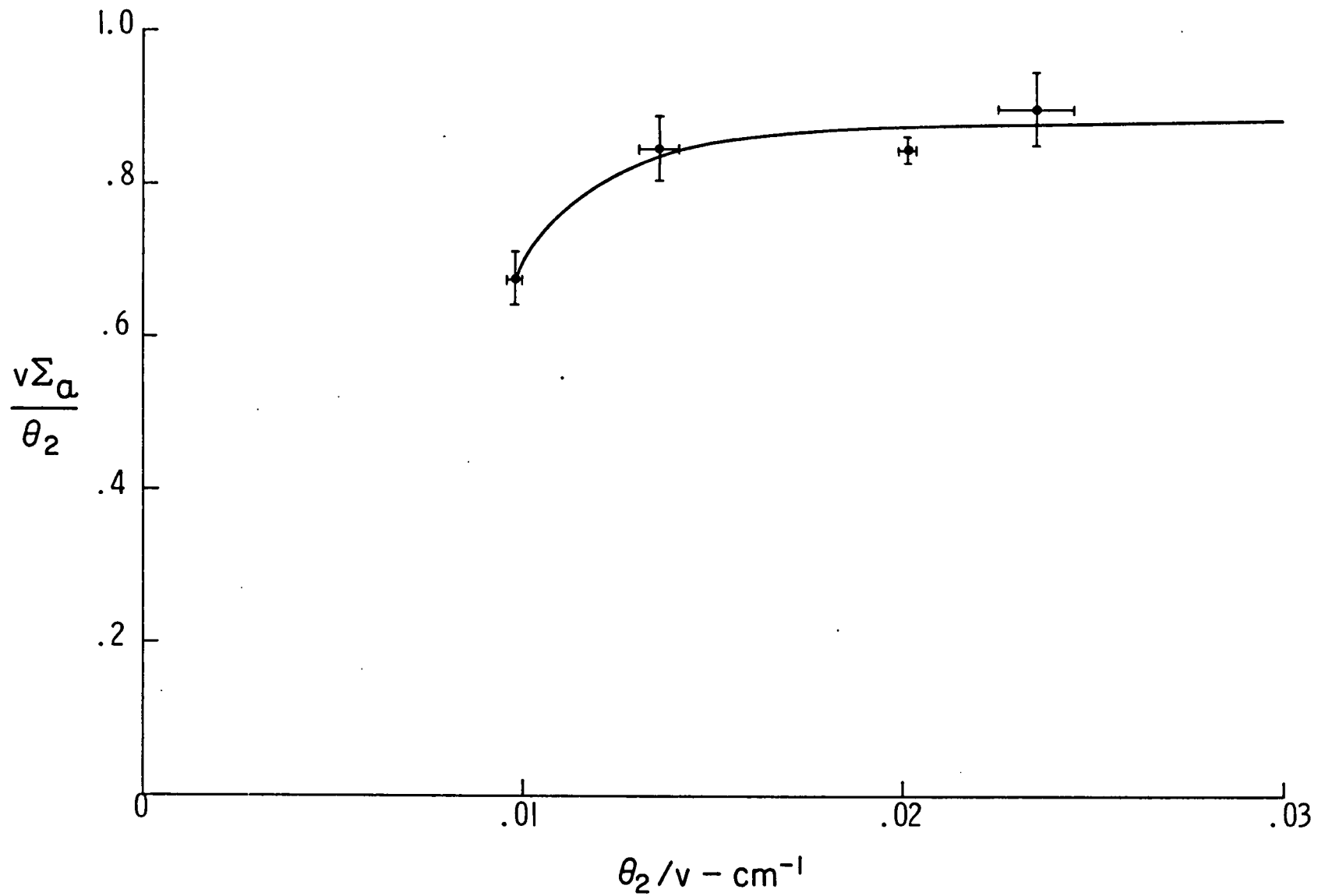


FIGURE 41
PULSE HEIGHT SPECTRA IN $^3\text{He}/\text{Cd}$ DETECTOR

